

METHODS FOR QUANTITATIVE SUSCEPTIBILITY MAPPING AND ITS  
APPLICATION TO CARDIOVASCULAR MRI

A Dissertation

Presented to the Faculty of the Graduate School

of Cornell University

In Partial Fulfillment of the Requirements for the Degree of

Doctor of Philosophy

by

Yan Wen

MAY 2020

© 2020 YAN WEN

ALL RIGHTS RESERVED

METHODS FOR QUANTITATIVE SUSCEPTIBILITY MAPPING AND ITS  
APPLICATION TO CARDIOVASCULAR MRI

YAN WEN, PH. D.

Cornell University 2020

Magnetic Resonance Imaging (MRI) is a powerful noninvasive medical imaging technique capable of volumetric imaging at an arbitrary plane. Another feature of MRI is its ability to produce images with different contrasts mechanism using different image acquisition strategies; contrasts mechanisms such as proton spin relaxation (T1, T2, etc.), proton motion (diffusion, perfusion, flow, etc.), and molecular electron cloud polarization (magnetic susceptibility). This dissertation focuses on the tissue magnetic susceptibility, and the technique for the mapping of magnetic susceptibility called the Quantitative Susceptibility Mapping (QSM). Specifically, this dissertation will describe 1) the strategies for cardiac and respiratory motions compensation in QSM data acquisitions, 2) the post-processing methods for generating high quality cardiovascular magnetic susceptibility maps, 3) the initial experiences of cardiovascular QSM in clinical settings, and 4) a novel QSM reconstruction algorithm to improve the signal model in dipole inversion.

## **BIOGRAPHICAL SKETCH**

Yan Wen was born in Hunan Province, China in 1992. He received the Bachelor of Science degree in Physics from The State University of New York at Stony Brook in 2014. He joined the graduate program in Biomedical Engineering at Cornell University in 2014, received the Master of Science degree in Biomedical Engineering in 2017.

*I Dedicate This Dissertation to My Family*

*For Their Gifts, Love, and Supports.*

## ACKNOWLEDGMENTS

I am grateful for my advisor and mentor, Dr. Yi Wang, for all his guidance and supports in my career development. His perseverance in approaching problems through a rigorous and thorough understanding of the fundamentals have always impressed me and greatly inspired me to approach my problems, both inside and outside of research, with comprehensive and insightful understandings.

I would also like to express my gratitude to Dr. Thanh D. Nguyen and Dr. Pascal Spincemaille, for being the reliable sources of advice and supports during all stages of research. Dr. Nguyen was always patient and generous, and I am especially thankful for his indispensable guidance in pulse sequence development and helps in many off-hours scans. Dr. Spincemaille was always able to provide insightful suggestions to overcome technical roadblocks, especially in the scope of QSM reconstruction.

The clinical aspects of my work could not have been possible without the collaboration with the expert cardiologist Dr. Jonathan W. Weinsaft. He was an essential source of our clinical data and he guided the cardiac QSM project toward a clinically significant direction. I would also like to thank Dr. Martin R. Prince, who is an expert in both medicine and physics, for providing valuable feedbacks in both the development and the presentation of my research.

I also owe a debt of gratitude to my colleagues for the completion of my dissertation. Dr. Tian Liu, an alumnus of our lab, was the first to guide me through the basics of QSM and programming. He was a vital source of knowledge for my early

publications. Dr. Dong Zhou, a former post-doc, provided many discussions on the mathematics and implementations for background field removal in QSM. I would also like to thank Junghun Cho, John Morgan, Ramin Jafari, Kofi Deh, and Zhe Liu for their supportive discussions in both research and life. I am grateful for Kelly McCabe Gillen for providing reliable logistic and editorial supports throughout my time in the lab. I feel fortunate to have worked with other talented members in the lab, Alexey Dimov, Jingwei Zhang, Sarah Eskreis-Winkler, Liangdong Zhou, Jingwei Zhang, Jinwei Zhang, Qihao Zhang, for their insights and encouragements.

Finally, I would like to acknowledge the members on my special committee, Dr. Yi Wang, Dr. David J. Christini, and Dr. Peter Doerschuk, for agreeing to examine this dissertation.

## TABLE OF CONTENTS

BIOGRAPHICAL SKETCH .....	ii
ACKNOWLEDGEMENTS .....	iv
TABLE OF CONTENTS .....	vi
LIST OF TABLES .....	viii
LIST OF FIGURES .....	ix
1. Introduction .....	1
1.1 Background .....	1
1.2 Summary of Contributions .....	6
2. Cardiac Quantitative Susceptibility Mapping (QSM) for Heart Chamber Oxygenation .....	9
2.1 Abstract .....	9
2.2 Introduction .....	11
2.3 Methods .....	12
2.4 Results .....	17
2.5 Discussions .....	19
2.6 Conclusion .....	23
3. Free Breathing Three-Dimensional Cardiac Quantitative Susceptibility Mapping for Differential Cardiac Chamber Blood Oxygenation – Initial Validation in Patients with Cardiovascular Disease Inclusive of Direct Comparison to Invasive Catheterization. ....	30
3.1 Abstract .....	30
3.2 Introduction .....	32
3.3 Methods .....	33
3.4 Results .....	39
3.5 Discussions .....	43
3.6 Conclusion .....	48
4. Quantitative Susceptibility Mapping of Carotid Plaques Using Nonlinear Total Field Inversion: Initial Experience In Patients With Significant Carotid Stenosis .....	57
4.1 Abstract .....	57
4.2 Introduction .....	58
4.3 Methods .....	60
4.4 Results .....	65
4.5 Discussions .....	68
4.6 Conclusion .....	71

5. Multi-Echo Complex Total Field Inversion (mcTFI) Method for Improved Signal Model in Quantitative Susceptibility Mapping .....	78
5.1 Abstract .....	78
5.2 Introduction .....	79
5.3 Theory .....	80
5.4 Methods .....	84
5.5 Results .....	89
5.6 Discussions .....	91
5.7 Conclusion .....	94
5.8 Appendix 5A .....	95
5.9 Appendix 5B .....	98
5.10 Appendix 5C .....	102
6. Conclusion and Future Directions .....	108
6.1 Cardiac QSM .....	108
6.2 Carotid QSM .....	108
6.2 Multi-Echo Complex Total Field Inversion (mcTFI) Method .....	109

## LIST OF TABLES

Table 3.1 .....	55
Table 3.2 .....	56

## LIST OF FIGURES

Figure 1.1 .....	8
Figure 2.1 .....	25
Figure 2.2 .....	26
Figure 2.3 .....	27
Figure 2.4 .....	28
Figure 2.5 .....	29
Figure 3.1 .....	49
Figure 3.2 .....	50
Figure 3.3 .....	51
Figure 3.4 .....	53
Figure 3.5 .....	54
Figure 4.1 .....	72
Figure 4.2 .....	73
Figure 4.3 .....	74
Figure 4.4 .....	75
Figure 4.5 .....	76
Figure 4.6 .....	77
Figure 5.1 .....	104
Figure 5.2 .....	105
Figure 5.3 .....	106
Figure 5.4 .....	107

# CHAPTER 1

## INTRODUCTION

### 1.1 Background

Magnetic Resonance Imaging (MRI) is a powerful noninvasive medical imaging technique capable of multi-contrast volumetric imaging at an arbitrary plane. The main source of MR signals in a typical MRI is hydrogen nuclei, which is a common element found inside a human body. When a hydrogen nuclei is placed inside an external magnetic field, such as the main magnetic field ( $\mathbf{B}_0$ ) of the MRI scanner, it will align with  $B_0$  (z-direction) and precess around  $B_0$  in Larmor frequency, creating a net magnet moment (typically referred to as spin in MR literature). A radiofrequency (RF) pulse with frequency matching the Larmor frequency can be used to flip the spin away from the z-direction by a specific flip angle, this process is called excitation. Following the excitation, MR signals are generated as the spin relaxes to its pre-excitation state, the detection of such signal is called readout. Different excitation and readout strategies can produce MRI images with different contrasts mechanism; contrast mechanisms such as proton spin relaxation (T1, T2, etc.), proton motion (diffusion, perfusion, flow, etc.), and molecular electron cloud polarization (magnetic susceptibility). This dissertation focuses on the measurement of tissue magnetic susceptibility and its application in cardiovascular MRI.

Magnetic susceptibility,  $\chi$ , is a dimensionless proportionally constant that indicates how much magnetization,  $\mathbf{M}$ , was gain when a material was placed inside an external magnetic field,  $\mathbf{B}_0$  in the case of MRI:  $\chi = \frac{M}{B_0}$ . Magnetic susceptibility is an intrinsic property of materials; for MRI in human  $\chi$  is typically referenced to the magnetic susceptibility of water, and then categorize as paramagnetic ( $\chi > 0$ ) or diamagnetic ( $\chi < 0$ ). Commonly found in a human body is calcium, which is highly diamagnetic, and iron, which is highly paramagnetic.

The multi-echo gradient echo (GRE) sequence is typically used for data acquisition in magnetic susceptibility mapping. Note that GRE sequence does not directly measure the magnetic susceptibility, but the magnetic susceptibility directly contributes to the GRE signals. The typical GRE image,  $S_j$ , measured at echo time,  $t_j$ , can be described with the following equation:

$$S_j = m_0 e^{-t_j R_2^*} e^{i\phi_0} e^{it_j 2\pi f} \quad [1.1]$$

where  $m_0$  is the initial magnetization,  $R_2^*$  is the T2 relaxation rate,  $\phi_0$  is the initial phase offset, and  $f$  is the susceptibility field. Derived from the Maxwell's equations (1-3) and using the Lorentz sphere correction (4), the susceptibility field can be approximated as a dipole field and can be modeled as the convolution of a susceptibility distribution,  $\chi$ , with the magnetic field of a unit dipole,  $d$ :

$$\frac{f}{B_0} = d * \chi \quad [1.2]$$

where  $*$  indicates the convolution operation, and  $d$  is the magnetic field generated by a unit dipole:

$$d(\mathbf{r}) = \frac{1}{4\pi} \frac{3 \cos^2 \theta - 1}{|\mathbf{r}' - \mathbf{r}|^3} \quad [1.3]$$

where  $\mathbf{r}$  is the location of observation,  $\mathbf{r}'$  is the location of source, and  $\theta$  is the angle between of  $\mathbf{r}' - \mathbf{r}$  and  $B_0$ . The Fourier Transform of the unit dipole, called the dipole kernel:

$$D(\mathbf{k}) = \frac{1}{3} - \frac{k_z^2}{k^2} \quad [1.4]$$

The technique for reconstruction of the susceptibility map from the MRI images (typically GRE images) is called the Quantitative Susceptibility Mapping (QSM).

The current state of the arts QSM reconstruction methods (5-7) typically first require multiple pre-processing steps to approximate the susceptibility field,  $f$ , from Eq. 1.1 or from variants of Eq. 1.1. Once the magnetic field was obtained, the susceptibility map could then be reconstructed by solving Eq. 1.4 (dipole inversion). The pre-processing typically starts with the estimation of  $f$ ; one common approach is to solve an approximation of Eq. 1.1 as the following:

$$(\phi'_0, f') = \underset{m_0, R_2^2, \phi_0, y}{\operatorname{argmin}} \sum_{j=1}^{N_{\text{echo}}} \left\| |S_j| e^{i\phi_0} e^{it_j 2\pi f} - S_j \right\|_2^2 \quad [1.5]$$

Where  $|S_j|$  denotes the magnitude of the GRE image,  $S_j$ . This estimated  $f$  is often not readily suitable for the dipole inversion step; one issue is that because  $f$  is defined

within a range of  $2\pi$ , any values of  $f$  that exceeds this range will be aliased. Many spatial phase unwrapping algorithms have been developed to undo such aliasing (8,9). The susceptibility field map generated up to this point is typically called the total field, which can be modeled as the composition of local field – field generated by susceptibility sources inside of the region of interest (ROI), and background field – field generated by susceptibility sources outside of the ROI. The ROI susceptibility map could then be reconstructed either by first removing the background field and then perform local field dipole inversion, or directly inverting the total field. The dipole inversion step can be formulated as a maximum likelihood estimation by minimizing the quadratic data fidelity term according to Eq. 1.2:

$$\chi' = \underset{\chi}{\operatorname{argmin}} \|D\chi - f\|_2^2 \quad [1.6]$$

where  $D$  represents the convolution with the unit dipole field and  $f$  is the susceptibility field. Note that the formulation of Eq. 1.6 assumes a Gaussian noise in  $f$ , which is likely untrue as the noise property of  $f$  changed as the estimation of Eq. 1.5, therefore, contributing to model errors in Eq. 1.6. Chapter 5 introduces a method to improve the noise model by fitting the susceptibility distribution directly to the complex GRE images. Another challenge for the inverse problem in Eq. 1.6 it is ill-posed and ill-conditioned, because according to Eq. 1.4, the dipole kernel is zero at  $k_z^2 = k^2/3$ , which corresponds to a pair of opposing cone surfaces at the magic angle  $\cong 54.7^\circ$ . This means any solution in the Fourier Transform of  $\chi$  located at the cone surfaces can satisfy Eq. 1.6. Furthermore, the dipole kernel is very small near the cone

surfaces, which can also lead to the amplification of noise. Therefore, failure to handle this ill-posedness when solving Eq.6 will lead to undesirable results (Figure 1.1).

Many algorithms have been developed to handle the ill-posedness of this inverse problem through the truncation of the singular values in the dipole kernel prior to the k-space division, or by incorporating regularizations to improve the condition of the problem (10). A popular and effective algorithm is the preconditioned total field inversion method, or TFI for short (11):

$$\mathbf{y}' = \underset{\mathbf{y}}{\mathit{argmin}} \|\mathbf{w}(\mathbf{D}\mathbf{P}\mathbf{y} - \mathbf{f})\|_2^2 + \lambda \|\mathbf{M}_G \nabla \mathbf{P}\mathbf{y}\|_1 \quad [1.7]$$

The first term is the data fidelity term, where  $w$  is a diagonal noise weighting matrix,  $P$  is a preconditioner to improve the convergence speed of the problem so that the susceptibility map is  $\chi = Py$ . The second term is a weighted total variation designed to suppress streaking artifacts caused by the singularities of the dipole kernel, where  $\lambda$  is the regularization parameter,  $M_G$  is the binary edge mask reflecting the anatomy, and  $\nabla$  is the gradient operator. The optimization problem in Eq 7 was solved iteratively using the Gauss-Newton (GN) method.

QSM has been extensively optimized in brain MRI, and demonstrated promising results in applications for the quantification of iron concentration (12-14), the characterization of multiple sclerosis lesion (15,16), Parkinson's disease (17-20), and more (21,22). Chapter 2, 3, and 4 provide the techniques and considerations for data acquisition, and the developments and optimizations for post-processing methods to produce high quality QSM maps in cardiovascular MRI.

## 1.2 Summary of Contributions

The works in this dissertation focus on A) the developments and optimizations of data acquisition and image processing methods to generate high quality cardiovascular QSM maps (chapters 2-4), and B) the development of a novel QSM algorithm to improve reconstruction in regions with poor SNR, such as hemorrhage and calcification (chapter 5).

Chapter 2 presents the initial demonstration of the feasibility of *in vivo* QSM in cardiac MRI (23). Since cardiac QSM has not been realized prior to this work, chapter 2 will detail the MRI pulse sequence and data acquisition techniques needed to obtain the cardiac GRE images that are suitable for QSM reconstruction. Then chapter 2 will outline the post-processing methods to reconstruct high quality cardiac QSM maps from the GRE images. Chapter 2 will also provide an initial experience of cardiac QSM as a non-invasive method to measure heart chamber blood oxygenation.

Chapter 3 presents improvements upon the works in chapter 2 by A) developing a more robust MRI pulse sequence that is suitable for clinical deployment, and B) employing additional regularization terms in the dipole inversion step to improve the quality of the reconstructed QSM map (24). Chapter 3 will also provide the initial validation of the accuracy of cardiac QSM based heart chamber blood oxygenation measurements via comparison with invasive catheterization based heart chamber blood oxygenation measurements.

Chapter 4 demonstrates of the feasibility of high quality carotid QSM and its potential application in the characterization of carotid plaques. The optimized data acquisition strategy and parameters for carotid QSM data acquisition will be detailed, and a nonlinear formulation of the TFI algorithm will be presented to improve the quality of the QSM reconstruction.

Chapter 5 presents a novel multi-echo Complex Total Field Inversion (mcTFI) method to compute the susceptibility map directly from the acquired GRE images, therefore avoiding errors from a separate field estimation and retaining the Gaussian noise property in the data. We compared mcTFI with its predecessor, the TFI method, to demonstrate improvements in susceptibility reconstruction, especially in regions with low SNR.

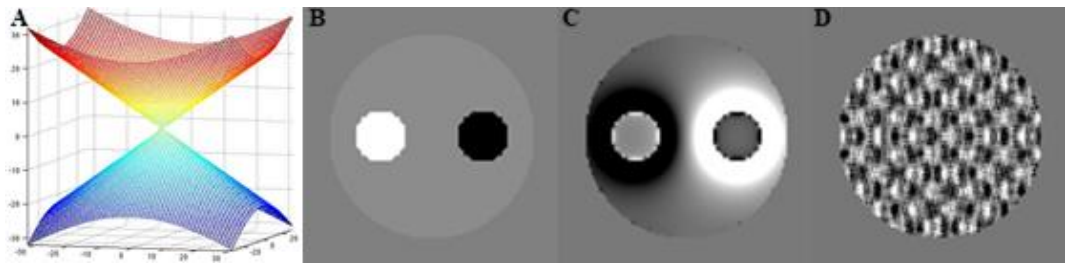


Figure 1.1 A) The double cone surfaces of the dipole kernel. B) A simulated susceptibility distribution. C) The susceptibility field generated by this susceptibility distribution. D) An unreasonable QSM reconstructed using k-space division.

## CHAPTER 2

# CARDIAC QUANTITATIVE SUSCEPTIBILITY MAPPING (QSM) FOR HEART CHAMBER OXYGENATION

### 2.1 Abstract

**Purpose:** To demonstrate the feasibility of *in vivo* quantitative susceptibility mapping (QSM) in cardiac MRI, and to show that mixed-venous oxygen saturation ( $SvO_2$ ) can be measured non-invasively using QSM.

**Methods:** ECG-gated multi-echo 2D gradient echo data were collected at 1.5T from 14 healthy volunteers during successive breath-holds. Phase wraps and fat chemical shift were removed using a graph-cut based phase analysis and IDEAL in an iterative approach. The large susceptibility range from air in the lungs to blood in the heart was addressed by using the preconditioning approach in the dipole field inversion.  $SvO_2$  was calculated based on the difference in blood susceptibility between the right ventricle (RV) and left ventricle (LV). Cardiac QSM quality was assessed by two independent readers.

**Results:** Nine out of fourteen volunteers (64%) yielded interpretable cardiac QSM. QSM maps showed strong differential contrast between RV and LV blood with RV

blood having higher susceptibility values ( $291.5 \pm 32.4$  ppb), which correspond to  $78.3 \pm 2.3\%$  SvO<sub>2</sub>.

**Conclusion:** *In vivo* cardiac QSM is feasible and can be used to measure SvO<sub>2</sub>, but improvements in data acquisition are needed.

## 2.2 Introduction

Mixed-venous oxygen saturation ( $SvO_2$ ) is an important indicator of cardiopulmonary function that is widely used clinically to assess cardiac function in heart failure patients, and to measure shunt fractions in patients with congenital or acquired heart disease (25-27). Currently, conventional measurement of  $SvO_2$  requires an invasive pulmonary artery catheterization procedure (26-28), and is thus both challenging and labor intensive for critically ill patients. Cardiac MRI has emerged as a promising non-invasive method for measuring  $SvO_2$ . It has been demonstrated that  $SvO_2$  can be calculated based on blood T2 relaxation, which requires *in vitro* calibration of blood samples infused with oxygen at different concentrations (29-36). This approach is highly dependent on pulse sequence parameters, field strengths, patient blood characteristics (31,36,37), and accurate blood calibration curves (38-40), thus complicating its clinical applicability (29,35). In contrast, magnetic susceptibility is a fundamental property of biomagnetic sources, with blood susceptibility being linearly dependent on the oxyheme concentration in blood. Therefore, a magnetic susceptibility based oxygenation measurement method would not require calibration (39,41) or blood withdrawal from patients.

Because of the difference in electron pairing in heme iron caused by oxygen binding, oxyheme is diamagnetic and deoxyheme is paramagnetic (6,42). Thus, blood oxygen saturation ( $SO_2$ ) can be measured using Quantitative Susceptibility Mapping (QSM), which is an advanced phase-based MRI method for measuring the distribution of biomagnetic sources (5-7,22,43-46). Furthermore, QSM-based oxygenation

quantification has been demonstrated to be feasible in the brain (41,42,47,48) and QSM has been used to study the mouse heart *ex vivo* (49), but it has not yet been applied to *in vivo* cardiac MRI due to several technical challenges: cardiac and respiratory motion, chemical shift effects from epicardial fat, and a large range in susceptibilities from air in the lungs and surrounding tissue. As known from coronary MRI, electrocardiogram triggering can be used to acquire data in mid-diastole to minimize cardiac motion, and breath-hold or navigator to minimize respiratory motion (50,51). Recent advancements in QSM precisely account for chemical shift effects using graph cuts (9), and deal with large range in susceptibility using preconditioning (52). By combining the knowledge from these advancements, this study aimed to investigate the feasibility of cardiac QSM for chamber blood SvO<sub>2</sub> quantification.

### 2.3 Methods

#### Blood oxygenation quantification using QSM

The blood volume susceptibility,  $\chi$ , depends linearly on the oxygen saturation, SO<sub>2</sub>, and can be estimated as follows (41,42) (ignoring the contribution from blood products other than oxy/deoxyheme):

$$\chi = H[(1 - \text{SO}_2)\chi_{\text{deoxyheme}} + \chi_{\text{oHb}}] \quad [2.1]$$

where  $H$  is the heme concentration in blood (in  $\mu\text{mol/ml}$ ),  $\chi_{\text{deoxyheme}}$  is the molar susceptibility of deoxyheme, and  $\chi_{\text{oHb}}$  is the susceptibility of oxyhemoglobin.  $H$  is a subject-specific physiological parameter which can be measured or estimated. The

multiplicative factor of 4 indicates the number of deoxyhemes contained in a fully desaturated deoxyhemoglobin. Let  $\Delta\chi$  be the blood susceptibility difference between the RV and LV measured on QSM, then the difference in blood oxygenation  $\Delta\text{SO}_2$  can be calculated as:

$$\Delta\text{SO}_2 = \frac{-\Delta\chi}{4H\chi_{\text{deoxyheme}}} \quad [2.2]$$

The value of  $H$  is calculated as (42):  $H = 4Hct \frac{\rho_{\text{RBC,Hb}}}{M_{\text{Hb}}}$ , where  $\rho_{\text{RBC,Hb}} = 0.34 \frac{\text{g}}{\text{ml}}$  is the mass concentration of hemoglobin in a RBC (53),  $M_{\text{Hb}} = 64450 \times 10^{-6} \frac{\text{g}}{\mu\text{mol}}$  is the molar mass of deoxyhemoglobin (54), and the multiplicative factor of 4 refers to the 4 deoxyheme in a deoxyhemoglobin molecule. In this imaging study of healthy volunteers, we assumed  $Hct$  to be .45 for adult males and .4 for adult females (55), so  $H_{\text{male}} = 9.49 \frac{\mu\text{mol}}{\text{ml}}$  and  $H_{\text{female}} = 8.43 \frac{\mu\text{mol}}{\text{ml}}$ . The value of  $4\chi_{\text{deoxyheme}}$  is  $151.054 \text{ ppb} \frac{\text{ml}}{\mu\text{mol}}$  (42). Given the arterial blood oxygen saturation  $\text{SaO}_2$  (measured by pulse oximeter),  $\text{SvO}_2$  can be estimated as  $\text{SaO}_2 - \Delta\text{SO}_2$ .

### Cardiac QSM experiments

This human study was approved by the Weill Cornell Medicine IRB committee and written informed consent was obtained from all subjects prior to imaging. Fourteen volunteers (13 male, 1 female, mean age 31.3 years  $\pm$  5.9, age range = 24-45 years, no history of cardiopulmonary disease) underwent a cardiac MRI exam on a 1.5T clinical scanner (GE HD23.0, GE Healthcare, Waukesha, WI, USA; maximum gradient

amplitude 33 mT/m, maximum slew rate 120 T/m/s). Subjects were imaged supine using a product 8-channel cardiac phased array coil (four anterior, four posterior elements) for signal reception and vector electrocardiographic (ECG) gating for cardiac synchronization. Prior to cardiac QSM, a breath-hold (BH) cine 2D balanced steady-state free precession (SSFP) scan was performed in the two-chamber view to determine the subject-specific optimal cardiac trigger delay time between the ECG trigger and the mid-diastolic diastasis. For cardiac QSM, a BH ECG-triggered 2D multi-echo fast gradient echo (FGRE) scan was performed in the short-axis view using the following typical imaging parameters: TR = 23 ms, TE = 3.6 ms,  $\Delta$ TE = 2.2 ms, number of echoes = 8, in-plane resolution  $\approx 1.25 \times 1.25 \text{ mm}^2$ , slice thickness = 5 mm, number of slices = 20, interleaved linear view ordering, first-order flow compensation in the readout and slice directions (for the readout direction, flow compensation gradients were applied to the first echo, and subsequent echoes were naturally flow compensated; for the slice direction, flow compensation gradients were applied to the slice-selection gradient), ASSET parallel imaging factor = 1.5, 10 views per heartbeat (HB) acquired during mid-diastolic diastasis, one slice per breath-hold of approximately 15 sec each. To maximize the consistency of respiratory position between imaging slices acquired in separate breath-holds, all subjects were instructed to completely exhale before holding their breath.

#### *QSM reconstruction and blood oxygenation difference calculation*

Figure 2.1 summarizes the main steps of cardiac QSM computation from the complex multi-echo GRE image data. First, an initial total field map was obtained by voxel

based linear regression on the phase of the complex data obtained at multiple TEs. This field map estimate contains field wraps and includes contributions from fat chemical shift, both of which need to be removed for accurate QSM reconstruction (56). In this study, an advanced graph-cuts based unwrapping method called SPURS (9) was used in conjunction with the IDEAL water/fat separation algorithm (57,58) in an iterative manner (56) to accurately remove fat chemical shift. The susceptibility map was then computed from the total field using the recently developed Total Field Inversion (TFI) algorithm (59). Briefly, this algorithm solves the total field-to-susceptibility source inversion problem by minimizing the following cost function:

$$\chi^* = \mathbf{arg\,min}_{\chi} \frac{1}{2} \|w(f - d * P\chi)\|_2^2 + \lambda \|M_G \nabla P\chi\|_1 \quad [2.3]$$

where  $\chi$  is the unknown susceptibility map in the whole field of view (FOV),  $f$  is the measured total field,  $d$  is a dipole kernel,  $*$  is a convolution operator,  $\nabla$  is a gradient operator,  $\lambda$  is a regularization parameter,  $M_G$  is an edge mask computed from the magnitude image, and  $w$  is a weighting factor depending on SNR ( $w \sim \text{SNR}$ ).  $P$  is a right preconditioner, designed to increase the convergence speed of the algorithm. As in (59),  $P$  was a binary mask that was equal to 1 inside the region of interest (ROI) and a larger value  $P_{outside}$  outside the ROI. In this study, both the optimal values of  $P_{outside} = 20$  for the background air and lung region, and  $\lambda = 1000$  were empirically determined in one subject by visual inspection of corresponding QSM maps and then fixed for the remaining subjects. For comparison with conventional QSM processing often used in brain imaging, a second set of QSM maps were computed using the PDF

algorithm for background field removal (60) and the MEDI algorithm for dipole deconvolution (44). A manually segmented ROI centered on the heart was used as a data mask in MEDI (which typically produced QSM maps with less artifacts compared to those obtained with a full FOV ROI).

For cardiac QSM analysis, the endocardial surfaces of the RV and LV were manually traced on GRE magnitude images. The mean susceptibility difference between RV and LV blood pools was measured, and  $\Delta\text{SO}_2$  was calculated using Eq.2.  $\text{SaO}_2$  was measured using pulse oximeter, and  $\text{SvO}_2$  was estimated as  $\text{SaO}_2 - \Delta\text{SO}_2$ . The visual quality of each cardiac QSM map obtained with the TFI algorithm was scored by two cardiologists experienced in reading cardiac MRI using a three-point scale (1 = major artifacts and uninterpretable, 2 = moderate artifacts and reasonable quality, and 3 = minimum artifacts and excellent quality). To correlate the QSM scores with consistency of breath-holds, we quantified spatial slice consistency as follows: two perpendicular long-axis images clearly depicting the heart-lung interface were obtained by reformatting the acquired short axis slices. A simple signal intensity thresholding on these images was used to find the surface curve corresponding to this heart-lung interface. A second derivative along this curve was computed and the slice inconsistency was defined as the standard deviation of this second derivative curve. A high standard deviation corresponded to a greater slice inconsistency (less smooth heart-lung interface). The Wilcoxon rank-sum test with Bonferroni correction was used to assess the statistical differences in slice inconsistency among the three groups of QSM scores. Cardiac  $\text{R}2^*$  maps were also calculated using ARLO (61), and the

average blood  $R2^*$  values were measured in the RV and LV using the same endocardial segmentations used in QSM analysis.

## 2.4 Results

The average scan time of cardiac QSM was  $11.7 \pm 1.9$  min. The average heart rate was  $64.9 \pm 4.7$  bpm (beats per minute). All subjects were able to maintain good breath-holding during data acquisition for individual slices, leading to excellent GRE images free of motion artifacts (Figs.2.2-2.4). However, the consistency of end-expiratory breath-holding position between consecutive slices was variable among the subjects, this can be seen as slice misregistration on the long-axis reformatted images (Fig.2.4). Of the 14 acquired cardiac QSM maps, 4 (29%) had excellent image quality (score=3), 5 (36%) were reasonable (score=2), and remaining 5 (36%) had significant artifacts and were uninterpretable (score=1). This resulted in a success rate of 64% (9/14, defined by scores  $\geq 2$ ). The average  $SaO_2$  measured using pulse oximeter was 98.7%. The measured RV to LV susceptibility differences for QSM maps obtained with TFI with image quality scores of 1, 2, and 3 were  $188.6 \pm 64.9$  ppb,  $266.1 \pm 22.2$  ppb, and  $323.3 \pm 14.6$  ppb, respectively. The corresponding values for QSM obtained with the conventional PDF+MEDI method were  $98.1 \pm 18.3$  ppb,  $122.6 \pm 43.5$  ppb, and  $156.1 \pm 54.2$  ppb, respectively. The corresponding  $SvO_2$  values were  $85.6 \pm 4.6\%$ ,  $80.1 \pm 1.2\%$ , and  $76.0 \pm 1.1\%$  for TFI versus  $93.2\% \pm 1.28\%$ ,  $91.4\% \pm 3.0\%$ , and  $89.1\% \pm 3.8\%$  for PDF+MEDI. The average RV to LV susceptibility difference for score  $\geq 2$  was  $291.5 \pm 32.4$  ppb (vs.  $136.0 \pm 48.3$  ppb for PDF+MEDI), which corresponds to a  $SvO_2$  of  $78.3\% \pm 2.3\%$  (vs.  $90.5\% \pm 3.4\%$  for PDF+MEDI). The values obtained with

TFI were in line with the normal range of SvO<sub>2</sub> in healthy adults at approximately 60-80%, while PDF+MEDI yielded values well above this range. There was weak contrast between LV myocardium and LV arterial blood on QSM (Figs. 2.2-2.3), with an average LV blood vs. myocardium susceptibility difference of  $43.2 \pm 32.5$  ppb measured on the TFI derived QSM maps with score  $\geq 2$ , and  $30.1 \pm 17.8$  ppb measured on the PDF+MEDI derived QSM maps ( $p=0.44$ , paired t-test). The average slice inconsistency (in pixels) was 2.15, 1.12, and 1.00 for datasets that produced QSM with image scores of 1, 2, and 3, respectively. There was a significant difference in slice inconsistency between QSMs with quality score of 1 and 2 ( $p = 0.016$ ) and between those with score of 1 and 3 ( $p = 0.016$ ). The average RV R2\* value across subjects was  $8.5 \pm 0.8$  Hz, which corresponded to a SvO<sub>2</sub> of  $72.5 \pm 6.6\%$ ,  $82.8 \pm 2.2\%$ , and  $82.2 \pm 7.5\%$  using the blood calibration curves reported in Silvennoinen et al. (38), Spees et al. (39), and Li et al. (40), respectively.

Two representative examples of cases with scores of 3 are shown in Figure 2.2. Strong contrast between the RV and LV blood pool can be seen on QSM, this reflects the differential oxygenation levels in the venous (paramagnetic) and arterial (diamagnetic) blood. In Figure 2.3, a case with a score of 2 shows a similar increase in susceptibility from LV to RV, though there are more apparent streaking and noise artifacts as compared to the cases shown in Figure 2.2. Figure 2.4 shows an example of a failed QSM map with a score of 1, in which major artifacts are present, resulting in poor or physiologically not meaningful RV-to-LV contrast. Figure 2.5 shows the comparison of the R2\* map, the QSM map obtained with PDF+MEDI, and the QSM map obtained

with TFI in one volunteer. In this example, compared to the  $R2^*$  map, both of the QSM maps shows improved visual contrast between RV and LV blood. Both QSM maps are free of streaking artifacts, but TFI yielded a realistic  $SvO_2$  of 77.0%, while the PDF+MEDI value was 90.1%, which was well outside the normal range in healthy subjects.

## 2.5 Discussion

Our preliminary data in healthy volunteers showed that *in vivo* cardiac QSM is feasible, but requires improvements in data acquisition to increase success rate and improve QSM quality. The difference in QSM between LV and RV blood can be used to indicate the changes in oxygenation between systemic and venous blood, however there is little QSM contrast between LV blood and myocardium in healthy subjects.

In this study, the average  $SvO_2$  values derived from the susceptibility maps of healthy volunteers were found to be in reasonable agreement with those reported in the literature. For successful QSM scans (image score  $\geq 2$ ), the average  $SvO_2$  was approximately 78%, which falls in the high end of the normal range (60-80%) (28), thus indicating an underestimation of susceptibility difference between RV and LV blood. This underestimation may be attributed to the fairly large voxel size (particularly in the slice direction) (62), which is needed to keep the scan time reasonably short. Another potential factor is the gradual decrease of arterial blood oxygenation in the LV during the length of the breath-hold (63). Lastly, the hematocrit

value of 0.45 for adult male and 0.4 for adult female, which might need to be adjusted for individual subjects.

Normal myocardium is weakly diamagnetic, and thus appears isointense with oxygenated LV blood on QSM. This image feature may potentially enable cardiac QSM to detect pathological conditions that alter myocardial tissue properties. For example, intramyocardial hemorrhage is a known consequence of acute myocardial infarction that has been associated with adverse LV chamber remodeling and poor clinical outcomes (64,65). Given that hemorrhage would be expected to cause myocardium to become highly paramagnetic,(66) both diagnosis and quantification could potentially be well addressed by QSM. QSM has been used to measure intracerebral hemorrhage (ICH) and differentiate ICH from calcification (67).

Whereas ICH risk has limited cerebral revascularization treatment to just to 1-8% of ischemic stroke patients (68), IMH damage to the heart as a long term causal factor for systolic heart failure after acute myocardial infarction is becoming more recognized (64,65).

While QSM is an established technique for mapping tissue and blood susceptibilities in the brain (6,7,22,43-45,47,67,69), this technology has not been applied to the chest due to several technical challenges. A major challenge common to heart imaging is respiratory and cardiac, which produce blurring and ghosting artifacts. In this first cardiac QSM study, a short breath-hold of 15 seconds was used to suspend respiration during acquisition, and data sampling was timed to the mid-diastolic cardiac rest period to minimize cardiac motion. In our cohort of healthy volunteers with good

breath-holding ability and low heart rate (65 bpm on average), individual GRE image slices with excellent image quality could be obtained. However, significant variability in QSM maps was observed (Figs. 2.2-2.4), and cardiac QSM was deemed successful in only 64% of subjects. This low success rate could be explained by the spatial inconsistency between consecutive slices that were acquired in different breath-holds. This misregistration artifact is best visualized in the long-axis view (Fig. 2.4). Misregistration can lead to major errors such as artificial field discontinuities in the field map estimation, which propagate into the final QSM, ultimately leading to severe artifacts. Our results demonstrated that as the slice inconsistency increased, the resulting QSM quality decreased. Spatial misregistration between imaging slices can be a greater problem in older patients with cardiopulmonary diseases who have limited breath-holding capabilities (70). Slice inconsistency is not a challenge for R2\* based oxygenation measurement methods, that are voxel-based. One approach to overcoming the challenge from respiratory motion in cardiac QSM is to use a free-breathing navigator GRE acquisition (51), which will be a main focus of our future work.

In addition to the motion challenge during cardiac QSM acquisition, the quality of cardiac QSM depends on the ability of the post-processing algorithm to successfully remove the chemical shift effect of epicardial fat and accurately search through the large susceptibility range from near zero susceptibility sources of heart tissue and very high susceptibility sources of air in the lungs. In this study, a novel algorithm based on SPURS (9) and IDEAL (57) was used in an iterative chemical shift update scheme

(56) to improve the quality of the field map in the fat regions (Fig. 2.1). To address the large susceptibility range, current state-of-the-art QSM methods generally perform background field removal first to estimate the local field, from which QSM is obtained through dipole field inversion. However, this two-step approach fundamentally contains errors in estimating background field from inaccurate boundary conditions (6,71), and these errors tend to carry over to the dipole inversion step, resulting in errors in the final QSM. In this work, the large susceptibility range is systematically managed using the preconditioning approach with TFI, which has been shown to be better than the background field removal methods at the interface between weak and strong susceptibility sources (59). As illustrated in Figure 2.5, we found that TFI yielded SvO<sub>2</sub> measurements within the expected range, while PDF+MEDI produced unusually high values well above the range expected from healthy volunteers. This strongly suggests that TFI is a more robust algorithm for cardiac QSM. While a simple binary mask was used for preconditioning in the TFI algorithm implemented in this study, a more complex preconditioner that relies on knowledge of strong susceptibility sources inside an ROI (i.e. RV blood, fat, bone, and possibly hemorrhage) may further improve QSM quality.

This initial feasibility study of cardiac QSM has several limitations. First, the current 2D approach uses relatively thick slices (5 mm) and still requires a long scan time (over 10 min). The need for sustaining a consistent breath-holding over this extended period precluded the recruitment of cardiac patients who often have limited breath-holding capability. Potential approaches for accelerating cardiac QSM include the use

of more efficient echo planar readout (72), parallel imaging (73) and echo sharing (74), as well as recent image reconstruction methods which combine k-space undersampling with compressed sensing (75). Second, the *in vivo* blood oxygenation difference between RV and LV obtained with QSM was not compared with the reference blood sampling method. Third, flow compensation was performed only in the readout and slice directions, which was needed to keep TR and the corresponding breath-hold length short. However, a previous study (47) has showed that 3D flow compensation can significantly improve the accuracy of QSM in regions with flow. Furthermore, the blood flow pattern in heart chambers during the mid-diastolic LV filling is complex, potentially resulting in phase errors that cannot be corrected with first-order flow compensation. As the result, the ventricular blood QSM values may have been affected by residual phase shift due to incomplete flow nulling, which may explain the slight increase in susceptibility of the LV blood in the apex compared to that at the basal slice (Figs. 2.2-2.3). Finally, it has been reported that 2D slice interleaved GRE acquisitions may produce inter-slice phase errors that can be corrected (72,76,77). We have carefully examined our GRE phase data and did not observe such errors, possibly because this study used a single slice 2D acquisition (without slice interleaving). However, phase inconsistency remains a potential concern regarding data acquisition.

## **2.6 Conclusion**

In this work, we demonstrated for the first time, the feasibility of *in vivo* cardiac QSM, and showed that a reasonable SvO<sub>2</sub> value can be measured non-invasively using this method.

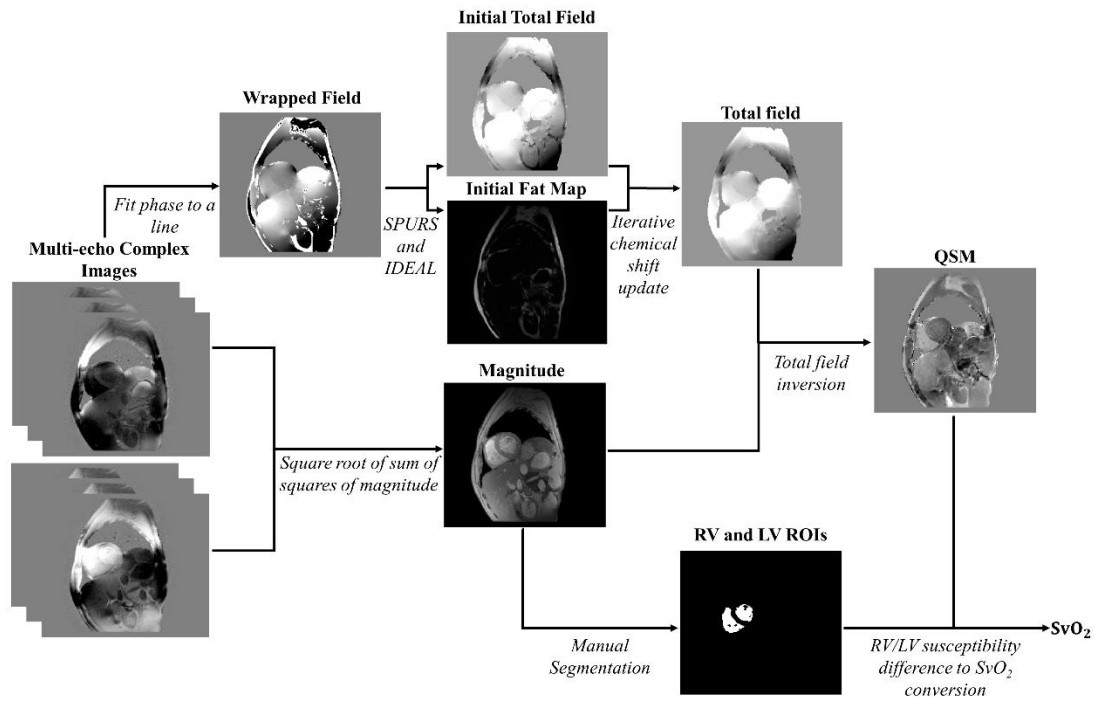


Figure 2.1. Flow chart of cardiac QSM post-processing.

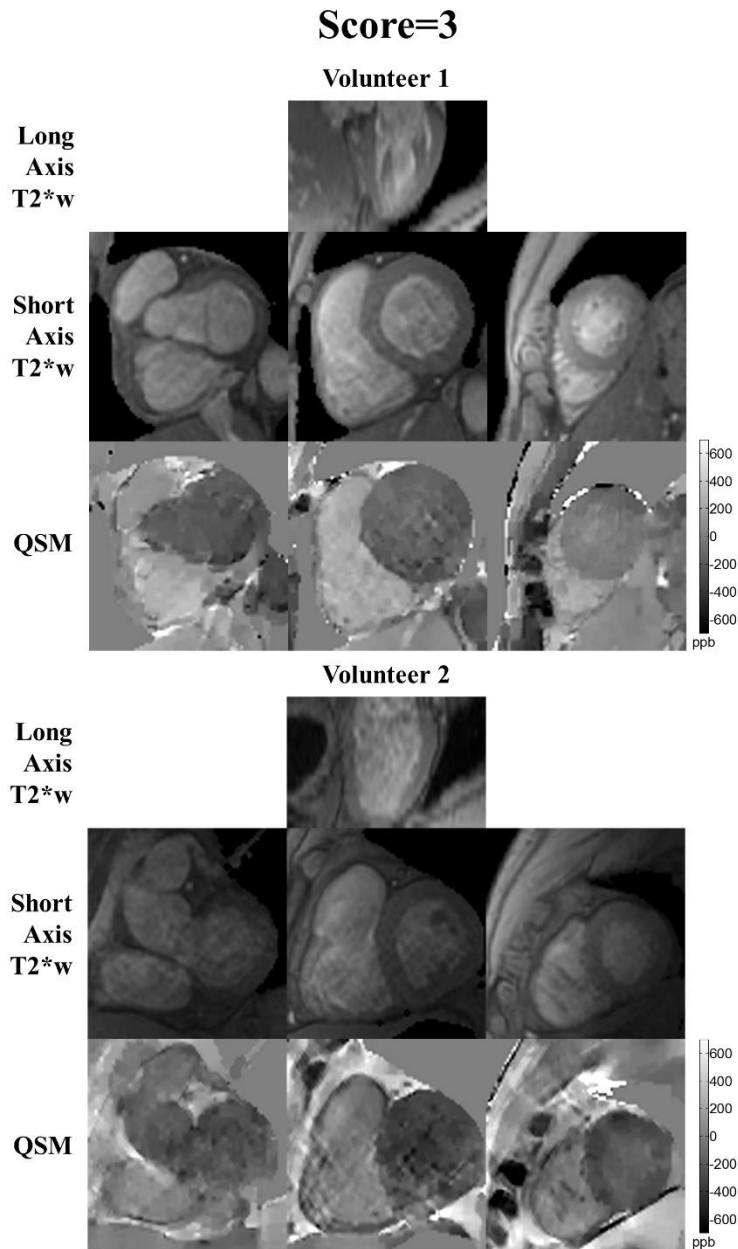


Figure 2.2. Two representative high quality cardiac QSM examples, demonstrating differential susceptibility between the left and right sides of the heart. Magnitude images reformatted into long axis in the top row, short axis magnitude images in the middle row, and corresponding QSM in the bottom row. QSM demonstrated oxygenation differences throughout the basal (left), mid, and apical (right) chambers, in both examples.

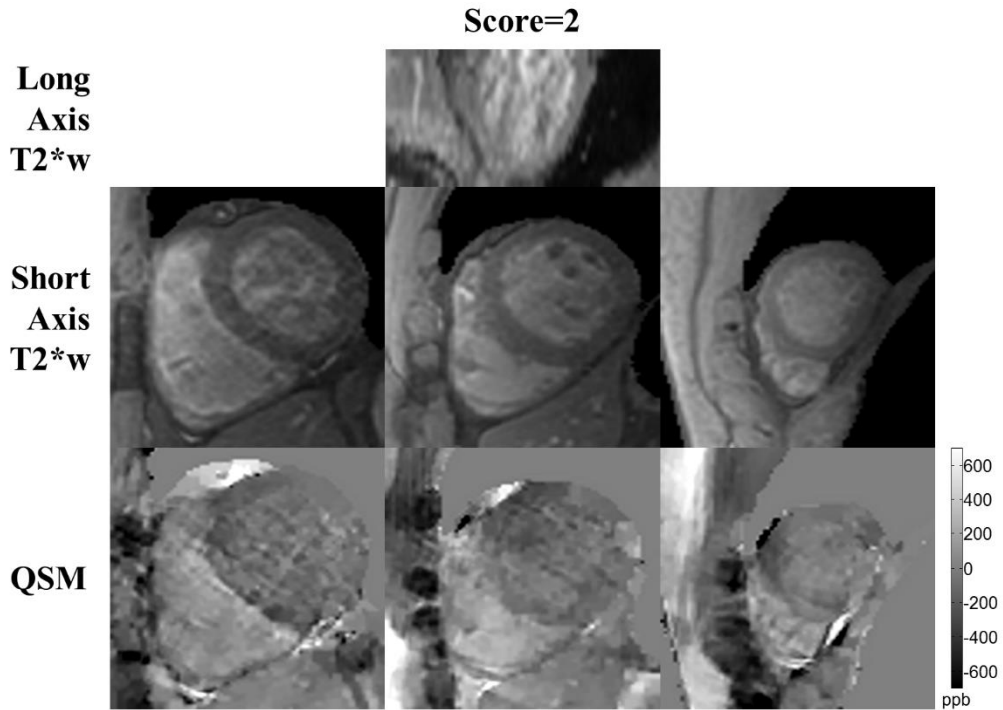


Figure 2.3. A representative cardiac QSM example with reasonable quality. Differential susceptibility between the left and right sides of the heart can be seen. Magnitude images reformatted into long axis in the top row, short axis magnitude images in the middle row, and corresponding QSM in the bottom row. Columns represent basal (left), mid, and apical (right) chambers.

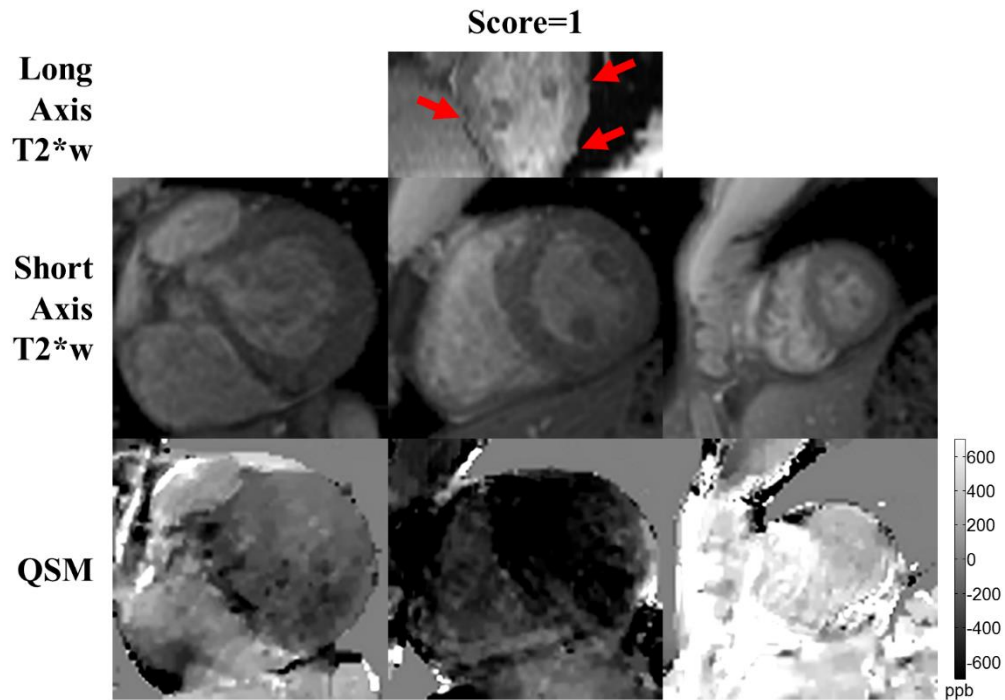


Figure 2.4. Representative cardiac QSM example with poor quality. The susceptibility contrast is mostly degraded by the shadowing artifacts. The long axis magnitude image (top) showed that there were a few misregistered slices (red arrows), suggesting inconsistent breath holding positions.

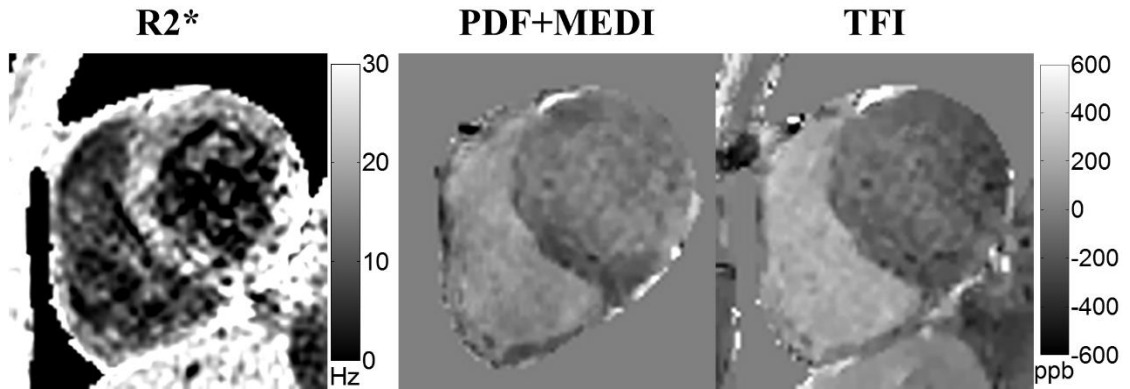


Figure 2.5. Comparison of  $R2^*$  map, and QSM maps computed using PDF+MEDI and TFI algorithms. In this example, both QSM maps demonstrated much improved blood contrast between the right and left ventricles than the  $R2^*$  map does. Between the two QSM maps, the result from TFI has better RV to LV contrast. The susceptibility difference between RV and LV blood was 327.4 ppb (corresponding to 77.0% SvO<sub>2</sub>) with TFI, and 138.6 ppb (90.1% SvO<sub>2</sub>, well above the normal range) with PDF+MEDI.

## CHAPTER 3

# FREE BREATHING THREE-DIMENSIONAL CARDIAC QUANTITATIVE SUSCEPTIBILITY MAPPING FOR DIFFERENTIAL CARDIAC CHAMBER BLOOD OXYGENATION – INITIAL VALIDATION IN PATIENTS WITH CARDIOVASCULAR DISEASE INCLUSIVE OF DIRECT COMPARISON TO INVASIVE CATHETERIZATION

### *3.1 Abstract*

**Background:** Differential blood oxygenation between left (LV) and right ventricles ( $\Delta SaO_2$ ) is a key index of cardiac performance; LV dysfunction yields increased RV blood pool deoxygenation. Deoxyhemoglobin increases blood magnetic susceptibility, which can be measured using an emerging MRI technique, Quantitative Susceptibility Mapping (QSM) – a concept previously demonstrated in healthy volunteers using a breath-hold 2D imaging approach (2D<sub>BH</sub>QSM). This study tested utility of a novel 3D free-breathing QSM approach (3D<sub>NAV</sub>QSM) in normative controls, and validated 3D<sub>NAV</sub>QSM for non-invasive  $\Delta SaO_2$  quantification in patients undergoing invasive cardiac catheterization (cath).

**Methods:** Initial control (n=10) testing compared 2D<sub>BH</sub>QSM (ECG-triggered 2D gradient echo acquired at end-expiration) and 3D<sub>NAV</sub>QSM (ECG-triggered navigator gated gradient echo acquired in free breathing using a phase-ordered automatic window selection algorithm to partition data based on diaphragm position). Clinical

testing was subsequently performed in patients being considered for cath, including 3D<sub>NAV</sub>QSM comparison to cine-CMR quantified LV function (n=39), and invasive-cath quantified  $\Delta SaO_2$  (n=15). QSM was acquired using 3T scanners; analysis was blinded to comparator tests (cine-CMR, cath).

**Results:** 3D<sub>NAV</sub>QSM generated interpretable QSM in all controls; 2D<sub>BH</sub>QSM was successful in 6/10. Among controls in whom both pulse sequences were successful, RV/LV susceptibility difference (and  $\Delta SaO_2$ ) were not significantly different between 3D<sub>NAV</sub>QSM and 2D<sub>BH</sub>QSM (251.7±39ppb [17.5±3.1%] vs. 211.3±29ppb [14.7±2.0%]; p=0.39). Acquisition times were 30% lower with 3D<sub>NAV</sub>QSM (4.7±0.9 vs. 6.7±0.5 minutes, p=0.002), paralleling a trend towards lower LV mis-registration on 3D<sub>NAV</sub>QSM (p=0.14). Among cardiac patients (63±10yo, 56% CAD) 3D<sub>NAV</sub>QSM was successful in 87% (34/39) and yielded higher  $\Delta SaO_2$  (24.9±6.1%) than in controls (p<0.001). QSM-calculated  $\Delta SaO_2$  was higher among patients with LV dysfunction as measured on cine-CMR based on EF (29.4±5.9% vs. 20.9±5.7%, p<0.001) or stroke volume (27.9±7.5% vs. 22.4±5.5%, p=0.013). Cath measurements (n=15) obtained within a mean interval of 4±3 days from MRI demonstrated 3D<sub>NAV</sub>QSM to yield high correlation (r=0.87, p<0.001), small bias (-0.1%), and good limits of agreement (±8.6%) with invasively measured  $\Delta SaO_2$ .

**Conclusion:** 3D<sub>NAV</sub>QSM provides a novel means of assessing cardiac performance. Differential susceptibility between the LV and RV is increased in patients with cine-CMR evidenced LV systolic dysfunction; QSM-quantified  $\Delta SaO_2$  yields high correlation and good agreement with the reference of invasively-quantified  $\Delta SaO_2$ .

### 3.2 Introduction

Differential blood oxygenation between the left and right heart ( $\Delta SaO_2$ ) is an established index of cardiac performance; left ventricular (LV) dysfunction results in stagnant blood flow – resulting in increased time for organ extraction of oxygen from blood and delivery of a greater fraction of deoxygenated blood to the right heart.

Increased  $\Delta SaO_2$  has been shown to predict adverse prognosis in patients with heart failure with and without pulmonary hypertension (78-80) for whom it is commonly used to guide management (81,82). However, in current clinical practice, oxygen saturation is measured via invasive catheterization (cath). Non-invasive imaging methods to measure oxygenation in the heart are limited, prohibiting non-invasive quantification of cardiac blood pool oxygenation as part of routine clinical evaluation (31,33,40,83-87). Given the fact that invasive catheterization entails procedural risks and can be challenging in critically ill patients (26-28), a non-invasive imaging method to accurately measure cardiac oxygenation would be of substantial clinical utility.

Quantitative susceptibility mapping (QSM) is an emerging MRI technique that enables quantification of diamagnetic and paramagnetic materials (6,7,21,43,45,46,88). Iron is a magnetically active element contained in hemoglobin that is central to oxygen transport - it is weakly diamagnetic when bound to oxygen, and paramagnetic when deoxygenated (89). This change in magnetic susceptibility by deoxyheme (47,48), provides a metric by which QSM can measure blood oxygen saturation. Prior work has validated QSM tissue characterization, including liver and brain iron content

(21,42,67,90). Regarding blood oxygenation, a pilot study by our group showed cardiac QSM to be feasible in normal controls (23). However, a 2D acquisition strategy was employed, which is suboptimal for imaging patients in whom breath-holding is often compromised. To address this, a free-breathing 3D QSM approach was developed that uses diaphragmatic navigator gating to track respiratory position. This study compared 3D free-breathing QSM ( $3D_{NAV}QSM$ ) to 2D breath held QSM ( $2D_{BH}QSM$ ) in controls, as well as to the reference of  $\Delta SaO_2$  measured in patients undergoing invasive cardiac catheterization.

### **3.3 Methods**

#### *Study Population*

$3D_{NAV}QSM$  was first compared to  $2D_{BH}QSM$  among normative controls without clinically reported cardiovascular conditions or associated risk factors to test the relative performance in a cohort able to undergo prolonged imaging inclusive of both pulse sequences. Next, a second group of normative controls were scanned and rescanned to test the reproducibility of  $3D_{NAV}QSM$   $\Delta SaO_2$  measurement. The second group of volunteers was asked to get off and then get back on the table between the two scans. All controls were without self-reported cardiovascular disease or atherosclerosis risk factors.

After initial testing,  $3D_{NAV}QSM$  was then performed among clinical patients who were being considered for or had undergone invasive catheterization to quantify blood oxygen saturation. Catheterization was performed by experienced physicians using standard techniques; intracardiac blood samples were obtained under baseline

conditions (without supplemental O<sub>2</sub>) and used to calculate  $\Delta SaO_2$  between the left and right heart. To test the effect of gadolinium in  $\Delta SaO_2$  measurement, QSM were obtained in 3 healthy volunteers and in 4 patients both pre-contrast and ~30 minutes post-contrast administration.

This study was performed at Weill Cornell Medicine (WCM; New York, NY). All participants (controls and patients) provided written informed consent for research participation. This protocol was performed with the approval from the WCM Institutional Review Board.

#### Data Acquisition

MRI was performed using commercial 3.0T scanners (750/SIGNA, GE Healthcare, Waukesha WI). 3D<sub>NAV</sub>QSM and 2D<sub>BH</sub>QSM imaging parameters were identical between healthy subjects and patients: 1<sup>st</sup>TE/ $\Delta$ TE/#TE/TR/BW = 2.3ms/3.6ms/5/20ms/111.1kHz, acquisition matrix=192x144, slice thickness = 5 mm, views per heartbeat = 10, parallel imaging factor = 2. Full 3D flow compensation gradients were implemented for both 2D<sub>BH</sub>QSM and 3D<sub>NAV</sub>QSM to minimize the phase generated by intra-chamber blood flow (47). To shorten 3D<sub>NAV</sub>QSM scan time, 75% partial Fourier acquisition was applied in the phase and slice encoding direction. Typical resolution is 1.5x1.5x5mm<sup>3</sup>, 40cm<sup>2</sup> FOV, and 20 slices per scan. Furthermore, 2D<sub>BH</sub>QSM used cardiac gating and breath-holding, and 3D<sub>NAV</sub>QSM used cardiac and respiratory gating (with diaphragm navigator) to ensure the acquisition of data at a consistent cardiac and respiratory phase. QSM was performed using non-contrast MRI in controls, and at the end of clinical exams in patients, which was approximately ~30

minutes post-gadolinium (Dotarem [gadoterate meglumine]; 0.2mmol/kg) infusion. As stated above, in 3 healthy subjects and 4 patients, QSM was acquired both pre- and post-contrast. Routine cine images were also acquired with typical parameters: TE = 1.4ms, TR = 3.8ms, FA=60°, bandwidth=781Hz/Px, resolution: 1.5x1.5x6mm<sup>3</sup>, and SENSE acceleration R=2.

2D<sub>BH</sub>QSM employed a conventional ECG-triggered multi-echo gradient echo sequence, for which data was acquired during end-expiration (~12s per breath-hold). 3D<sub>NAV</sub>QSM employed a tailored ECG-triggered navigator gated multi-echo gradient echo sequence, for which data was acquired during free breathing: a cross pair diaphragmatic navigator was used to track respiratory motion (91,92). A 2-bin phase-ordered automatic window selection (PAWS) gating algorithm (4mm effective gating window) was used to tailor data acquisition according to diaphragm position in real-time (22). In PAWS, each diaphragm position falls within a 2mm bin for which k-space is acquired from alternating directions from bin to bin. The scan is complete when two adjacent bins have acquired all necessary k-space lines. Two navigator echoes were used in each heartbeat. The first navigator was acquired immediately before acquisition and used for PAWS gating. The second navigator was acquired immediately after data acquisition and used to provide additional motion suppression: if the difference between diaphragm positions detected by the two navigator echoes was >4mm for a given heartbeat, then the data acquired in that heartbeat were discarded and scheduled to be reacquired in a later heartbeat.

Ancillary imaging was performed to test QSM in relation to conventional cardiac functional/ remodeling indices. Cine-MRI was performed using a conventional steady state free precession pulse sequence, which was acquired in contiguous long and short axis images, the latter of which were segmented to quantify left ventricular end-diastolic and end-systolic chamber volumes for calculation of LV and RV ejection fraction (EF) as well as stroke volume.

### QSM Post Processing

QSM maps were reconstructed by first obtaining a total field map (containing both the local and background field) with the contributions of fat chemical shift removed. This was done using both graph-cut based phase unwrapping (9) and IDEAL water/fat separation (57) with iterative chemical shift update (56). Next, a susceptibility map was obtained using the preconditioned total field inversion method (11). In this work, two regularization terms, similar to the regularization terms described in MEDI+0 (93), were added to the inversion to restrict the susceptibility variations within the right ventricle (RV) and left ventricle (LV) as follows:

$$\mathbf{y}^* = \underset{\mathbf{y}}{\operatorname{argmin}} \quad \frac{1}{2} \|\mathbf{w}(\mathbf{f} - \mathbf{d} \otimes \mathbf{P}\mathbf{y})\|_2^2 + \lambda \|\mathbf{M}_G \nabla \mathbf{P}\mathbf{y}\|_1 \quad [3.1]$$

$$+ \lambda_{RV} \|\mathbf{M}_{RV} \mathbf{P}(\mathbf{y} - \bar{\mathbf{y}}^{RV})\|_2^2 + \lambda_{LV} \|\mathbf{M}_{LV} \mathbf{P}(\mathbf{y} - \bar{\mathbf{y}}^{LV})\|_2^2$$

The first two terms are the data fidelity term and structure consistency regularization term, respectively, where  $w$  is the SNR weighting,  $f$  is the total field,  $d$  is the dipole kernel,  $\otimes$  is the convolution operator,  $P$  is the preconditioner,  $\lambda$  is the regularization parameter,  $M_G$  is a binary edge mask constructed by retaining the highest 70% of gradients of the T2\*w image obtained by taking the square root of the sum of squares

GRE images across echoes), and  $\nabla$  is the gradient operator (6),  $P$  is a binary mask that is 1 inside the region of interest (ROI) and a larger value,  $P_{outside}$ , outside of the ROI (see below). The final QSM map,  $\chi$ , is then  $\chi = Py^*$ . The last two terms constrain the susceptibility variation within the RV and the LV blood pools, where  $\lambda_{RV}$  and  $\lambda_{LV}$  are the regularization parameters,  $M_{RV}$  and  $M_{LV}$  are the mask for RV and LV obtained through manual segmentation on the GRE images.  $\bar{y}^{RV}$  and  $\bar{y}^{LV}$  are the average susceptibility over the RV and LV blood pools, respectively. In this study, the values of  $P_{outside} = 20$ ,  $\lambda = 1/1000$ , and  $\lambda_{RV} = \lambda_{LV} = 1/20$  were empirically determined in an initial study in healthy subjects via visual inspection of the corresponding QSM, and then fixed for subsequent subjects.

To account for potential field errors from water/fat separation, an iterative reweighted least squares fitting method, MERIT (94), was implemented to modify noise weighting of fat voxels (fat fraction > 30%) in each Gauss-Newton iteration to account for residual fat chemical shift not removed from the total field in the water/fat separation step. After iteration  $i$  in the Gauss-Newton solver, the noise weighting,  $w$ , in fat voxels for the next iteration  $i + 1$  was recalculated as  $w_{i+1}^* =$

$$\begin{cases} w_i & \frac{\rho_i}{2\sigma_i} \leq 1 \\ w_i/(\rho_i/2\sigma_i) & \frac{\rho_i}{2\sigma_i} > 1 \end{cases}, \text{ where } \rho_i = w_i |f - d \otimes Py_i| \text{ is the voxel-by-voxel data term}$$

residual for the  $i$ th iteration, and  $\sigma_i$  is the standard deviation of  $\rho_i$  over all voxels.

The differential susceptibility between RV and LV blood pools ( $\Delta\chi$ ) was converted to blood oxygenation difference ( $\Delta SaO_2$ ) using an established formula (23):

$$\Delta SaO_2 = \frac{-\Delta\chi}{4H\chi_{deoxyheme}} \quad [3.2]$$

Where  $\chi_{deoxyheme}$  is the molar susceptibility of deoxyheme such that  $4\chi_{deoxyheme} = 151.054 \text{ ppb} \frac{\text{ml}}{\mu\text{mol}}$  is the molar susceptibility of a fully deoxygenated deoxyhemoglobin (95).  $H = 4Hct \frac{\rho_{RBC,Hb}}{M_{Hb}}$  is the heme concentration in blood (in  $\mu\text{mol/ml}$ ), where  $Hct$  is the hematocrit,  $\rho_{RBC,Hb} = 0.34 \frac{\text{g}}{\text{ml}}$  is the mass concentration of hemoglobin in a red blood cell, and  $M_{Hb} = 64450 \times 10^{-6} \frac{\text{g}}{\mu\text{mol}}$  is the molar mass of deoxyhemoglobin. For controls,  $Hct$  was assumed to be 47% in men and 42% in women. These values were obtained by taking the average of the range in men and in women observed in a prior study (96). For patients,  $Hct$  data was obtained from peripheral blood samples. Note that the current approach only measures the susceptibility difference between RV and LV blood pools (therefore only measures the oxygen saturation difference between the RV and LV blood pools), bypassing the need to reference the blood susceptibility to a susceptibility reference (typically chosen to be water), which may or may not replicate in-vivo conditions. Post-processing was performed using MATLAB (The MathWorks, Natick, MA, USA).

### QSM Performance Scores

Image quality (of GRE images) was assessed using two different approaches. Image quality for individual short axis slices (in-plane data) was scored semi-quantitatively based on visually assessed motion artifact/endocardial blurring (0 = severe, 1 = moderate, 2 = negligible). Scoring was performed by consensus of three experienced

physicians (JWW, JK, JK). Through plane image quality was measured quantitatively based on the magnitude of slice misregistration (from both in-plane and through-plane motion), which was measured as the standard deviation of the second derivative along heart surface curves that were obtained from two perpendicular reformatted long-axis images that depict the heart-lung interface (23): a higher standard deviation corresponded to lower through plane image quality (less smooth heart-lung interface).

### Statistical Methods

Continuous variables were compared between groups using Student's t-tests (expressed as mean  $\pm$  standard deviation). 2D and 3D image quality scores were compared using a two-tailed Wilcoxon paired-sample signed rank test. Pearson correlation coefficients and Deming linear regression (97) were used to test the associations between the QSM based  $\Delta SaO_2$  and the invasively quantified  $\Delta SaO_2$ , as were the Bland Altman plot. Two-sided  $p < 0.05$  was deemed indicative of statistical significance. Statistical analyses were performed using MATLAB (MathWorks, Natick, MA, USA) and Prism 7 (GraphPad Software, San Diego, CA, USA).

## **3.4 Results**

### Normative Controls

$3D_{NAV}QSM$  and  $2D_{BH}QSM$  were acquired in a cohort of 10 asymptomatic controls ( $31 \pm 4$  yo, 60% male). Whereas in-plane image quality was higher for  $2D_{BH}QSM$  compared to  $3D_{NAV}QSM$  ( $2.0 \pm 0.0$  vs.  $1.1 \pm 0.4$ ,  $p < 0.001$ ), through plane image quality

tended to be higher (lower slice misregistration) for 3D<sub>NAV</sub>QSM compared to 2D<sub>BH</sub>QSM ( $1.0 \pm 0.2$  vs.  $1.5 \pm 0.8$ ,  $p=0.14$ ).

3D<sub>NAV</sub>QSM successfully generated interpretable QSM in all 10 controls, whereas 2D<sub>BH</sub>QSM was successful in 6/10 of cases. **Figure 3.1** provides a representative example of as an interpretable QSM dataset acquired by 3D<sub>NAV</sub>QSM despite non-interpretable 2D<sub>BH</sub>QSM (**1A**), as well an interpretable QSM dataset concordantly acquired by 2D<sub>BH</sub>QSM and 3D<sub>NAV</sub>QSM (**1B**).

In all cases for which 2D<sub>BH</sub>QSM was uninterpretable, failure was due to slice misregistration between sequential LV short axis datasets. Consistent with this, quantitative slice misregistration was over 2-fold higher in cases for which 2D<sub>BH</sub>QSM failed ( $n=4$ ) compared to cases ( $n=6$ ) in which 2D<sub>BH</sub>QSM yielded diagnostic results ( $2.3 \pm 0.4$  vs.  $1.0 \pm 0.2$ ,  $p<0.001$ ). There was no significant difference in slice misregistration between 3D<sub>NAV</sub>QSM and 2D<sub>BH</sub>QSM in exams for which both sequences were successful ( $1.0 \pm 0.1$  vs  $1.0 \pm 0.2$ ,  $p=1.0$ ).

Regarding data acquisition time, results demonstrated 3D<sub>NAV</sub>QSM to yield a 30% reduction compared to 2D<sub>BH</sub>QSM ( $4.7 \pm 0.9$  vs.  $6.7 \pm 0.5$  minutes,  $p=0.002$ ) attributable to the interval time between each breath-hold. Navigator efficiency for 3D<sub>NAV</sub>QSM was  $54 \pm 12\%$ . Reduced scan time yielded by 3D<sub>NAV</sub>QSM remained significant even among controls in whom both pulse sequences produced diagnostic results and acquisitions were reduced by an average of 37% ( $4.3 \pm 1.4$  vs.  $6.8 \pm 0.4$  minutes,  $p=0.002$ ), with navigator efficiency for 3D<sub>NAV</sub>QSM  $56 \pm 16\%$ .

Regarding QSM results, mean RV/LV susceptibility difference was not significantly different between 3D<sub>NAV</sub>QSM and 2D<sub>BH</sub>QSM acquired in controls in whom the latter pulse sequence was successful (251.7±39ppb vs. 211.3±29ppb, p=0.39), corresponding to  $\Delta SaO_2$  of 17.5±3.1% and 14.7±2.0%, respectively. Of note, the RV/LV susceptibility difference (and  $\Delta SaO_2$ ) calculated using 3D<sub>NAV</sub>QSM was not significantly different when compared between controls with and without diagnostic results yielded by 2D<sub>BH</sub>QSM (251.7±39 ppb vs. 250.0±33 ppb, p=0.87 [17.5±3.1% vs. 17.3±2.4%]).

Reproducibility of 3D<sub>NAV</sub>QSM (as tested in 5 volunteers) was high, as evidenced by small mean differences (-0.4%) and reasonable limits of agreement (±2.2%) between data acquired during two separate scans (**Figure 3.2**).

### Clinical Patients

3D<sub>NAV</sub>QSM was acquired in 39 patients whose population characteristics are shown in **Table 3.1**. In this group, QSM data was successfully obtained in 87% (34/39) of cases. In 5 cases, 3D<sub>NAV</sub>QSM yielded non-diagnostic results (non-physiological equivalence between LV and RV blood oxygenation) – all of which had substantial motion artifact. In the remainder of patients (n=34), RV/LV susceptibility difference calculated using 3D<sub>NAV</sub>QSM was substantial (298.3±72.0 ppb), corresponding to a  $\Delta SaO_2$  of 24.9±6.1% (p<0.001 vs. controls). Image acquisition time in the overall clinical cohort was 6.9±2.8 minutes; increased acquisition time tended to be longer among patients compared to controls (4.7±0.9 minutes; p=0.04) due to greater respiratory variability and lower navigator efficiency in patients (36±12% vs. 54±12%).

Among the overall clinical cohort in whom QSM was successful (n=34), results varied in relation to LV systolic dysfunction as quantified using cine-CMR. As shown in **Figure 3.3A**, a greater  $\Delta SaO_2$  on QSM was observed among patients with LV dysfunction (EF<50%) as quantified by cine-CMR (29.4±5.9% vs. 20.9±5.7%, p<0.001). Similarly, patients in the bottom median of cine-CMR quantified LV stroke volume had greater  $\Delta SaO_2$  on QSM (27.9±7.5% vs. 22.4±5.5%, p=0.013).

In a subgroup of 15 patients who had successful QSM, invasive cardiac catheterization (cath) was available as a reference standard for heart chamber oxygenation: all patients underwent cath for evaluation of known/suspected heart failure – 47% had left ventricular systolic dysfunction and 53% had primary pulmonary hypertension. Mean interval between tests (cath, MRI) was 4±3 days (range 0-12 days). **Figure 3.3B** provides representative patient examples, including close agreement with invasively quantified  $\Delta SaO_2$  and increased magnitude of difference in context of LV dysfunction. As shown in **Figure 3.4A**, QSM yielded good correlation with invasively quantified  $\Delta SaO_2$  (r=0.87, p<0.001); corresponding to small bias (-0.1%) and reasonable limits of agreement (±8.6%) between the two tests (**Figure 3.4B**). **Table 3.2** provides a breakdown of QSM results on a per-patient basis, together with invasive cath data and corresponding indices of LV function. Consistent with results in the overall clinical cohort, patients who underwent cath demonstrated LV systolic dysfunction (EF<50%) to be associated with greater  $\Delta SaO_2$  on both invasive testing (32.9±3.7% vs. 21.2±6.9%, p=0.002) and non-invasive QSM (33.9±5.6% vs. 21.2±5.8%, p<0.001).

### Cardiac QSM before and after contrast administration

Cardiac QSM was obtained successfully in all 7 subjects who were scanned both before and after contrast administration. As shown in **Figure 3.5**, the  $\Delta SaO_2$  measured from pre- and post-contrast QSM matched very well (slope=1.04,  $r=0.97$ ,  $p<0.001$ ), with a small bias (-0.7%), small limits of agreement ( $\pm 1.9\%$ ), and a small mean absolute difference (0.9%).

### **3.5 Discussion**

This is the first study to test the free breathing 3D cardiac QSM for non-invasive measurement of blood oxygenation, inclusive of validation data provided by cine-CMR quantified cardiac remodeling and invasively quantified oxygen saturation in cardiac patients. Key findings are as follows: first, among a normative test cohort, 3D<sub>NAV</sub>QSM more commonly yielded interpretable results than did 2D<sub>BH</sub>QSM (100% vs. 60%) and did so within shorter scan time ( $4.7\pm 0.9$  vs.  $6.7\pm 0.5$  minutes,  $p=0.002$ ). Second, 3D<sub>NAV</sub>QSM performed robustly in a subsequent cohort of 39 patients with established cardiovascular disease, among whom results demonstrated differential LV/RV susceptibility in 87% (34/39) of cases: magnitude of  $\Delta SaO_2$  differed in relation to LV systolic dysfunction as quantified on cine-CMR, as evidenced by greater  $\Delta SaO_2$  on QSM among patients with impaired LVEF ( $<50\%$ ) compared to those with preserved LVEF ( $29.4\pm 5.9\%$  vs.  $20.9\pm 5.7\%$ ,  $p<0.001$ ), and similar results when QSM results were compared in relation to decreased LV function as stratified based on stroke volume ( $p=0.013$ ). Third, among a subgroup of patients undergoing invasive catheterization, 3D<sub>NAV</sub>QSM yielded good correlation with invasively

quantified  $\Delta SaO_2$  ( $r=0.87$ ,  $p<0.001$ ), corresponding to reasonably small bias and limits of agreement ( $-0.1\%$  and  $\pm 8.6\%$ , respectively) between approaches.

While our data validate cardiac QSM for differential chamber oxygenation, it is important to recognize that prior research has applied different MRI approaches for this purpose. Most previous approaches are based on measurement of blood MR relaxation times ( $T_2$ ,  $T_2^*$ , and  $T_1$ ) (31,33,40,83,84,86,87,98). However, conventional methods based on longitudinal ( $T_1$ ) or transverse ( $T_2$ ) relaxation properties can be challenging to apply clinically. For example, the dependence of spin echo  $T_2$  on oxygenation is well understood, but in practice requires measuring several model parameters in addition to oxygenation, thereby potentially limiting accuracy or complicating clinical implementation. Recently, an oxygen saturation measurement based on acquiring multiple  $T_2$  maps using a 2D  $T_2$  prepared SSFP sequence designed to overcome limitations of previous  $T_2$  based methods, was shown to provide good agreement with invasive catheterization based measurement in an animal study. A comparison between this promising approach and our proposed QSM approach is warranted in a future study (85). An alternative approach consists of quantifying the magnetic susceptibility of blood. The physical model relating blood susceptibility to oxygen saturation is simpler than that for  $T_2$  as it is linear with the slope a known physical constant. The magnetic susceptibility of venous blood can be computed from the MR image phase by geometric modeling (41,99-102). Mapping of magnetic susceptibility throughout the 3D field of view, as is done in QSM, enables measurement of oxygen saturation of any vascular structure (including the heart) by

simple ROI analysis (47,48,103). Our current data extends on prior work by our group that has shown QSM to provide an index of hemorrhage (47,67), as well as an index of metabolism and oxygen utilization in the brain (104,105).

Our QSM results regarding differential LV and RV blood oxygen saturation are consistent with values reported in prior literature as well as expected differences between subjects with and without cardiovascular disease. Regarding control data,  $\Delta SaO_2$  measured from 3D<sub>NAV</sub>QSM ( $17.5 \pm 3.1\%$ ) was in agreement with a prior study that reported  $\Delta SaO_2$  in healthy subjects undergoing invasive cardiac catheterization (106), in which a mean difference of 18.8% was reported (arterial: 97.3%, venous: 78.5%).  $\Delta SaO_2$  as measured in controls were also lower than that in patients with cardiovascular disease ( $17.5 \pm 3.1\%$  vs.  $24.9 \pm 6.1\%$ ,  $p < 0.001$ ), consistent with expected physiological differences between the two groups. Among our subgroup of patients with cath validation (n=15), QSM derived  $\Delta SaO_2$  demonstrated a linear relationship with invasive measurements, and bias between the two oxygenation measurement approaches was small.

One key technical innovation in our current study concerns use of navigator technology for free breathing 3D QSM. The conventional cardiac 2D<sub>BH</sub>QSM approach generates data by imaging LV (short axis) slices individually via sequential breath-holds in order to reconstruct a 3D field map. When one or more of these breath-holds is acquired at a different respiratory position than the others, the resulting field map will not be a true 3D volume, and the QSM map will contain artifacts as the reconstruction model assumes a continuous 3D dataset as input. The susceptibility

inversion problem is inherently 3D, given that susceptibility changes within one region of a given structure (e.g. RV blood pool) affects the field in the surrounding areas in all three (x, y, z) spatial directions: this stems from the fact that the field is a 3D convolution of the underlying 3D susceptibility distribution with the dipole kernel. The 3D<sub>NAV</sub>QSM approach has no inherent mis-registration limitation, and the success of 3D<sub>NAV</sub>QSM acquisition depends on navigator accuracy in motion tracking. These aspects of QSM reconstruction may explain our seemingly discordant finding regarding GRE image quality and diagnostic performance of the two QSM pulse sequences tested in our study: even though GRE images from the 2D<sub>BH</sub>QSM sequence were assigned higher image scores than images from the 3D<sub>NAV</sub>QSM sequence, 2D<sub>BH</sub>QSM failed to generate interpretable QSM more often than did 3D<sub>NAV</sub>QSM and this failure was primarily attributable to slice mis-registration.

Several limitations should be noted. First, scan time of 3D<sub>NAV</sub>QSM sequence is long (~4-7 minutes) compared to other routine clinical sequences. One potential approach to shorten scan time is to increase parallel acceleration factor, use compressed sensing (73,107), and/or apply data acquisition strategies such as echo planar readout (72) or echo sharing methods (74). Non-Cartesian acquisitions that allow for self-gating (108) and multi-phase reconstruction (109) are also alternatives to shorten cardiac QSM. A second limitation to the current 3D<sub>NAV</sub>QSM approach is that the respiratory motion is tracked by diaphragm navigator, which is known to fail occasionally (110). More advanced navigator techniques such as cardiac fat navigator can be used to improve success rates (91,92,111-113). A third issue to consider is that QSM was performed during non-contrast imaging in controls, and at the end of contrast-enhanced exams

(~30 minutes post gadolinium infusion) in patients. Whereas gadolinium changes blood susceptibility, prior data has shown gadolinium to be near completely cleared from myocardium, and to be well mixed in the intravascular space at our imaging time point (114,115). Accordingly, QSM calculations were based on the premise that contrast blood pool concentration was constant across cardiac chambers, such that gadolinium contributions to susceptibility in the LV and RV cancel out when computing differential oxygenation. Fourthly, QSM validation in this study was derived from cardiac remodeling indices in 39 cardiac patients of whom 15 had invasive catheterization for evaluation of known or suspected heart failure; further validation in a larger clinical cohort including patients undergoing catheterization for different indications is warranted. Finally, it should be noted that whereas interval between QSM and invasive cath was short (mean  $4\pm 3$  days, median 2 days [IQR 1-5 days]), cardiac chamber oxygenation could have varied during this time, thus resulting in discordance between tests. Future research with simultaneous invasive and MRI oxygenation measurements in animal models could be of utility for further validation of QSM, as well as comparisons with alternative pulse sequences for oxygenation quantification (i.e. T2). Nevertheless, our current findings that 3D navigator QSM was feasible among a clinical cohort in whom it generally agreed with differential oxygenation saturation as measured invasively is of substantial importance with respect to translational application of this technique, and provides initial proof of concept with respect to clinical implementation.

It should also be noted that heart rate could have impacted our QSM results. This has been shown to be the case for oxygenation methods such as BOLD, which relies on

the magnitude of the MR signal. On the other hand, QSM, which relies on the phase of the MR signal, is expected to be relatively insensitive to heart rate because the contributions to the phase (field) induced by the difference in left and right ventricle magnetic susceptibility (oxygenation) are not affected by heart rate. Further research is warranted to specifically assess physiologic factors impacting QSM, as well as to validate this pulse sequence in a larger clinical cohort including patients undergoing catheterization for different indications.

### **3.6 Conclusion**

In conclusion, results of this study provide validation of free breathing 3D cardiac QSM as an index of cine-CMR evidenced LV dysfunction and differential LV/RV oxygen saturation as measured by invasive catheterization. Future research is necessary to test accelerated free-breathing QSM strategies, refine cardiac QSM for myocardial tissue characterization, and validate QSM-derived blood oxygenation for non-invasive stratification of heart failure symptoms and prognostic outcomes.

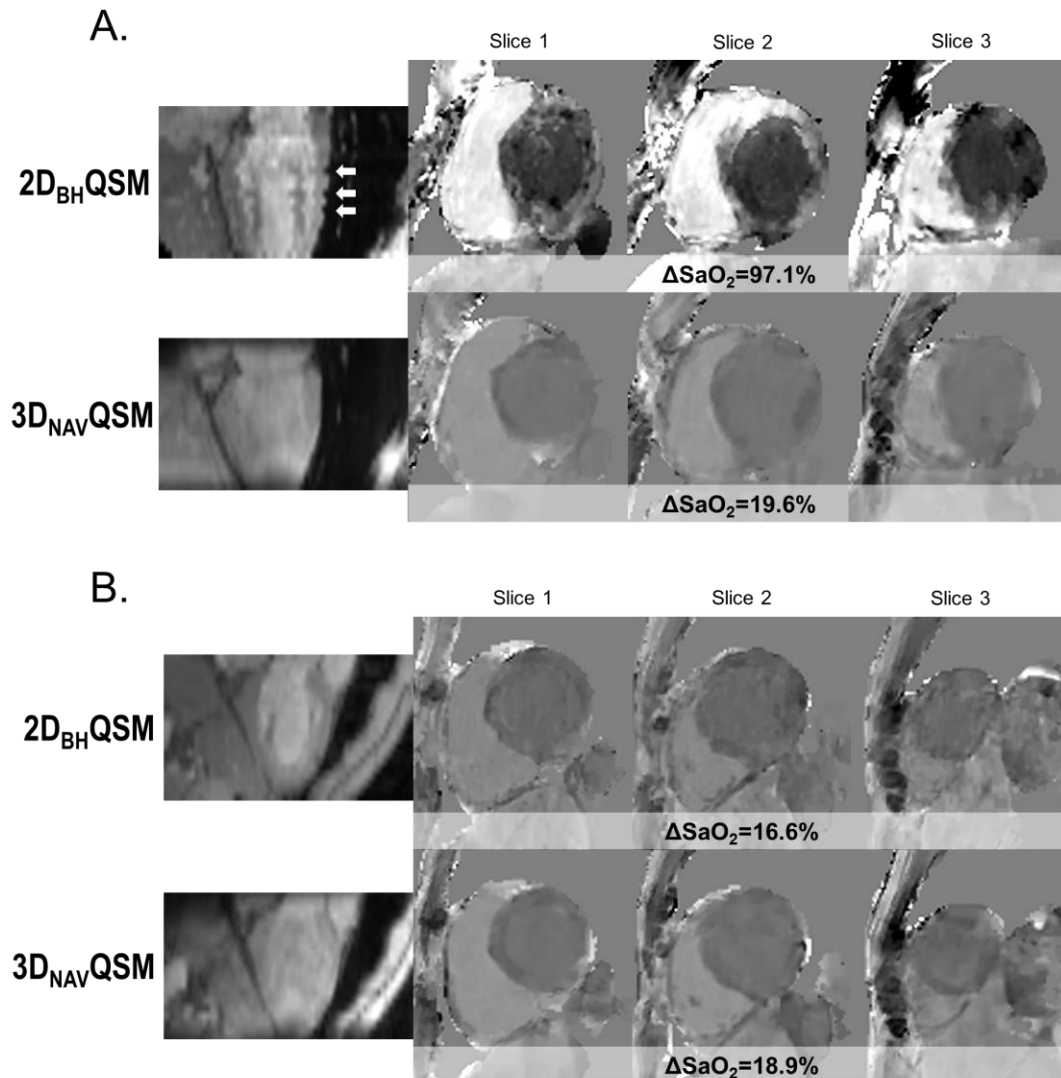


**Figure 3.1. Representative Examples of Cardiac QSM in Normative Controls.**

**1A.** Unsuccessful 2D<sub>BH</sub>QSM due to slice mis-registration (white arrows) attributable to inconsistent breath-hold positions, resulting in non-diagnostic QSM map.

Corresponding 3D<sub>NAV</sub>QSM was successful, yielding physiologic differential oxygen saturation between the left and right ventricles.

**1B.** Successful 2D<sub>BH</sub>QSM and 3D<sub>NAV</sub>QSM, resulting in equivalent QSM maps.

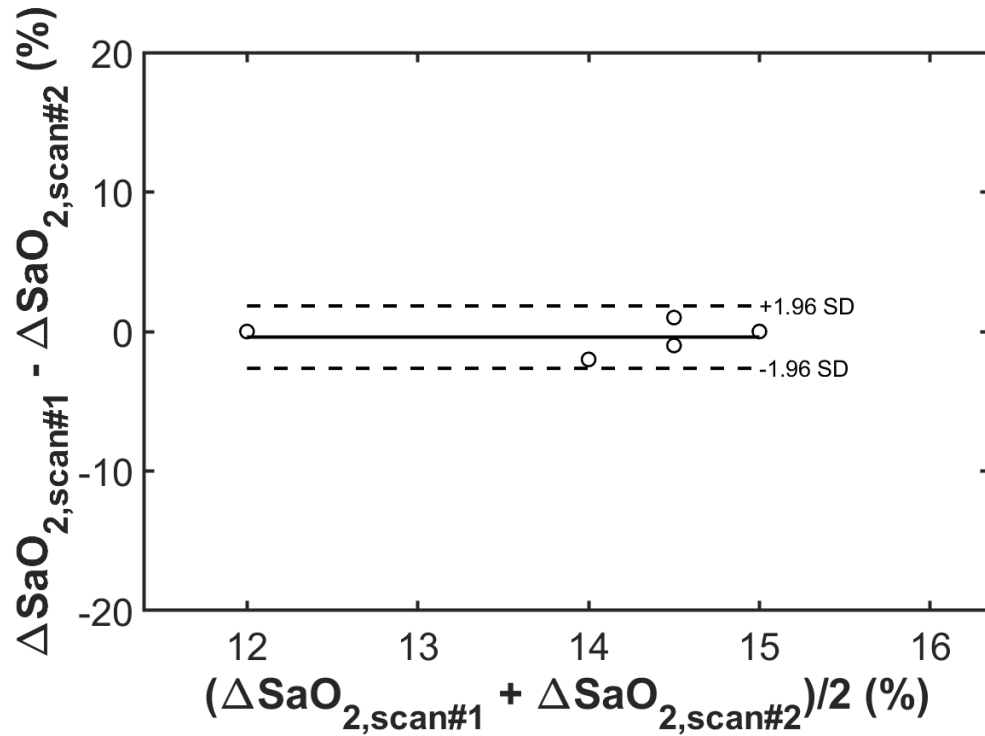


**Figure 3.2.  $\Delta SaO_{2,QSM}$  reproducibility experiment in normative controls**

N=5 normative controls were scanned and rescanned to test the reproducibility of QSM based  $\Delta SaO_2$  measurement. The  $\Delta SaO_2$  measured by QSM between the two scans were very similar: small bias (-0.4%) and reasonable limits of agreement ( $\pm 2.2\%$ ).

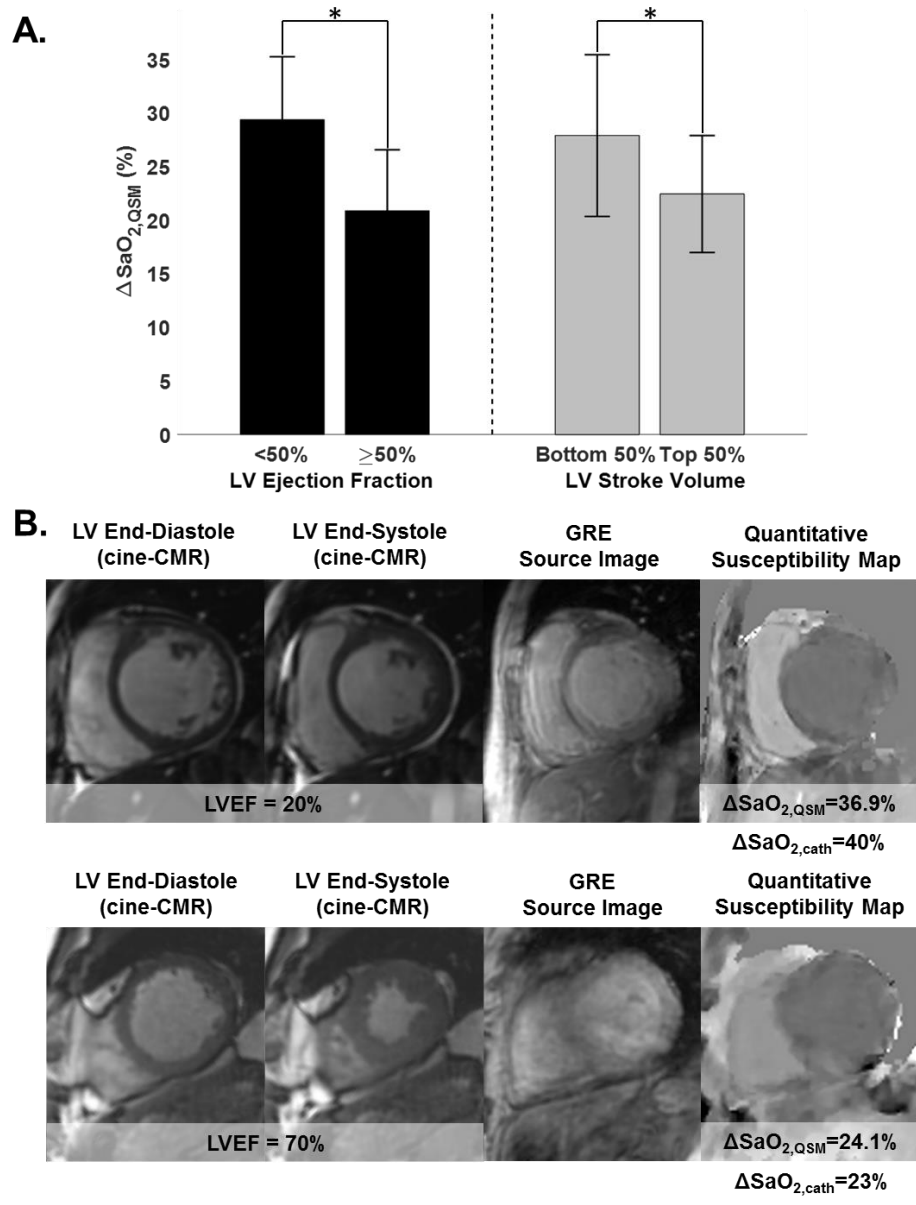
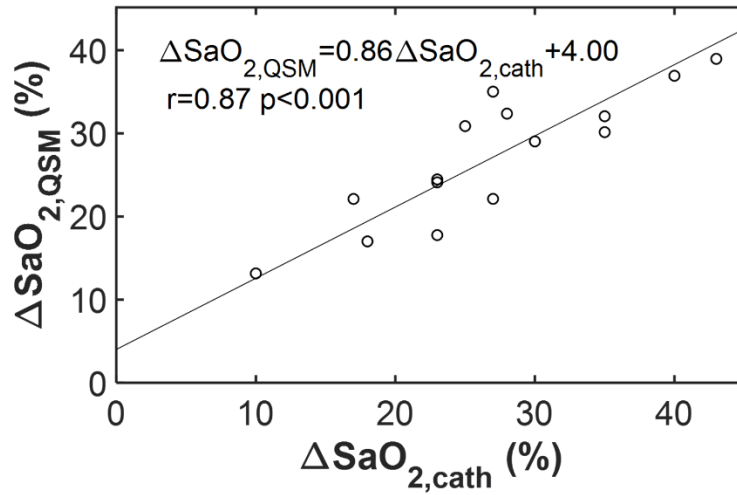


**Figure 3.3. Cardiac QSM in Cardiac Patients**

3A. QSM  $\Delta\text{SaO}_2$  among patients grouped based on presence or absence of LV systolic dysfunction based on cine-CMR quantified ejection fraction (left) and stroke volume (right) (data shown as mean  $\pm$  standard deviation). Note greater  $\Delta\text{SaO}_2$  among patients with LV dysfunction.

**3B.** Two representative examples of QSM maps in cardiac patients. In the top patient, who had severely reduced LV function (EF=20%), QSM measured a marked increase in  $\Delta\text{SaO}_2$  (36.9%), which agreed well with invasive catheterization (40%). In the bottom patient, who had normal LV function (EF=70%), QSM measured  $\Delta\text{SaO}_2$  (24.1%) was within normal limits and was similar to invasive data (23%)

**A.**



**B.**

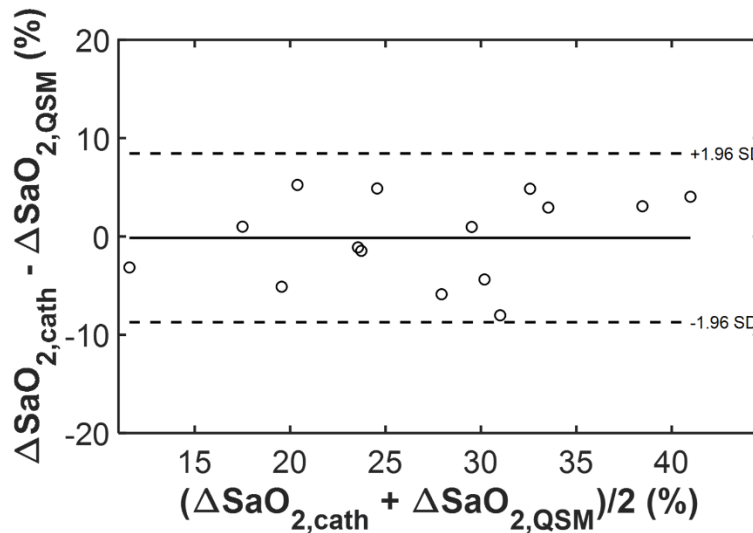


**Figure 3.4. Cardiac QSM in Relation to Invasive Catheterization**

**4A.** Scatter plot examining QSM derived  $\Delta\text{SaO}_2$  in relation to invasive catheterization derived  $\Delta\text{SaO}_2$ . A good correlation ( $r = 0.87$ ,  $p < 0.001$ ) and linear relationship between the two approaches is observed.

**4B.** Bland Altman plot. Note small bias between the two tests (-1%) and moderate limits of agreement ( $\pm 8.6\%$ ).

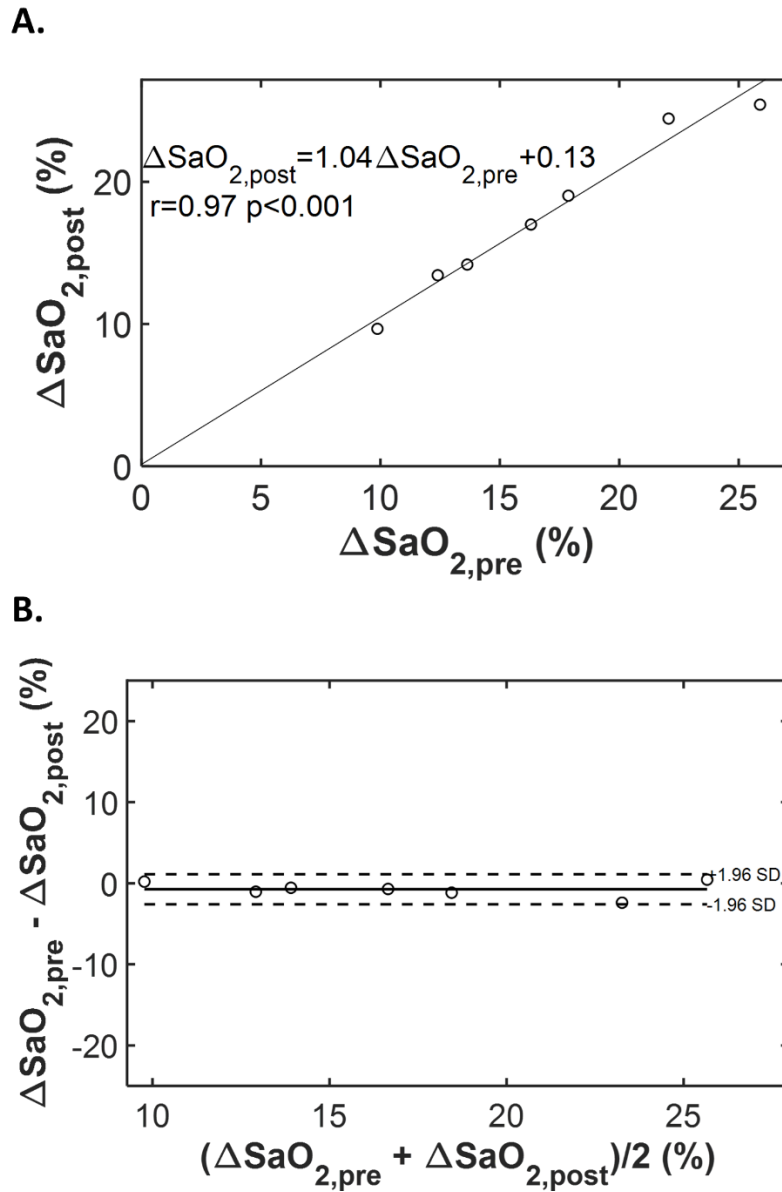


**Figure 3.5. QSM based  $\Delta\text{SaO}_2$  measured pre- and post-contrast administration**

**5A.** Scatter plot examining QSM derived  $\Delta\text{SaO}_2$  pre- and post-contrast administration.

A good correlation and linear relationship between the two measurements is observed.

**5B.** Bland Altman plot showing small bias (-0.7%) and small limits of agreement

( $\pm 1.9\%$ ).

**Table 3.1. Population characteristics.**

<b>Age</b>	63±10yo
<b>Gender (% male)</b>	31% (12)
<b>Known CAD</b>	56% (22)
<b>Pulmonary Hypertension</b>	51% (20)
<b>Atherosclerosis Risk Factors</b>	
Tobacco Use (prior or current)	46% (18)
Hypertension	67% (26)
Hyperlipidemia	54% (21)
Diabetes mellitus	18% (7)
<b>Medication Regimen</b>	
ACE Inhibitors or ARB	51% (20)
Beta-Blockers	72% (28)
Aspirin	74% (29)
Statin	69% (27)
Diuretic	46% (18)
<b>Cardiac Structure/Function</b>	
LVEF (%)	49±14%
LV Dysfunction (EF<50%)	49% (19)
LV End-Diastolic Volume	186±57ml
LV End-Systolic Volume	106±56ml
RV EF (%)	51±11%
RV Dysfunction (EF<50%)	31% (12)
RV End-Diastolic Volume	169±62ml
RV End-Systolic Volume	96±52ml

*Data reported as % (n) for categorical variables, mean standard deviation for*

*continuous variables.*

**Table 3.2. QSM in relation to Invasive Catheterization  $\Delta SaO_2$  and Cine-CMR Cardiac Function**

<b>Patient</b>	<b>cath <math>\Delta SaO_2</math> (%)</b>	<b>QSM <math>\Delta SaO_2</math> (%)</b>	<b>LV Ejection Fraction (%)</b>	<b>LV Stroke Volume (ml)</b>	<b>LV Dysfunction (1 = EF&lt;50%)</b>	<b>Pulmonary Hypertension (1=present)</b>
1	25	31	66	96	0	1
2	17	22	70	60	0	0
3	23	24	71	140	0	0
4	10	13	70	90	0	0
5	35	32	47	71	1	1
6	30	29	28	77	1	0
7	40	37	20	48	1	0
8	43	39	20	60	1	1
9	27	35	16	66	1	1
10	28	32	40	48	1	1
11	27	22	66	28	0	1
12	35	30	33	47	1	1
13	23	18	65	94	0	0
14	23	24	54	126	0	0
15	18	17	69	93	0	1

## CHAPTER 4

### QUANTITATIVE SUSCEPTIBILITY MAPPING OF CAROTID PLAQUES USING NONLINEAR TOTAL FIELD INVERSION: INITIAL EXPERIENCE IN PATIENTS WITH SIGNIFICANT CAROTID STENOSIS

#### 4.1 Abstract

**Purpose:** To develop a nonlinear preconditioned total field inversion algorithm using the MEDI toolbox (MEDInpt) for robust quantitative susceptibility mapping (QSM) of carotid plaques and evaluate its performance in comparison with a local field inversion algorithm (STISuite) previously applied to carotid QSM.

**Methods:** Numerical simulation and in vivo carotid QSM were performed to compare the MEDInpt and STISuite algorithms. Multi-contrast MRI (mcMRI) was used as the reference standard for detecting calcified plaque and intraplaque hemorrhage (IPH). A total of five healthy volunteers and eleven patients with at least one significant carotid artery stenosis were enrolled in this study.

**Results:** In the numerical carotid phantom, the relative susceptibility errors for calcified plaque and IPH were reduced from -63.2% and -56.5% with STISuite to -13.0% and -24.2% with MEDInpt, respectively. In humans, MEDInpt provided a higher QSM quality score and better detection of calcification and IPH than STISuite. While all calcifications and IPHs detected on mcMRI could be seen on QSM obtained

with MEDInpt, only 50% of calcified plaques and 83% of IPHs could be captured on QSM obtained with STISuite.

**Conclusion:** MEDInpt can resolve calcification and IPH in advanced atherosclerotic carotid plaques. Compared to STISuite, MEDInpt provided better QSM quality and has the potential to improve the detection of these plaque components.

## 4.2 Introduction

Carotid artery atherosclerosis is a major vascular risk factor and accounts for approximately 15% of ischemic strokes (116,117). Angiography of the carotid artery lumen has been used to quantify the degree of narrowing or stenosis as the main biomarker of stroke risk in patients with carotid atherosclerosis. Additionally, imaging of the vessel wall is much desired to provide a clinically valuable assessment of plaque composition (118). For example, the presence of intraplaque hemorrhage (IPH) on MRI confers a 4 to 6-fold increased risk of future stroke (119,120), which, when taken into account with stenosis and other risk factors, helps to identify high-risk patients who would most likely benefit from surgical revascularization procedures (121-123).

IPH is thought to originate from fragile leaky neovasculature (124) or plaque fissure (125), and occurs in about one-third of asymptomatic patients and a higher proportion of patients with hemodynamically significant stenosis (126). Currently, multi-contrast MRI (mcMRI) is the preferred approach for plaque characterization based on time-of-flight (TOF) and black blood fat-suppressed T1-weighted (T1w), T2-weighted (T2w),

and proton density-weighted (PDw) images (127,128). Fresh and recent IPH can be identified as a vessel wall region with hyperintense signal on TOF and T1w images (127,129,130), while chronic IPH appears hypointense. IPH signal intensity on mcMRI is highly dependent on erythrocyte integrity as well as the state of hemoglobin degradation from deoxyhemoglobin to methemoglobin in the acute stage and later to hemosiderin in the chronic stage (131). While mcMRI can detect large IPHs, it misses about half of small or heavily calcified IPHs (132). Of potentially greater concern, mcMRI cannot differentiate hemosiderin-rich hemorrhage associated with rupture risk from calcification that indicates plaque stability and reduces the risk of arterial embolization by half (133).

Quantitative susceptibility mapping (QSM) is a novel MRI technique that maps magnetic sources in tissue from the tissue field measured with multi-echo gradient echo data by performing field-to-source dipole inversion (134-138). QSM is well suited for distinguishing paramagnetic iron-rich blood products from diamagnetic bone and calcification (90,139,140), as demonstrated previously in the brain (67,141). QSM of the carotid vessel wall for plaque characterization has been attempted using the linear local field inversion approach (142,143). A recent QSM-histology correlation study on patients scheduled for carotid endarterectomy (144) showed that QSM obtained using STISuite software (145) markedly improved the depiction of IPH and calcification in carotid plaques. However, carotid plaque QSM remains a major challenge in the clinic due to residual artifacts caused by the proximity of background air and air cavities in the neck region, which often require significant tissue erosion at the air-tissue interface to ensure effective background field removal (146). Another

challenge is the noise amplification in areas with low signal-to-noise ratio (SNR) including calcified plaques and hemosiderin-rich IPHs, which introduces artifacts on QSM.

The objectives of this study were to develop a nonlinear preconditioned total field inversion (MEDInpt) algorithm using the MEDI toolbox (<http://pre.weill.cornell.edu/mri/pages/qsm.html>) for robust carotid plaque QSM without tissue erosion and to evaluate its ability for distinguishing IPH and calcification in comparison with STISuite using mcMRI as the reference standard.

### 4.3 Methods

#### Nonlinear preconditioned total field inversion (MEDInpt) algorithm

The proposed MEDInpt algorithm combines the robustness of the nonlinear local field inversion algorithm against phase noise propagation in low SNR regions (147) with the improved accuracy of the linear total field inversion (TFI) algorithm near the air-tissue boundaries (148). MEDInpt is comprised of two main steps. First, the total field map (containing both the local and background fields) was obtained by nonlinear fitting of the multi-echo gradient echo data followed by spatial phase unwrapping as described in (147). Next, the susceptibility map was computed using regularized nonlinear total field inversion with preconditioning by minimizing the following objective function:

$$\mathbf{y}^* = \underset{\mathbf{y}}{\operatorname{argmin}} \left\| \mathbf{w}(e^{-i\alpha f} - e^{-id*P\mathbf{y}}) \right\|_2^2 + \lambda \|\mathbf{M}_G \nabla P \mathbf{y}\|_1 \quad [4.1]$$

$$+ \lambda_A \|\mathbf{M}_A P(\mathbf{y} - \bar{\mathbf{y}}^A)\|_2^2$$

Here the first two terms are the data fidelity term and structure consistency regularization term, respectively, where  $w$  is the SNR weighting,  $f$  is the total field,  $d$  is the dipole kernel,  $P$  is the preconditioner,  $M_G$  is the edge mask, and  $\nabla$  is the gradient operator (135). The third term was added to the inversion to enforce susceptibility homogeneity of the well-mixed blood within the lumens of the carotid arteries, similar to the regularization of ventricular CSF in the brain as described in (93).  $M_A$  is the mask of carotid artery lumens obtained by a custom semi-automatic region-growing segmentation algorithm, and  $\overline{y}^A$  is the average susceptibility within the luminal mask (recalculated at each iteration when solving Eq.1 using an iterative method).  $\alpha$  is a scalar value that scales down  $f$  to avoid phase wraps in  $e^{-i\alpha f}$  and  $e^{-id*Py}$ . The preconditioner  $P$  is a binary mask that is 1 inside the region of interest (ROI) and a larger value,  $P_{outside}$ , outside of the ROI. The final QSM map is  $\chi = \frac{1}{\alpha} Py^*$ . In this study, we chose  $P_{outside} = 20$  — similar to previous cardiac QSM work (149) — and  $\alpha = 1/100$  based on the expectation that the maximum total field in the neck region is  $\pm 1$  kHz. The optimal regularization parameters  $\lambda = 1/250$  (which controls the suppression of streaking artifacts on QSM) and  $\lambda_A = 1/10$  (which controls the uniformity of susceptibility values within the arterial lumen) were empirically determined in a healthy subject as follows. First,  $\lambda_A$  was set to 0 and  $\lambda$  was varied from 1/100 to 1/10000, and the optimal  $\lambda$  was determined by visual inspection. Next,  $\lambda_A$  was varied from 1/100 to 1 and an optimal value was similarly obtained. These parameters were then fixed for all subsequent subjects. The objective function in Eq.1 was minimized using the iterative Gauss-Newton algorithm with a conjugate gradient

solver (maximum 500 iterations) at each step. To account for residual field map errors in the input total field, an iterative reweighted least squares fitting method called model error reduction through iterative tuning (MERIT) was implemented to modify the data weighting  $w$  of voxels with poor fit in each Gauss-Newton iteration. In this work, MEDInpt was compared with a linear local field inversion method recently applied to carotid plaques (144) using a publicly available implementation (STISuite version 3.0, <https://people.eecs.berkeley.edu/~chunlei.liu/software.html>). In STISuite, a Laplacian-based algorithm was used to unwrap phase data (150), followed by the V-SHARP algorithm to remove the background field (151), and the iLSQR algorithm for local field-to-source inversion (145). These algorithms were run with default parameters preset by the developers. The same tissue mask was used for processing with MEDInpt and STI Suite. All processing was performed in MATLAB R2018b (Mathworks Inc, Natick, MA, USA) using GPU parallel computing enabled on an Nvidia Titan Xp graphics card (Nvidia Corporation, Santa Clara, CA, USA).

### *Numerical simulation*

To compare the accuracy of MEDInpt and STISuite for carotid QSM, a numerical carotid vessel wall susceptibility phantom (which includes calcified plaque and IPH) was generated based on a realistic vessel structure obtained by manual segmentation of the carotid vessel wall and lumen from MR images of one human subject. Multi-echo GRE image data (ignoring T1 relaxation effect) were calculated using the following signal equation:

$$S_j(\mathbf{r}) = M_0 e^{-t_j R_2^*(\mathbf{r})} e^{it_j d(\mathbf{r}) * \chi(\mathbf{r})} \quad [4.2]$$

where  $S_j(\mathbf{r})$  is the complex GRE signal measured at location  $\mathbf{r}$  and the  $j$ th echo time  $t_j$ ,  $M_0$  is the equilibrium magnetization,  $R_2^*$  is the T2\* relaxation rate,  $d$  is the dipole kernel, and  $\chi$  is the known phantom susceptibility distribution. The following tissue parameters  $M_0$  (a.u.)/ $R_2^*$  (Hz) / $\chi$  (ppm) were assumed based on literature values: muscle = 0.9/40/0, vessel wall = 0.9/45/-0.1, arterial blood = 0.85/20/0.1, venous blood = 0.85/40/0.4, calcification = 0.13/500/-1.5, IPH = 0.5/150/1.5. Background air has susceptibility of 9 ppm. The simulation parameters were: 1<sup>st</sup> TE/ $\Delta$ TE/ETL = 2.9 ms/4.7 ms/4 (same as that of in vivo imaging study), SNR = 100. Complex GRE images were generated at 0.3 mm isotropic resolution and then downsampled to 0.6 x 0.6 x 2 mm<sup>3</sup> resolution (which was used for in vivo imaging), from which QSM images were reconstructed using MEDInpt and STISuite as described above.

#### *In vivo carotid QSM study*

The human imaging study was approved by our local Institutional Review Board. Carotid QSM was first optimized and tested in five healthy volunteers (all male, mean age 31.6 years  $\pm$  8.8). The developed carotid QSM protocol was further evaluated in patients with atherosclerotic disease of the carotid arteries who were undergoing imaging for clinical purposes. Imaging was performed on 3T Siemens scanners using a product 64-channel head/neck coil or a 6-channel dedicated carotid surface coil for signal reception. A total of eleven patients (all male, mean age 63.2 years  $\pm$  4.8) with

at least one hemodynamically significant carotid artery stenosis (>50% stenosis) were included in this pilot study.

The carotid plaque MRI protocol was based on recent recommendations by the ASNR Vessel Wall Imaging Study Group (152) and consisted of 3D gradient echo TOF, 2D black-blood fat-suppressed T1w and T2w turbo spin echo (TSE), and 3D magnetization-prepared rapid gradient echo (MPRAGE) sequences for mcMRI as well as 3D multi-echo gradient echo sequence for QSM with approximately 6 cm longitudinal coverage of the carotid bifurcation. The pertinent imaging parameters were as follows: axial T1w TSE: TR/TE = 885/9.4 ms, echo train length (ETL) = 7, number of signal averaging (NSA) = 2, readout bandwidth (rBW) = 410 Hz/pixel, voxel size = 0.63x0.63x2 mm<sup>3</sup>, scan time = 4:12 min; axial T2w TSE: TR/TE = 4770/58 ms, ETL = 12, NSA = 3, rBW = 410 Hz/pixel, voxel size = 0.63x0.63x2 mm<sup>3</sup>, scan time = 6:21 min; coronal MPRAGE: TR/TE/TI = 840/3.4/500 ms, flip angle = 15°, rBW = 331 Hz/pixel, voxel size = 0.63x0.63x0.83 mm<sup>3</sup>, scan time = 3:44 min; axial TOF: TR/TE = 20/3.6 ms, flip angle = 30°, rBW = 250 Hz/pixel, voxel size = 0.63x0.63x2 mm<sup>3</sup>, scan time = 4:03 min; axial QSM: TR/first TE/TE spacing = 21/2.9/4.7 ms, ETL = 4, flip angle = 10°, NSA = 2, rBW = 580 Hz/pixel, voxel size = 0.63x0.63x2 mm<sup>3</sup>, scan time = 8:03 min. For T1w and T2w TSE, blood suppression was achieved by spatial presaturation of the region immediately upstream to the imaged slice. For QSM, echo time spacing of 4.7 ms was chosen to allow 4 $\pi$  inter-echo phase evolution of fat relative to water at 3T, which has been shown to provide optimal field estimation in the presence of fat (153).

### Image analysis

A neuroradiologist with 13 years of reading experience reviewed the mcMRI images to identify calcification and IPH in carotid plaques. Calcification was defined as a vessel wall region with hypointense signal (compared to the adjacent muscle) on mcMRI images. IPH was defined as a wall region with hyperintense signal on T1w and MPRAGE images (the TOF image was used when the MPRAGE image was not interpretable due to motion or blood flow artifacts) and hypo- or iso-intense region on T2w images. Prior CTA images (if available) were also reviewed as part of an IRB-approved retrospective study to corroborate the presence of calcified plaques. The MEDInpt and STISuite QSM image of the plaque detected by mcMRI was then reviewed to identify calcification and IPH as regions with strongly negative and positive susceptibilities, respectively, compared to that of the adjacent arterial blood. The diagnostic quality of QSM maps obtained with MEDInpt and STISuite was subjectively scored on a 3-point scale (1=poor, 2=good, 3=excellent). QSM values are reported using arterial blood as the susceptibility reference.

### **4.4 Results**

Numerical simulation results showed that the mean susceptibility values of both calcified plaque and IPH obtained with the proposed MEDInpt algorithm were more accurate than those obtained with STISuite, reducing the relative error in calcified plaque and IPH from -63.2% and -56.5% with STISuite to -13.0% and -24.2% with MEDInpt, respectively. While both algorithms were able to correctly detect the

presence of calcification and IPH, MEDInpt provided a more truthful depiction of plaque morphology (Fig.4.1).

Carotid wall QSM was obtained successfully from all five healthy volunteers using MEDInpt and STISuite. Figure 4.2 shows an example of QSM images of the common carotid artery, demonstrating improved depiction of the artery wall and soft tissues without tissue erosion by MEDInpt in the neck region compared to STISuite. The average quality scores of QSM obtained with MEDInpt and STISuite were  $2.8 \pm 0.4$  and  $1.8 \pm 0.4$ , with higher scores for MEDInpt in all five healthy cases.

Carotid plaque QSM using MEDInpt and STISuite was successful in 82% (9/11) of patients. Two patients had non-diagnostic QSM due to excessive ghosting and blurring artifacts caused by breathing motion as evidenced by the source GRE magnitude images; their data were excluded from further analysis. The average QSM quality scores of the remaining nine patients were  $2.6 \pm 0.5$  and  $1.8 \pm 0.4$  for MEDInpt and STISuite, respectively. A total of six plaques with calcifications and six with IPH were identified on mcMRI, all of which (100%) could be seen on QSM obtained with MEDInpt. However, only 3/6 (50%) of calcified plaques and 5/6 (83%) of IPHs could be captured on QSM obtained with STISuite. Figure 4.3 shows an example of a large plaque with extensive calcification almost fully occluding the left internal carotid artery in a 59-year-old patient. The calcified plaque can be defined as regions with hypointense appearance on mcMRI and strongly negative susceptibility on QSM with similar depiction by MEDInpt and STISuite. In this and all subsequent figures, display windows of  $\pm 1.5$  ppm and  $\pm 0.75$  ppm were used for QSM images obtained with

MEDI<sub>np</sub>t and STISuite, respectively, to provide similar visual contrast. Figure 4.4 shows an example of a plaque in the right internal carotid artery of a 69-year-old patient, which appears hyperintense on TOF, T1w and MPRAGE images and hypointense on a T2w image suggesting the presence of a recent IPH (131). On QSM, this area also has a hyperintense appearance with a positive susceptibility value of 0.7 ppm by MEDI<sub>np</sub>t and 0.2 ppm by STISuite. In this example, QSM also identified an adjacent calcified plaque with a negative susceptibility value of approximately -1 ppm, which could not be prospectively identified by the human readers using only mcMRI images because of its small size. Figure 4.5 illustrates the superior QSM quality of MEDI<sub>np</sub>t compared to that of STISuite for depicting calcified plaques in a 71-year-old patient in excellent agreement with mcMRI.

In addition to the six IPHs identified by both QSM and mcMRI, QSM obtained with the proposed MEDI<sub>np</sub>t algorithm further detected small focal hyperintense areas with high positive susceptibility in four other plaques, which were invisible or appeared hypointense on mcMRI similar to calcification and could not be prospectively detected on QSM obtained with STISuite. Figure 4.6 illustrates an example in which two regions at the boundary of a large plaque from a 63-year-old patient appear similarly hypointense on TOF, T1w, T2w and MPRAGE images. On QSM obtained with MEDI<sub>np</sub>t, one region has a strongly negative susceptibility of -1.5 ppm consistent with calcification. However, the other region shows a strongly positive susceptibility of 1.8 ppm suggesting an old hemorrhage with deposition of highly paramagnetic hemosiderin. These plaque features with marked susceptibility contrast could not be seen well on QSM obtained with STISuite.

## 4.5 Discussion

In this pilot study, we have demonstrated the feasibility of carotid QSM using the proposed MEDInpt algorithm and its potential to distinguish calcification and IPH in carotid plaques of patients with hemodynamically significant carotid stenosis.

Calcified plaques appear hypointense on QSM with strongly negative susceptibility of less than -1 ppm, while IPH has positive susceptibility ranging from approximately 0.5 ppm in a recent hemorrhage to 1.5-2 ppm in a chronic hemorrhage. The promising results obtained in this preliminary study suggest that QSM can play an important role in carotid plaque assessment, especially for distinguishing calcification and IPH, as well as for detecting small focal IPH. Compared to traditional mcMRI, the unambiguous visual contrast between calcification/IPH and the surrounding tissues on QSM allows easy identification and may improve diagnostic confidence.

The benefit of QSM for improving the depiction of calcifications and IPHs in carotid atherosclerotic plaques has been demonstrated recently by Ikebe et al (144) who applied the STISuite linear local field inversion method to carotid QSM. In this study, we showed that, compared to STISuite, MEDInpt provides higher QSM quality scores as well as better depiction of calcification and IPH, leading to improved detection rates. Several factors may contribute to the performance of STISuite in this study: 1) the Laplacian based phase unwrapping may introduce smoothing of the field measurements near large susceptibility sources (154), and 2) background field removal, which is necessary for local field inversion methods, can be challenging in the neck area due to the presence of air cavities and bones within the region of interest

(146). Unlike STISuite, MEDInpt performs total field-to-source inversion through nonlinear fitting of the complex field data, which is more robust against noise propagation (147) and achieves effective background field removal over the small neck region without requiring tissue erosion.

A major pathological feature of vulnerable plaques at high risk of rupture is the presence of IPHs (119,120,123). Currently, IPH is identified as T1w hyperintensity on a plaque region (128). However, it is well known that T1w hyperintensity only captures the transient methemoglobin phase of hemorrhage after red blood cell lysis (155). The hemosiderin phase immediately follows the methemoglobin phase due to macrophages collecting heme iron released during hemorrhage formation.

Hemosiderin has considerably higher positive magnetic susceptibility than methemoglobin, resulting in hypointensity on T1w due to rapid signal decay caused by diffusion (spin echo) and dephasing (gradient echo) in strong inhomogeneous fields (131). This T1w hypointensity has been interpreted as calcification, another common component of carotid plaque with very negative susceptibility, potentially causing IPH misdetection. The inability of mcMRI to reliably detect IPH is even more pronounced at higher magnetic field strengths (3T vs. 1.5T) due to increased susceptibility induced field effects (156). This is considered as the primary cause of the much lower IPH detection sensitivity (53-71%) of mcMRI at 3T compared to 1.5T (132,157,158).

Unlike mcMRI, QSM allows for direct characterization of tissue magnetism and can resolve IPH hemosiderin with positive (strongly paramagnetic) susceptibility from calcification with negative (strongly diamagnetic) susceptibility. This is demonstrated in Fig. 4.6 where QSM detects small regions that appear hypointense on mcMRI but

have high susceptibility values of opposite signs consistent with calcification and hemorrhage sources. In this study, out of the ten detected plaques with IPH, six of relatively large size were identified by both mcMRI and MEDInpt QSM, and four of small size by MEDInpt QSM alone. This suggests that adding MEDInpt QSM to carotid MRI may improve the IPH detection rate. Furthermore, combining QSM with T1w may enable the characterization of hemorrhage age (Fig. 4.6) (139), which is potentially valuable for assessing plaque rupture risk. The encouraging results obtained in this pilot study warrant a larger study to evaluate the benefit of QSM for detecting IPHs.

While carotid QSM was successfully obtained from all healthy volunteers, excessive motion artifacts led to unreliable QSM in 18% of patients, which is similar to the 15% failure rate attributed to motion in a previous multicenter carotid MRI study (159).

Motion is a well-known challenge for high resolution MRI (160). Carotid artery motion includes both the patient's involuntary head or swallowing motion and physiological motion related to respiration and cardiac pulsatility. Swallowing has been identified as the greatest source of artery displacement (4.7 mm on average) (161). Real-time navigator gating approaches have been developed to suppress intra-scan swallowing and breathing motion (51,162,163) and will be considered in our future work to further improve the reliability of carotid plaque QSM.

A major limitation of this feasibility study is the lack of histopathological confirmation of calcification and IPH detected in the carotid plaques. Another limitation is the relatively long scan time of the QSM sequence. More efficient k-

space sampling trajectories (164) and the use of higher field strengths or better surface carotid coil designs to improve SNR can be used to reduce acquisition time. Also, in comparison with QSM approaches for dealing with a large dynamic range of susceptibilities, including the STAR-QSM method (165), was not performed. Finally, other plaque components of clinical interest including the lipid-rich necrotic core and the fibrous cap were not considered in this study due to the limited sample size.

#### **4.6 Conclusion**

In conclusion, our study demonstrated that QSM using the proposed MEDInpt algorithm can distinguish calcification and IPH in advanced atherosclerotic carotid plaques in good agreement with findings on mcMRI. Compared to STISuite, MEDInpt provided better QSM quality and has the potential to improve the detection of calcifications as well as small focal areas with high positive susceptibility values consistent with hemorrhages.

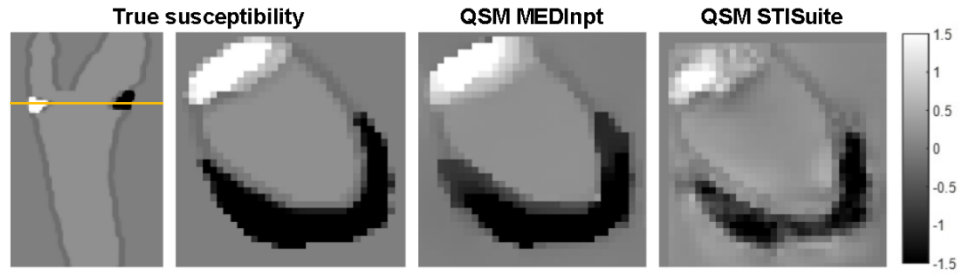


**Figure 4.1.** Simulated susceptibility distribution (in ppm) of the carotid artery with a calcified plaque (strongly negative compared to the surrounding arterial blood and muscle tissues) and an IPH (strongly positive) near the carotid bifurcation. Both coronal and enlarged axial views (at the level indicated by the orange line) are shown on the left. QSM images reconstructed from the numerically simulated complex multi-echo GRE data (SNR = 100) by the proposed MEDInpt and STISuite algorithms show good tissue contrast for both plaque components. However, MEDInpt provides more accurate susceptibility values than STISuite.

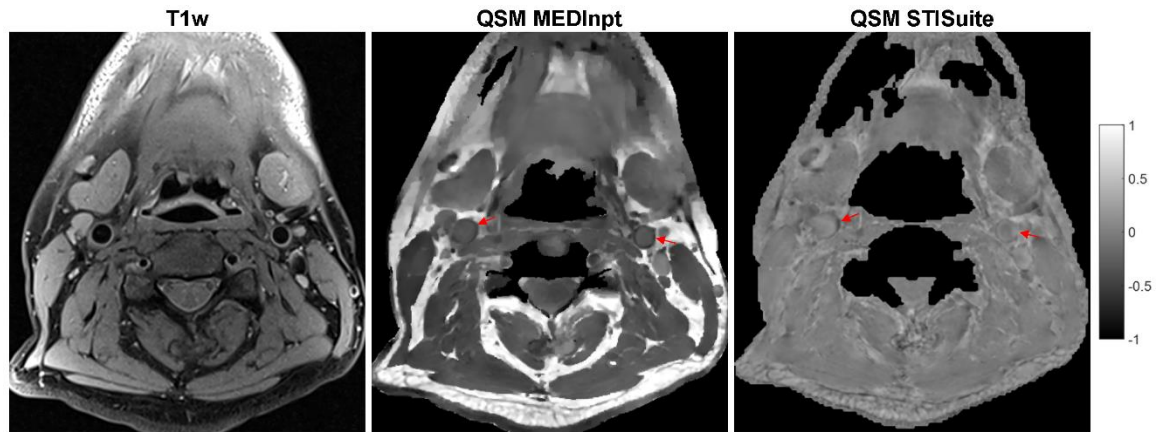


**Figure 4.2.** Example of black blood T1w and QSM images (in ppm) of the common carotid arteries obtained from a healthy volunteer using MEDInpt and STISuite reconstruction algorithms. Compared to STISuite, MEDInpt provides better overall QSM quality of the cervical vasculature and soft tissues. Note the improved depiction of the arterial vessel walls by MEDInpt (red arrows) with a diamagnetic susceptibility of approximately -160 ppb compared to -60 ppb by STISuite using arterial blood as the susceptibility reference.

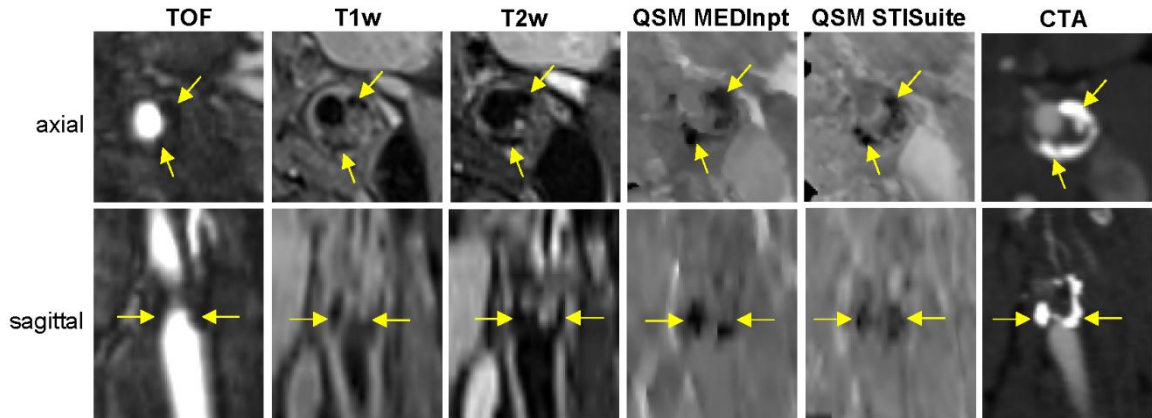


**Figure 4.3.** Example of a heavily calcified plaque almost fully occluding the left internal carotid artery at the level of carotid bifurcation with hypointense appearance on TOF and black-blood T1w and T2w images as well as strongly negative susceptibility on QSM images computed with MEDInpt and STISuite (approximately  $<-1.2$  ppm compared to arterial blood). Note the improved calcification contrast on QSM compared to mcMRI images. In this and all subsequent figures, display windows of  $\pm 1.5$  ppm and  $\pm 0.75$  ppm were used for QSM images obtained with MEDInpt and STISuite, respectively, to provide similar visual contrast. The computed tomography angiography (CTA) image acquired 1.5 years prior to MRI at 0.6 mm resolution from the same patient is shown to help with plaque localization.

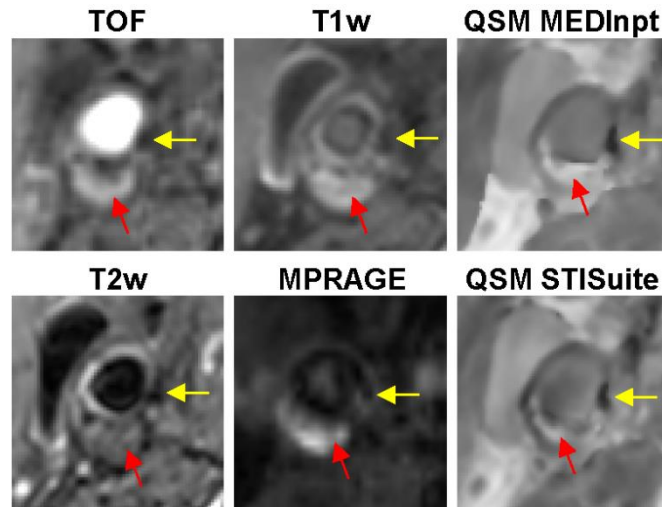


**Figure 4.4.** Example of a carotid plaque in the right internal carotid artery (red arrow) with hyperintense appearance on TOF, T1w and MPRAGE images and slightly hypointense signal on the T2w image, which are consistent with a recent IPH. On QSM, the IPH shows relatively high positive susceptibility (approximately 0.7 ppm and 0.2 ppm higher than the arterial blood by MEDInpt and STISuite, respectively). Both MEDInpt and STISuite show a small calcified plaque on the wall of the adjacent carotid artery with strongly negative susceptibility on QSM (yellow arrow), demonstrating the superior contrast of QSM for calcification detection compared to mcMRI.

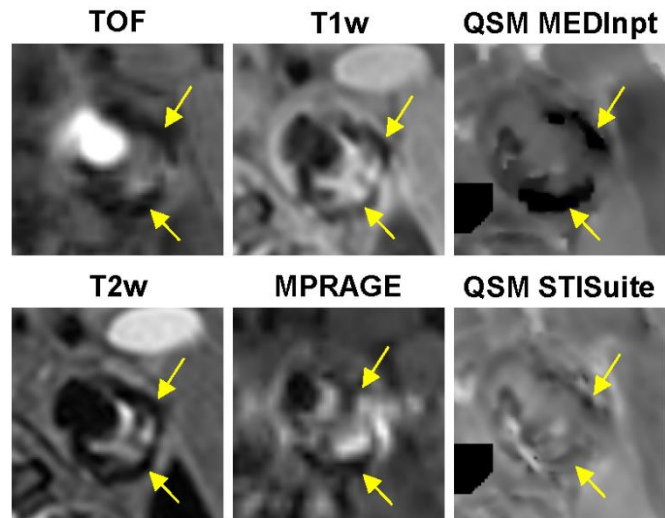


**Figure 4.5.** Example of calcified plaques in the left carotid artery at the level of carotid bifurcation with hypointensity on mcMRI and strongly negative susceptibility (approximately -2 ppm compared to the arterial blood) on QSM obtained with the MEDInpt algorithm. In this case, STISuite did not provide a clear depiction of the calcifications.

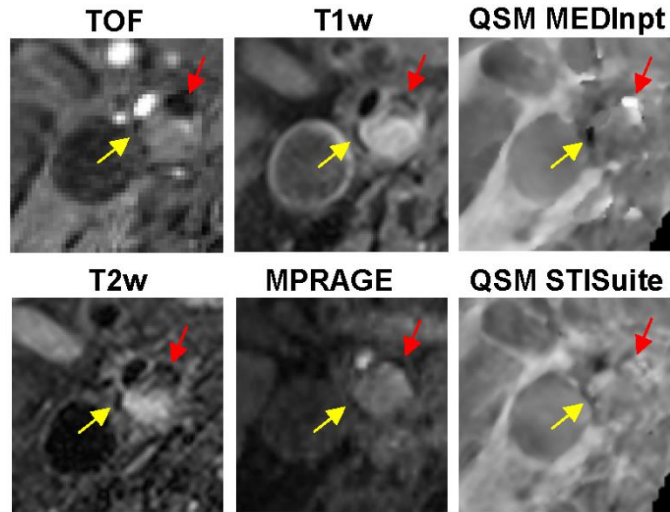


**Figure 4.6.** In this example of a severely stenotic right internal carotid artery, small hypointense regions (arrows) can be identified at the edge of a large plaque on TOF, T1w, T2w and MPRAGE images suggesting the presence of calcifications. On QSM obtained by the proposed MEDInpt algorithm, one region (yellow arrow) shows strongly negative susceptibility (approximately -1.5 ppm) consistent with calcification. However, the other region shows strongly positive susceptibility (approximately 1.8 ppm) with hypointensity on mcMRI, suggesting paramagnetic iron contained within hemosiderin from old hemorrhage. These plaque features could not be identified on the corresponding QSM obtained with STISuite.

## CHAPTER 5

# MULTI-ECHO COMPLEX TOTAL FIELD INVERSION (mcTFI) METHOD FOR IMPROVED SIGNAL MODEL IN QUANTITATIVE SUSCEPTIBILITY MAPPING

### 5.1 Abstract

**Purpose:** To develop a multi-echo complex Total Field Inversion (mcTFI) method to compute the susceptibility map directly from the multi-echo gradient echo images using an improved signal model that retains the Gaussian noise property in the complex domain, and demonstrate its improvements in QSM reconstruction over the traditional field-to-source inversion.

**Methods:** The proposed mcTFI method was compared with the Total Field Inversion method (TFI) in a numerical brain with hemorrhage and calcification, the numerical brains used in the QSM challenge 2.0, 18 brains with intracerebral hemorrhage scanned at 3T, and 6 healthy brains scanned at 7T.

**Results:** Compared to TFI, the proposed mcTFI demonstrated more accurate QSM reconstruction around the lesions in both numerical simulations. The mcTFI reconstructed QSM also demonstrated the best image quality with the least artifacts in the brains with intracerebral hemorrhage scanned at 3T and healthy brains scanned at 7T.

**Conclusion:** The proposed multi-echo Complex Total Field Inversion improved QSM

reconstruction over traditional field-to-source inversion through better signal modeling.

## **5.2 Introduction**

Quantitative Susceptibility Mapping (QSM) is an MRI contrast mechanism that is capable of the mapping of the underlying tissue magnetic susceptibility (1). The magnetic susceptibility sources are magnetized when placed inside an external magnetic field such as the main field  $B_0$  of an MRI scanner, and the magnetic fields generated by the magnetized susceptibility sources, henceforth termed the susceptibility field, can then be measured by the MRI scanner for susceptibility map reconstruction. Accordingly, QSM can be used to study tissue susceptibility sources such as deoxyheme iron in blood (2-8), tissue nonheme iron (9-12), myelin (13), cartilage (14,15), and calcification (16-18). QSM robustness and reproducibility have been demonstrated for brain applications (19,20), and there are a wide range of QSM clinical applications, including deep brain stimulation target mapping (21,22), cerebral cavernous malformation monitoring (23-25), multiple sclerosis chronic inflammation imaging (26-28) and MRI follow-up without gadolinium (27,29), neurodegeneration investigation in Parkinson's disease (30-33) and Alzheimer's disease (31,34,35), and more (36,37).

Technical challenges remain for QSM in regions of low SNR, such as lesions with large susceptibility contrasts and regions near air-tissue interfaces (38), and these challenges become more problematic at higher field strengths. Typically, the multi-echo gradient-echo (GRE) sequence is used for QSM data acquisition and the

susceptibility field can be inferred as the change in the phase of the GRE images measured at the multiple echo times. QSM reconstruction consists of first estimating this susceptibility field from the GRE images, and then reconstructing the susceptibility map from the estimated field (39). While proper noise modeling of the estimated field is important (40,41), assumptions made during field estimation from GRE data may introduce errors (39,42). These errors can propagate into the reconstructed susceptibility map as artifacts. The use of iterative tuning of the noise weighting (MERIT) (41) helps alleviate some of the resulting artifacts but its implementation remains empirical.

Here we report a multi-echo Complex Total Field Inversion (mcTFI) method to compute the susceptibility map directly from the acquired GRE images using an improved signal model and the Gaussian noise property of the complex data. We compared mcTFI with preconditioned Total Field Inversion (TFI) (43,44), to demonstrate improvements in susceptibility reconstruction, especially in regions with low SNR.

### 5.3 Theory

In this work, the gradient echo signal  $S_j$  measured at echo time  $t_j$  with  $j = 1, \dots, \#TE$  is modeled as:

$$S_j = m_0 e^{-t_j R_2^*} e^{i\phi_0} e^{it_j 2\pi f} \quad [5.1]$$

Where  $m_0$  is the initial magnetization,  $R_2^*$  is the  $T_2$  relaxation rate,  $\phi_0$  is the initial phase offset, and  $f$  is the susceptibility field. The susceptibility field is modeled as a

dipole field: it is the convolution of a susceptibility distribution  $\chi$  with the magnetic field of a unit dipole. An operator  $D$  is used to denote the convolution with the unit dipole field:

$$f = \gamma B_0 D \chi \quad [5.2]$$

Where  $\omega_0 = \gamma B_0$  with  $B_0$  the main magnetic field with  $\gamma$  being the gyromagnetic ratios. Therefore, Eq. 5.2 can also be written as the susceptibility modeled complex signal at the  $j^{\text{th}}$  echo:

$$S_j = m_0 e^{-t_j R_2^*} e^{i\phi_0} e^{it_j \omega_0} D \chi \quad [5.3]$$

The goal of QSM is to reconstruct the susceptibility distribution map,  $\chi$ , from the measured complex GRE images,  $S_j$ .

Here, we propose mcTFI to compute the susceptibility distribution directly from the complex gradient echo data. The cost function of mcTFI was formulated as follows:

$$\begin{aligned} \chi' = P\mathbf{y}', \quad & (\mathbf{m}'_0, \mathbf{R}'_2, \phi'_0 \mathbf{R}\mathbf{y}') \quad [5.4] \\ & = \underset{m_0, R_2^*, \phi_0, \mathbf{y}}{\operatorname{argmin}} \sum_{j=1}^{\#TE} \left\| m_0 e^{-t_j R_2^*} e^{i\phi_0} e^{it_j D P \mathbf{y}} - S_j \right\|_2^2 \\ & + \lambda_1 \|M_G \nabla P \mathbf{y}\|_1 + \lambda_2 \|M_c (P \mathbf{y} - \overline{P \mathbf{y}}^{M_c})\|_2^2 + \lambda_3 \left\| \begin{array}{l} d\mathbf{m}_0 \\ d\mathbf{R}_2^* \\ d\phi_0 \end{array} \right\|_2^2 \end{aligned}$$

Where  $m_0$ ,  $R_2^*$ , and  $\phi_0$ , were solved alongside with the susceptibility map,  $\chi = P\mathbf{y}$ , with  $P$  being a preconditioner. The second term is a weighted total variation designed to suppress streaking artifacts in  $\mathbf{y}$ , where  $\lambda_1$  is the regularization parameter,  $M_G$  is the binary edge mask reflecting the anatomy, and  $\nabla$  is the gradient operator. The third term enforces uniform susceptibility distribution in  $P\mathbf{y}$  within a mask  $M_c$  where  $\lambda_2$  is

the regularization parameter, and  $\overline{Py}^{M_c}$  is the average of  $Py$  over  $M_c$ . In brain QSM,  $M_c$  is typically chosen as the regions containing CSF (45). The last term is a Tikhonov regularization on the updates of  $m_0$ ,  $R_2^*$ , and  $\phi_0$  to improve stability, where  $\lambda_3$  is the regularization parameter.

The optimization problem in Eq. 5.4 was solved iteratively using the Gauss-Newton (GN) method. In each GN iteration, Eq. 5.4 was linearized with respect to the four unknowns via first order Taylor expansion. For computational efficiency, the linearized problem at the  $n$ th GN iteration was broken down into two subproblems: 1) keeping  $m_{0,n}$ ,  $R_{2,n}^*$ , and  $\phi_{0,n}$  fixed,  $y_{n+1}$  was found using the Conjugate Gradient (CG) solver (see Appendix A for solver detail):

$$\mathbf{y}'_{n+1} = \underset{\mathbf{y}}{\operatorname{argmin}} \sum_{j=1}^{\#TE} \left\| \mathbf{m}_{0,n} e^{-t_j R_{2,n}^*} e^{i\phi_{0,n}} e^{it_j D P \mathbf{y}} - \mathbf{S}_j \right\|_2^2 + \lambda_1 \|\mathbf{M}_G \nabla P \mathbf{y}\|_1 + \lambda_2 \|\mathbf{M}_c (P \mathbf{y} - \overline{P \mathbf{y}}^{M_c})\|_2^2 \quad [5.5]$$

and 2) keeping  $y_{n+1}$  fixed,  $m_{0,n+1}$ ,  $R_{2,n+1}^*$ , and  $\phi_{0,n+1}$  were updated using a voxel-by-voxel pseudo-inversion (see Appendix B for solver detail):

$$\begin{aligned} & (\mathbf{m}'_{0,n+1}, \mathbf{R}'_{2,n+1}, \boldsymbol{\phi}'_{0,n+1}) \\ &= \underset{m_0, R_2^*, \phi_0}{\operatorname{argmin}} \sum_{j=1}^{\#TE} \left\| \mathbf{m}_0 e^{-t_j R_2^*} e^{i\phi_0} e^{it_j P D \mathbf{y}_{n+1}} - \mathbf{S}_j \right\|_2^2 \\ &+ \lambda_3 \left\| \begin{array}{c} d\mathbf{m}_0 \\ dR_2^* \\ d\phi_0 \end{array} \right\|_2^2 \end{aligned} \quad [5.6]$$

The proposed mcTFI method can be considered as an extension to the TFI method (44). In TFI, QSM was computed by fitting the susceptibility to the susceptibility

field,  $f$ , which needs to be first estimated via a separation fitting, for instance, by approximating the noise in the signal amplitude in Eq. 5.1 and solving only for  $\phi_0$  and  $f$ :

$$(\phi'_0, f') = \underset{\phi_0, f}{\operatorname{argmin}} \sum_{j=1}^{\#TE} \left\| |S_j| e^{i\phi_0} e^{it_j 2\pi f} - S_j \right\|_2^2 \quad [5.7]$$

the susceptibility map was then reconstructed by solving the following optimization problem using the Gauss-Newton method:

$$\begin{aligned} \chi' = \mathbf{P}\mathbf{y}', \quad \mathbf{y}' = \underset{\mathbf{y}}{\operatorname{argmin}} & \left\| \mathbf{w}(\mathbf{D}\mathbf{P}\mathbf{y} - \mathbf{f}) \right\|_2^2 + \lambda_1 \left\| \mathbf{M}_G \nabla \mathbf{P}\mathbf{y} \right\|_1 \\ & + \lambda_2 \left\| \mathbf{M}_c(\mathbf{P}\mathbf{y} - \overline{\mathbf{P}\mathbf{y}}^{M_c}) \right\|_2^2 \end{aligned} \quad [5.8]$$

where  $w$  is a diagonal noise weighting matrix, which was typically calculated as the covariance matrix of the fitting in Eq. 5.7 (46). Note that the noise in  $f$  may no longer be Gaussian, which could introduce model errors to the data fidelity term in Eq. 5.8. Using a proper noise weighting in TFI can help to mitigate this model error (as well as fitting errors from Eq. 5.7) by assigning small values to  $w$  in the problematic voxels, therefore, reducing the influence of these problematic voxels during the optimization. Since  $w$  can also contain errors and may not completely account for the noise property in the susceptibility field, MERIT (41) was introduced to further retune  $w$ . With MERIT, at the end of the  $i$ th GN iteration, the noise weighting  $w_i$  is updated to  $w_{i+1}$ , which will be used in the next GN iteration, as follows:

$$\mathbf{w}_{i+1} = \begin{cases} \mathbf{w}_i & \frac{\rho_i}{T} \leq 1 \\ \frac{\mathbf{w}_i}{\left(\frac{\rho_i}{T}\right)^R} & \frac{\rho_i}{T} > 1 \end{cases} \quad [5.9]$$

where  $\rho_i = w_i |DPy_i - f|$  is the voxel-by-voxel data term residual for the  $i_{th}$  iteration,  $T$  is the threshold determining the number of voxels whose noise weighting will be reduced, and  $R$  is the attenuation factor determining the strength of the weighting reduction. Careful selection of  $T$  and  $R$  are important: large values may cause reasonable voxels to be disregarded and small values may not probably penalize all erroneous voxels. However, MERIT is a heuristic method and the parameters,  $T$  and  $R$ , are currently empirically determined.

The proposed mcTFI method is hypothesized to be an improvement upon the TFI method because 1) mcTFI does not require the fine-tuning of  $w$ , and 2) by avoiding a separate fitting of  $f$ , the Gaussian noise assumption in mcTFI cost function still holds.

## 5.4 Methods

The accuracy of the proposed mcTFI algorithm was evaluated against TFI both without and with MERIT (TFI+MERIT) in a numerical brain simulation with inclusion of a hemorrhage and calcification, in patients suffering from intracerebral hemorrhage (ICH) scanned at 3T and in healthy subjects scanned at 7T.

### Implementation Details

In TFI,  $P$  is the automated adaptive preconditioner,  $\lambda_1 = 0.001$ , and  $\lambda_2 = 0.1$  were chosen as accordance with the literature (43). The MERIT parameters  $T = 6\sigma$ , where

$\sigma$  is the standard deviation of the two-norm of the data term residual, and  $R = 2$  were chosen according to the original work (41).

The same automated adaptive preconditioner was used in mcTFI. The follows steps were taken in order to match the regularizations parameters in mcTFI to that in TFI:

- 1) The noise weighting in TFI was scaled such that its mean values over the brain mask  $M$  was 1, or  $\frac{1}{\#M} \sum_{k \in M} w_k = 1$  with  $\#M$  the number of voxels in  $M$ . In mcTFI, the complex images,  $S_j$  were scaled by  $C = \frac{1}{\#TE} \sum_{j=1}^{\#TE} \frac{1}{\#M} \sum_{k \in M} |S_{j,k}|$ , so that  $\frac{1}{\#TE} \sum_{j=1}^{\#TE} \frac{1}{\#M} \sum_{k \in M} \left| \frac{S_{j,k}}{C} \right| = 1$ .
- 2)  $\lambda_{1,mcTFI} = \lambda_{1,TFI} \times \sum_{j=1}^{\#TE} t_j$  and  $\lambda_{2,mcTFI} = \lambda_{2,TFI} \times \sum_{j=1}^{\#TE} t_j^2$  were chosen as the regularization parameters (see appendix A for derivation).

The Tikhonov regularization parameter,  $\lambda_3$ , was automatically determined for each case by first constructing a L-curve in a large range, from  $10^{-5}$  to  $10^1$  with an increment of an order of magnitude, to determine a rough value for the L-curve corner. Then, a second L-curve was constructed within a range of an order of magnitude around this rough value, and  $\lambda_3$  was chosen as the corner of the second L-curve. The L-curve corner was determined using an adaptive pruning algorithm (47). To further improve the stability of mcTFI,  $m_0$  and  $R_2^*$  were constrained to be greater than or equal to zero.

Proper initializations are important for solving the nonlinear optimization problems in mcTFI. Here,  $R_{2,init}^*$  was obtained using ARLO (48), and then  $m_{0,init}$  was estimated

as  $m_{0,init} = \frac{|S_1|}{e^{-t_1 R_{2,init}^*}}$ .  $\phi_{0,init}$  and  $f_{init}$  were obtained via pseudo-inversion of the

$$\text{phase in the first two GRE echoes: } (\phi_{0,init}, f_{init}) = \begin{bmatrix} 1 & t_1 \\ 1 & t_2 \end{bmatrix}^{-1} \begin{bmatrix} \angle S_1 \\ \angle S_2 \end{bmatrix}.$$

One challenge in initializing Eq. 5.5 is that the angle of a complex exponential is only defined within a range of  $2\pi$ , so that large susceptibility field may cause wraps in the phase, leading in turn to a wraps in the resulting susceptibility map. Such wrapping artifact can be avoided if  $y$  is initialized without any wraps, and this was done with the following steps:

- 1) Perform phase unwrapping on  $f_{init}$
- 2) Perform phase unwrapping on the phase of the GRE images:  $\angle S_{j,nowrap} = \angle S_j - \text{round}\left(\frac{\angle S_j - f_{init} * t_j + \phi_{0,init}}{2\pi}\right) * 2\pi$
- 3) Construct a new set of GRE images that do not have phase wrap:  $S_{j,nowrap} = |S_j| e^{i\alpha \angle S_{j,nowrap}}$ . Here,  $\alpha$  is a very large scalar that ensures the range of  $\alpha \angle S_{j,nowrap}$  falls within  $2\pi$  so that there is no phase wrap.
- 4) Solve  $y_{nowrap} = \underset{y}{\text{argmin}} \sum_{j=1}^{\#TE} \|m_{0,init} e^{-t_j R_{2,init}^*} e^{i\phi_{0,init}} e^{it_j D P y} - S_{j,nowrap}\|_2^2 + \lambda_1 \|M_G \nabla P y\|_1 + \lambda_2 \|M_c (P y - \overline{P y}^{M_c})\|_2^2$ , linearized at  $y = 0$  and with 1 GN iteration.
- 5)  $y_{init} = y_{nowrap} / \alpha$

A quality map guided spatial unwrapping algorithm was used for phase unwrapping (49).

## Simulation

A numerical brain phantom with calcification and hemorrhage was constructed based on the Zubal phantom (50). First, multi-echo GRE image data (ignoring T1 relaxation effect) were simulated according to Eq. 5.3, on 3T, with simulation parameters  $1^{\text{st}}$  TE (ms)/ $\Delta$ TE (ms)/#TE (ms)/voxel size (mm<sup>3</sup>)=4.5/5/8/1x1x1, and with known tissue parameters  $m_0$  (a.u.)/ $R_2^*$  (Hz)/ $\phi_0$  (rad)/ $\chi$  (ppm) set for different structures based on literature values: white matter = 0.715/20/1/-0.046, grey matter = 0.715/20/1/0.053, CSF = 0.715/4/1/0, caudate nucleus= 0.715/30/1/0.093, putamen = 0.715/30/1/0.093, thalamus = 0.9/20/1/0.073, globus pallidus = 0.9/45/1/0.193, calcification = 0.1/500/1/-2.4, ICH = 0.1/150/1/2.68, air = 0/0/0/9, sagittal sinus = 0/45/0/0.27, and skull = 0/4/0/-2. Next, random zero-mean gaussian white noise at SNR = 100 was added to the real and imaginary parts of the complex image independently. Finally, the GRE images were downsampled by a factor of 2, from which the QSM images were reconstructed using the different methods for comparison. This simulation experiment was repeated for SNR ranging from 10 to 150 to evaluate the performance of the QSM methods at different SNR levels, and at each SNR level the experiment was repeated 10 times. The accuracy of the reconstructed QSM was calculated as the mean of the RMSE=  $\sqrt{\frac{1}{N} \sum_i^N (M\chi_{truth,i} - M\chi_{recon,i})^2}$  over the 10 repeats; RMSE was calculated inside of the brain mask, only inside of the lesions, and only outside of the lesions. The lesion mask was set as the actual lesion plus 3 layers of voxels around it.

### QSM Challenge 2.0 data

The 4 datasets (1 brain with and without calcification, simulated at two different SNR) provided in the QSM Challenge 2.0 (51) were used to compare mcTFI, TFI, and TFI+MERIT. The results were evaluated according to the metrics of QSM Challenge 2.0, which are:

- 1) RMSE over the whole brain
- 2) demeaned and detrended RMSE, ddrRMSE, calculated over the whole brain, over the cortical gray and white matter, over the deep gray matter, and over the venous blood
- 3) linear regression analysis over all voxels in deep gray matter
- 4) streaking artifact level around calcification
- 5) the magnetic moment of the calcification

Both data and evaluation codes are available on the official QSM Challenge 2.0 website: <http://www.listsnu.org/qsm-challenge>.

### In vivo Brain

Eighteen ICH patients were scanned on a commercial 3T scanner (750/SIGNA, General Electric Healthcare, Waukesha Wisconsin, USA) with a unipolar flow compensated multi-echo gradient echo sequence. The acquisition parameters were: FA = 15, FOV = 25.6 cm, TE1 = 4.5–5.0 ms, TR = 39–49 ms, #TE = 6–8,  $\Delta$ TE = 4.6–5 ms, acquisition matrix =  $512 \times 512 \times 64$ –144, reconstructed voxel size =  $0.5 \times 0.5$  mm<sup>2</sup>, reconstructed slice thickness = 1–3 mm, and BW =  $\pm 62.5$  kHz.

Six healthy volunteers were scanned on a prototype 7T MR scanner (MR950, Signa 7.0T, General Electric Healthcare, Waukesha, WI) using a two-channel transmit/32-

channel to receive head coil with a multi-echo gradient echo sequence. The acquisition parameters were: FA = 15, FOV = 220 × 176 mm<sup>2</sup>, TE1 = 3.81 ms, TR = 45.03 ms, #TE = 10, ΔTE = 4.1 ms, acquisition matrix = 320 × 320 × 74, reconstructed voxel size = 0.5×0.5 mm<sup>2</sup>, reconstructed slice thickness = 1 mm, and BW = ± 78.1 kHz.

The image quality of the reconstructed hemorrhage was scored semi-quantitatively based on visually assessed artifacts with a three-point scale (3 = severe, 2 = moderate, and 1 = negligible), by an experienced radiologist (I. K.). The image quality scores (presented as mean ± standard deviation) were compared with each other using a two-tailed Wilcoxon paired-sample signed rank test, and a two-sided  $p < 0.05$  was deemed indicative of statistical significance.

## 5.5 Results

### Simulation

**Figure 5.1** shows the comparison between TFI, TFI+MERIT, and mcTFI in a simulated brain that contains a calcified lesion and an ICH. As shown in **Figure 5.1A** (SNR=100), TFI reconstructed QSM contains severe streaking artifacts that originated from the two lesions. The streaking artifacts were suppressed with the usage of MERIT, but the lesions susceptibilities were underestimated and the lesions themselves appeared enlarged. On the other hand, the mcTFI QSM contains no streaking artifacts, the lesion susceptibilities were in reasonable agreement with ground truth, and the lesions were not enlarged. **Figure 5.1B** showed the mean RMSE over the 10 repeats at different SNR levels, and mcTFI results consistently resulted in better RMSE than the TFI and TFI+MERIT results.

### QSM Challenge 2.0

**Figure 5.2A** shows the QSM reconstructed using TFI, TFI+MERIT, and mcTFI in one of the datasets provided by QSM Challenge 2.0. The TFI result contains streaking artifacts that originate from the calcified lesion. The streaking artifact was suppressed using MERIT, but the lesion size appeared larger than ground truth. The QSM from mcTFI contains the least streaking artifacts from the lesion and the lesion size is not enlarged compared to the ground truth. The QSM from the three methods is otherwise similar outside of the calcified lesion and streaking artifacts. This is also demonstrated in **Figure 5.2B**, where the RMSE and streaking artifact measurements in TFI+MERIT and mcTFI are much better than that in TFI, because both TFI+MERIT and mcTFI results contain minimal streaking artifacts. But between TFI+MERIT and mcTFI, the latter produced more accurate calcification moment measurement compared to the ground truth.

### In vivo Brains with hemorrhages

The image quality scores of the reconstructed hemorrhages for TFI, TFI+MERIT, and mcTFI were respectively  $2.44 \pm 0.62$ ,  $1.78 \pm 0.35$ , and  $1.11 \pm 0.21$ . There was a significant difference between the scores of TFI and TFI+MERIT ( $p=0.002$ ), a significant difference between the scores of TFI and mcTFI ( $p<0.001$ ), and significant difference between the scores of TFI+MERIT and mcTFI ( $p<0.001$ )

**Figure 5.3** shows the QSM reconstructions in a representative ICH brain presented in the three major planes. Severe streaking artifacts coming from the hemorrhage were

observed in the TFI result; these streaking artifacts were significantly reduced in TFI+MERIT, but not completely suppressed (yellow arrow). In mcTFI, the hemorrhage streaking artifacts appeared to be nearly suppressed.

#### *In vivo healthy Brains at 7T*

The image quality scores for TFI, TFI+MERIT, and mcTFI were  $2.86 \pm 0.24$ ,  $2.29 \pm 0.41$ , and  $1.29 \pm 0.041$ , respectively. There was no significant difference between the scores of TFI and TFI+MERIT ( $p=0.102$ ), a significant difference between the scores of TFI and mcTFI ( $p=0.002$ ), and significant difference between the scores of TFI+MERIT and mcTFI ( $p=0.012$ ).

**Figure 5.4** shows the QSM reconstructions in a representative brain scanned at 7T. In case 1, significant artifacts in the prefrontal cortex area were observed in the TFI and TFI+MERIT results (red arrows) while the proposed mcTFI effectively suppressed this artifact.

## **5.6 Discussion**

QSM computes the susceptibility map from a susceptibility field (38,39,52-54), typically with the field first estimated by fitting a signal model to the acquired GRE images. The fitting errors and the non-zero mean Gaussian noise in the resulting fitted susceptibility field propagates through the subsequent dipole inversion step, causing artifacts in the final susceptibility map. The proposed mcTFI method computes the susceptibility map directly from the multi-echo complex GRE images, while minimizing errors in field estimation and retaining the Gaussian noise property in the

data term. The mcTFI method was compared with TFI (without and with MERIT), and mcTFI demonstrated both quantitative and qualitative improvements over TFI in simulations, brains with ICH, and healthy brains scanned at 7T.

The proper biophysical modeling is important for parameter extraction in quantitative MRI. For field estimations in the presence of fat chemical shift, for example, Dimov et al. (55) demonstrated that by modeling the fat chemical shift as part of the unknowns, as opposed to assuming it to be a constant value, the quality, and accuracy resulting estimated field was substantially improved. Prior to this work, the susceptibility field was first estimated via various approximations to Eq. 5.1, where different assumptions to the noise property of the field were made in the different approximations (39,56). For example, the TFI approach here estimated the susceptibility field by solving Eq. 5.7 (a simplified version of Eq. 5.1), in which the magnitude component of the complex images was assumed to be noiseless. The proposed mcTFI, on the other hand, solves the signal equation directly, which is a better signal model with fewer approximations and simplifications.

Another benefit of fitting the susceptibility map directly to the complex data is that the assumed noise in mcTFI is that of the acquired data. A separate field estimation commonly simplifies and alters the noise property, contributing to potential model errors in the subsequent dipole inversion step, which is typically formulated as maximum likelihood estimation by minimizing the quadratic data fidelity term  $\|D\chi - f\|_2^2$ , thereby causing artifacts in the final susceptibility map. A noise weighting term,  $w$ , needs to be introduced to the data fidelity term  $\|w(D\chi - f)\|_2^2$  to

mitigate the model errors and suppress the artifacts (40), but the proper estimation of  $w$  remains a challenge. This noise property related errors are substantial in tissue lesions with large susceptibilities such as hemorrhages and at ultra-high field strengths such as 7T. Accordingly, mcTFI can significantly improve QSM performance for these applications, as demonstrated in this work.

Currently, for field estimation using Eq. 5.7, the noise weighting is calculated as the covariance matrix of the fit in Eq. 5.7 (46), but it does not properly account for the noise properties, as demonstrated by the suboptimal TFI results in this work. Further retuning of  $w$  using MERIT allows better suppression of artifacts from these model errors (41). However, MERIT is a heuristic method and dataset-specific MERIT parameters are required to ensure that MERIT suppresses the artifacts without introducing new artifacts (see appendix C for details regarding the parameters). Looking at the examples in this work, when the MERIT parameters caused over-penalization, then, as shown in **Figure 5.1A**, the streaking artifacts were effectively suppressed, but to over-penalized noise weighting in the voxels in and around the two lesions, led to the solver to fit for the field around the lesions first and the size of the lesions in the resulting susceptibility map appeared larger. In contrast, by using a more accurate model in the data term, mcTFI results demonstrated a sufficient suppression of streaking artifacts while retaining the true size of the lesions. Furthermore, the over-penalization of MERIT likely causes the loss of data in TFI, resulting in less accurate susceptibility map reconstruction in comparison to mcTFI, as shown in **Figure 5.1B**. Similar behaviors were also demonstrated in **Figure 5.2A**, where streaking artifacts

were effectively suppressed using MERIT, but lesions appeared larger. On the other hand, mcTFI was able to suppress streaking artifacts, while avoiding the introduction of new artifacts. **Figure 5.3** demonstrated a case where MERIT failed to completely suppress all streaking artifacts because it did not sufficiently penalize the noise weighting in all problematic voxels; in contrast, the QSM reconstructed using mcTFI suppressed streaking artifacts around the hemorrhage.

There are a few limitations to the current implementation of mcTFI. Firstly, Eq. 5.1 may not fully describe the images from any GRE acquisitions. To model the brain GRE images produced by the acquisition strategy described in the Methods section, additional terms may need to be introduced into Eq. 5.1 to account for other contributions to the signal, including voxel sensitivity function, chemical shift, bipolar readout, shimming gradients, and intravoxel dephasing. Secondly, the nonlinear and nonconvex objective function in mcTFI, by definition, has multiple local minima, and, therefore, its solutions may be sensitive to the choice of initial guess. There is no guarantee that the initial guess strategies as used in this initial implementation are optimal, so the investigation into robust initial guesses is a natural continuation of this work. Finally, an increase of model complexity in mcTFI also comes with an increase in computation time; the Alternating Direction Method of Multipliers (ADMM), which is a much faster algorithm (57), may be used efficiently solve the objective function in mcTFI.

## **5.7 Conclusion**

This work proposed the mcTFI method to directly estimate the susceptibility map from the GRE images, which is a more appropriate way to model the signal noise and bypass any errors from a separate field estimation. Compared to TFI, the proposed mcTFI demonstrated improvements in susceptibility map reconstruction, with reduced streaking artifacts and improved performance in regions with low SNR.

## 5.8 APPENDIX 5A

Starting from Eq. 5.5, let  $W_j = m_0 e^{-t_j R_2^*} e^{i\phi_0} e^{it_j DP y}$ , and  $APy = Py - \overline{Py}^{M_c}$ :

$$E(y) = \underset{y}{\operatorname{argmin}} \sum_{j=1}^{\#TE} \|W_j - S_j\|_2^2 + \lambda_1 \|M_G \nabla P y\|_1 + \lambda_2 \|M_c AP y\|_2^2$$

First order Taylor expansion around  $y$  gives:

$$\begin{aligned} E(y + dy) = & \sum_{j=1}^{\#TE} \left\| \begin{array}{c} W_j - S_j \\ + W_j(it_j DP dy) \end{array} \right\|_2^2 + \lambda_1 \|M_G \nabla P(y + dy)\|_1 \\ & + \lambda_2 \|M_c AP(y + dy)\|_2^2 \end{aligned}$$

The regularizations terms can be reformatted as follows so that the regularizations terms at each  $j$  can be scaled down by  $t_j$ :

$$\begin{aligned} E(y + dy) = & \sum_{j=1}^{\#TE} \left\| \begin{array}{c} W_j - S_j \\ + W_j(it_j DP dy) \end{array} \right\|_2^2 + \lambda_1 \sum_{j=1}^{\#TE} \|t_j M_G \nabla P(y + dy)\|_1 \\ & + \lambda_2 \sum_{j=1}^{\#TE} \|t_j M_c AP(y + dy)\|_2^2 \end{aligned}$$

Let  $B = W_j - S_j$ :

$$E(y + dy) = \sum_{j=1}^{\#TE} \|B + W_j(it_j DP dy)\|_2^2 + \lambda_1 \sum_{j=1}^{\#TE} \|t_j M_G \nabla P(y + dy)\|_1$$

$$+ \lambda_2 \sum_{j=1}^{\#TE} \|t_j M_c AP(y + dy)\|_2^2$$

Gradient of E with respect to  $dy$ :

$$\frac{\delta E}{\delta dy}$$

$$= \frac{\delta}{\delta dy} \left( \begin{array}{c} \sum_{j=1}^{\#TE} dy^H P^H D^H t_j^H i^H W_j^H W_j i t_j DP dy + dy^H P^H D^H t_j^H i^H W_j^H B + B^H W_j i t_j DP dy \\ \lambda_1 \sum_{j=1}^{\#TE} |t_j M_G \nabla P(y + dy)| \\ \lambda_2 \sum_{j=1}^{\#TE} dy^H P^H A^H M^H t_j^H t_j MAP dy + dy^H P^H A^H M^H t_j^H t_j MAP y + y^H P^H A^H M^H t_j^H t_j MAP dy \end{array} \right)$$

$$= \left( \begin{array}{c} \sum_{j=1}^{\#TE} 2\text{Re}\{P^H D^H t_j^H i^H W_j^H W_j i t_j DP dy\} + 2\text{Re}\{P^H D^H t_j^H i^H W_j^H B\} \\ \lambda_1 \sum_{j=1}^{\#TE} P^H \nabla^H M_G^H t_j^H \frac{1}{|t_j M_G \nabla P y|} [t_j M_G \nabla P(y + dy)] \\ \lambda_2 \sum_{j=1}^{\#TE} 2P^H A^H M^H t_j^H t_j MAP dy + 2P^H A^H M^H t_j^H t_j MAP y \end{array} \right)$$

In both  $\lambda_1$  and  $\lambda_2$  terms, since  $t_j$  is the only summation variable and  $t_j$  is scalar, the above expression can be further simplified:

$$\frac{\delta E}{\delta dy} = \begin{pmatrix} \sum_{j=1}^{\#TE} 2\text{Re}\{P^H D^H t_j^H i^H W_j^H W_j i t_j D P dy\} + 2\text{Re}\{P^H D^H t_j^H i^H W_j^H B\} \\ \lambda_1 \left( \sum_{j=1}^{\#TE} t_j \right) P^H \nabla^H M_G^H \frac{1}{|M_G \nabla P y|} [M_G \nabla P (y + dy)] \\ \lambda_2 \left( \sum_{j=1}^{\#TE} t_j^2 \right) 2P^H A^H M^H M A P dy + 2P^H A^H M^H M A P y \end{pmatrix}$$

Settings the gradients to zero:

$$\begin{pmatrix} \sum_{j=1}^{\#TE} 2\text{Re}\{P^H D^H t_j^H i^H W_j^H W_j i t_j D P dy\} \\ \lambda_1 \left( \sum_{j=1}^{\#TE} t_j \right) P^H \nabla^H M_G^H \frac{1}{|M_G \nabla P y|} [M_G \nabla P dy] \\ \lambda_2 \left( \sum_{j=1}^{\#TE} t_j^2 \right) 2P^H A^H M^H M A P dy \end{pmatrix}$$

$$= \begin{pmatrix} \sum_{j=1}^{\#TE} 2\text{Re}\{P^H D^H t_j^H i^H W_j^H B\} \\ \lambda_1 \left( \sum_{j=1}^{\#TE} t_j \right) P^H \nabla^H M_G^H \frac{1}{|M_G \nabla P y|} [M_G \nabla P y] \\ \lambda_2 \left( \sum_{j=1}^{\#TE} t_j^2 \right) 2P^H A^H M^H M A P y \end{pmatrix}$$

## 5.9 APPENDIX 5B

$$(m'_0, R_2^*, \phi'_0) = \underset{m_0, R_2^*, \phi_0}{\operatorname{argmin}} \sum_{j=1}^{\#TE} \left\| m_0 e^{-t_j R_2^*} e^{i\phi_0} e^{it_j DP y_{n+1}} - S_j \right\|_2^2 + \lambda_3 \left\| \begin{array}{c} dm_0 \\ dR_2^* \\ d\phi_0 \end{array} \right\|_2^2$$

First order Taylor expansion:

$$\begin{aligned} E(m_0 + dm_0, R_2^* + dR_2^*, \phi_0 + d\phi_0) \\ = \sum_{j=1}^{\#TE} \left\| \begin{array}{c} m_0 e^{-t_j R_2^*} e^{i\phi_0} e^{it_j DP y_{n+1}} - S_j \\ + m_0 e^{-t_j R_2^*} e^{i\phi_0} e^{it_j DP y_{n+1}} \left( \frac{dm_0}{m_0} \right) \\ + m_0 e^{-t_j R_2^*} e^{i\phi_0} e^{it_j DP y_{n+1}} (-t_j dR_2^*) \\ + m_0 e^{-t_j R_2^*} e^{i\phi_0} e^{it_j DP y_{n+1}} (id\phi_0) \end{array} \right\|_2^2 + \lambda_3 \left\| \begin{array}{c} dm_0 \\ dR_2^* \\ d\phi_0 \end{array} \right\|_2^2 \end{aligned}$$

Let  $W_j = m_0 e^{-t_j R_2^*} e^{i\phi_0} e^{it_j DP y_{n+1}}$ , and  $B = W_j - S_j$

$$\begin{aligned} E(m_0 + dm_0, R_2^* + dR_2^*, \phi_0 + d\phi_0) \\ = \sum_{j=1}^{\#TE} \left\| W_j \left( \frac{dm_0}{m_0} - t_j dR_2^* + id\phi_0 \right) + B \right\|_2^2 + \lambda_3 \left\| \begin{array}{c} dm_0 \\ dR_2^* \\ d\phi_0 \end{array} \right\|_2^2 \\ = \sum_{j=1}^{\#TE} \left[ W_j \left( \frac{dm_0}{m_0} - t_j dR_2^* + id\phi_0 \right) + B \right]^H \left[ W_j \left( \frac{dm_0}{m_0} - t_j dR_2^* + id\phi_0 \right) + B \right] \\ + \lambda_3 \left[ \begin{array}{c} dm_0 \\ dR_2^* \\ d\phi_0 \end{array} \right]^H \left[ \begin{array}{c} dm_0 \\ dR_2^* \\ d\phi_0 \end{array} \right] \end{aligned}$$

Gradient of E with respect to  $dm_0$ ,  $dR_2^*$ , and  $d\phi_0$ :

$$\begin{aligned}
& \frac{\delta E}{\delta dm_0} \\
&= \frac{\delta}{\delta dm_0} \left( \sum_{j=1}^{\#TE} \left[ \left( \frac{dm_0}{m_0} \right)^H W_j^H W_j \frac{dm_0}{m_0} - \left( \frac{dm_0}{m_0} \right)^H W_j^H W_j t_j dR_2^* + \left( \frac{dm_0}{m_0} \right)^H W_j^H W_j id\phi_0 \right. \right. \\
&\quad \left. \left. + \left( \frac{dm_0}{m_0} \right)^H W_j^H B - (t_j dR_2^*)^H W_j^H W_j \frac{dm_0}{m_0} + (id\phi_0)^H W_j^H W_j \frac{dm_0}{m_0} + (B)^H W_j \frac{dm_0}{m_0} \right] \right. \\
&\quad \left. + \lambda_3 (dm_0^H dm_0) \right) \\
&= \sum_{j=1}^{\#TE} \left[ \left( \frac{W_j^H}{m_0} \frac{W_j}{m_0} + \left( \frac{W_j^H}{m_0} \frac{W_j}{m_0} \right)^H \right) dm_0 - \left( \frac{W_j^H}{m_0} W_j t_j dR_2^* + (t_j dR_2^*)^H W_j^H \frac{W_j}{m_0} \right) \right. \\
&\quad \left. + \left( \frac{W_j^H}{m_0} W_j id\phi_0 + (id\phi_0)^H W_j^H \frac{W_j}{m_0} \right) + \left( \frac{W_j^H}{m_0} B + (B)^H \frac{W_j}{m_0} \right) \right] + 2\lambda_3 dm_0 \\
&= \sum_{j=1}^{\#TE} \left[ 2Re \left\{ \frac{W_j^H}{m_0} \frac{W_j}{m_0} dm_0 \right\} - 2Re \left\{ \frac{W_j^H}{m_0} W_j t_j dR_2^* \right\} + 2Re \left\{ \frac{W_j^H}{m_0} W_j id\phi_0 \right\} \right. \\
&\quad \left. + 2Re \left\{ \frac{W_j^H}{m_0} B \right\} \right] + 2\lambda_3 dm_0
\end{aligned}$$

$$\begin{aligned}
& \frac{\delta E}{\delta dR_2^*} \\
&= \frac{\delta}{\delta dR_2^*} \left( \sum_{j=1}^{\#TE} \left[ -dR_2^{*H} t_j^H W_j^H W_j \frac{dm_0}{m_0} + dR_2^{*H} t_j^H W_j^H W_j t_j dR_2^* - dR_2^{*H} t_j^H W_j^H W_j id\phi_0 \right. \right. \\
&\quad \left. \left. - dR_2^{*H} t_j^H W_j^H B - \left( \frac{dm_0}{m_0} \right)^H W_j^H W_j t_j dR_2^* - (id\phi_0)^H W_j^H W_j t_j dR_2^* - (B)^H W_j t_j dR_2^* \right] \right. \\
&\quad \left. + \lambda_3 (dR_2^{*H} dR_2^*) \right) \\
&= \sum_{j=1}^{\#TE} \left[ - \left( t_j^H W_j^H W_j \frac{dm_0}{m_0} + \left( \frac{dm_0}{m_0} \right)^H W_j^H W_j t_j \right) \right. \\
&\quad + \left( t_j^H W_j^H W_j t_j + (t_j^H W_j^H W_j t_j)^H \right) dR_2^* - \left( t_j^H W_j^H W_j id\phi_0 + (id\phi_0)^H W_j^H W_j t_j \right) \\
&\quad \left. - (t_j^H W_j^H B + (B)^H W_j t_j) \right] + 2\lambda_3 dR_2^* \\
&= \sum_{j=1}^{\#TE} \left[ -2Re \left\{ t_j^H W_j^H W_j \frac{dm_0}{m_0} \right\} + 2Re \{ t_j^H W_j^H W_j t_j dR_2^* \} - 2Re \{ t_j^H W_j^H W_j id\phi_0 \} \right. \\
&\quad \left. - 2Re \{ t_j^H W_j^H B \} \right] + 2\lambda_3 dR_2^*
\end{aligned}$$

$$\begin{aligned}
& \frac{\delta E}{\delta d\phi_0} \\
&= \frac{\delta}{\delta d\phi_0} \left( \sum_{j=1}^{\#TE} \left[ d\phi_0^H i^H W_j^H W_j \frac{dm_0}{m_0} - d\phi_0^H i^H W_j^H W_j t_j dR_2^* + d\phi_0^H i^H W_j^H W_j id\phi_0 + d\phi_0^H i^H W_j^H B \right] \right. \\
&\quad \left. + \left( \frac{dm_0}{m_0} \right)^H W_j^H W_j id\phi_0 - (t_j dR_2^*)^H W_j^H W_j id\phi_0 + (B)^H W_j id\phi_0 \right) \\
&\quad + \lambda_3 (d\phi_0^H d\phi_0) \\
&= \sum_{j=1}^{\#TE} \left[ \left( i^H W_j^H W_j \frac{dm_0}{m_0} + \left( \frac{dm_0}{m_0} \right)^H W_j^H W_j i \right) - \left( i^H W_j^H W_j t_j dR_2^* + (t_j dR_2^*)^H W_j^H W_j i \right) \right. \\
&\quad \left. + \left( i^H W_j^H W_j i + (i^H W_j^H W_j i)^H \right) d\phi_0 + \left( i^H W_j^H B + (B)^H W_j i \right) \right] + 2\lambda_3 d\phi_0 \\
&= \sum_{j=1}^{\#TE} \left[ 2Re \left\{ i^H W_j^H W_j \frac{dm_0}{m_0} \right\} - 2Re \{ i^H W_j^H W_j t_j dR_2^* \} + 2Re \{ i^H W_j^H W_j id\phi_0 \} \right. \\
&\quad \left. + 2Re \{ i^H W_j^H B \} \right] + 2\lambda_3 d\phi_0
\end{aligned}$$

Settings the gradients to zero:

$$\sum_{j=1}^{\#TE} \left[ Re \left\{ \frac{W_j^H}{m_0} W_j \left( \frac{dm_0}{m_0} - t_j dR_2^* + id\phi_0 \right) \right\} \right] + \lambda_3 dm_0 = \sum_{j=1}^{\#TE} \left[ -Re \left\{ \frac{W_j^H}{m_0} B \right\} \right]$$

$$\sum_{j=1}^{\#TE} \left[ -Re \left\{ t_j^H W_j^H W_j \left( \frac{dm_0}{m_0} - t_j dR_2^* + id\phi_0 \right) \right\} \right] + \lambda_3 dR_2^* = \sum_{j=1}^{\#TE} \left[ Re \{ t_j^H W_j^H B \} \right]$$

$$\sum_{j=1}^{\#TE} \left[ \text{Re} \left\{ i^H W_j^H W_j \left( \frac{dm_0}{m_0} - t_j dR_2^* + id\phi_0 \right) \right\} \right] + \lambda_3 d\phi_0 = \sum_{j=1}^{\#TE} \left[ -\text{Re} \{ i^H W_j^H B \} \right]$$

## 5.10 APPENDIX 5C

The threshold,  $T$ , needs to be selected such that only the unreliable voxels in the data have their noise weighting reduced. As such, if  $T$  is smaller than the optimal value, then some of the reliable voxels would be penalized, resulting in the loss of data, but if  $T$  is larger than the optimal value, then some unreliable voxels would not be penalized, allowing these voxels to continue to generate artifacts in the solution. The attenuation factor,  $R$ , determines how much the noise weightings in voxels, that were picked up by a given  $T$ , are reduced. Large  $R$  could cause voxels to be over-penalized, leading to the loss of data, and small  $R$  could result in insufficient noise weighting reduction in unreliable voxels and insufficient suppression of artifacts. The current implementation of MERIT uses the parameters  $T = 6\sigma$ , where  $\sigma$  is the standard deviation of the two-norm of the data-term residual,  $\rho$ , therefore, assuming that  $\rho$  is a Gaussian distribution, 0.3% of the voxels are penalized by MERIT at every GN iteration. In practice, however, it is unlikely that precisely 0.3% of voxels in every GN iteration contain model errors. Furthermore, the current MERIT implementation uses  $R = 2$ , such that the noise weighting in the selection voxels are reduced by a factor of  $\left(\frac{\rho_i}{T}\right)^2$ , but there is no guarantee that this reduction factor will always return a more

appropriate noise weighting. Implementation of MERIT can be found in the MEDI  
opensource toolbox: <http://pre.weill.cornell.edu/mri/pages/qsm.html>

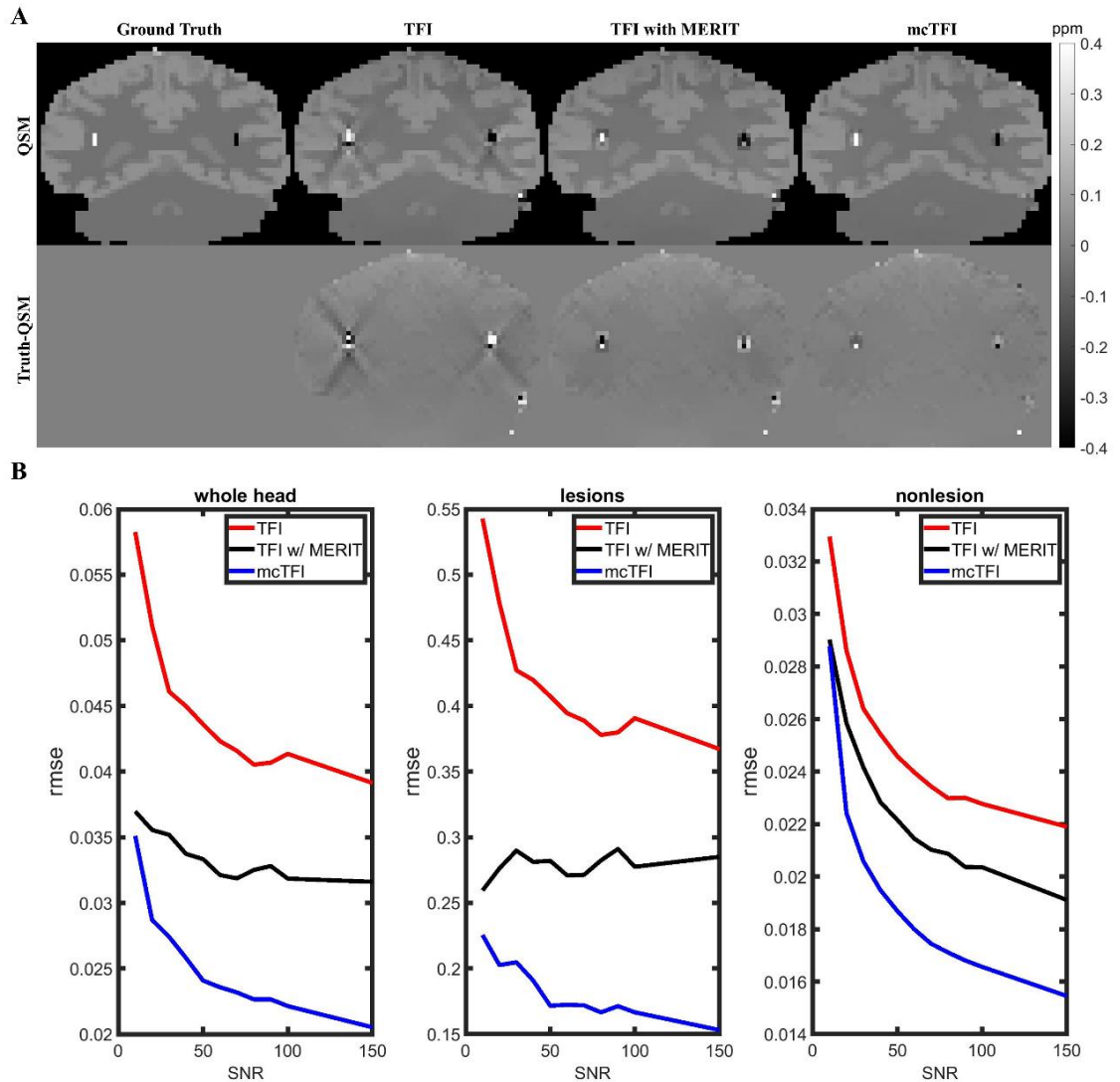
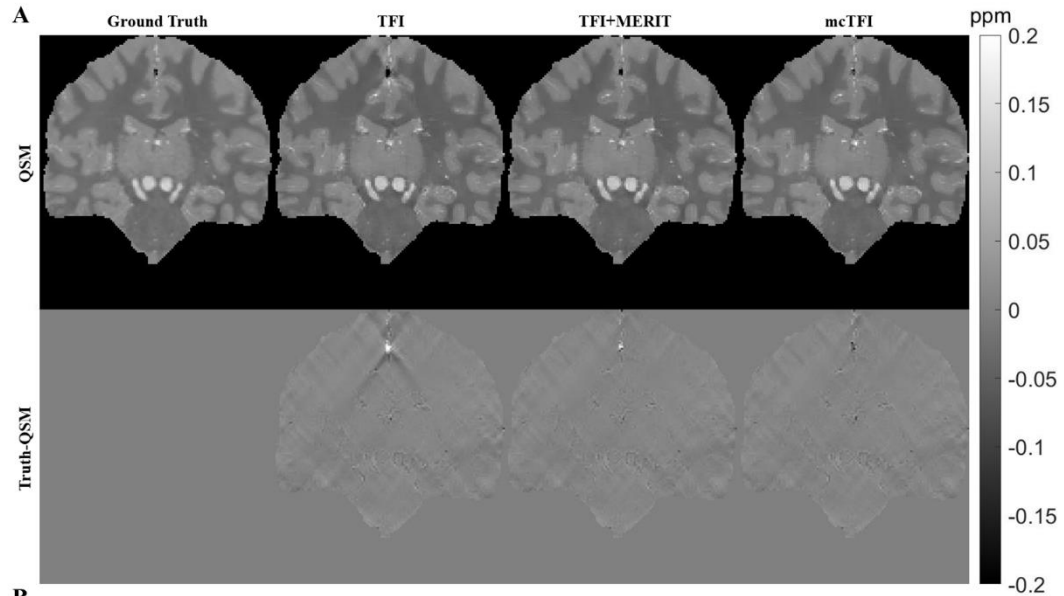


Figure 5.1. A) comparison between TFI, TFI+MERIT, and mcTFI in a simulated brain that contains a calcified lesion and an ICH. TFI contains streaking artifacts that originated from the two lesions, due to improper noise weighting in voxels around the lesions. MERIT helped to suppress the streaking artifacts, but the size of the lesion appeared enlarged. mcTFI suppressed the streaking artifacts and reconstructed the lesions best resembled the ground truth. B) mcTFI results also have the best RMSE at all different SNR levels.



**B**

		RMSE	ddRMSE Whole	ddRMSE Tissue	ddRMSE Blood	ddRMSE DGM	1-Slope	Streaking Around Calcification	Deviation True Calcification Moment
SNR 1	TFI	45.49	46.08	53.52	91.65	25.56	<b>0.020</b>	0.061	20.23
	TFI+MERIT	40.89	41.33	48.18	79.66	23.97	0.022	0.020	6.63
	mcTFI	<b>37.97</b>	<b>39.27</b>	<b>46.06</b>	<b>76.98</b>	<b>23.25</b>	0.023	<b>0.015</b>	<b>3.06</b>
SNR 2	TFI	40.70	41.18	47.30	85.98	22.58	<b>0.029</b>	0.049	18.48
	TFI+MERIT	36.90	<b>37.24</b>	<b>41.68</b>	77.40	<b>21.22</b>	<b>0.029</b>	0.015	5.34
	mcTFI	<b>36.14</b>	37.26	42.81	<b>76.16</b>	21.64	0.034	<b>0.014</b>	<b>3.37</b>

Figure 5.2. A) comparison between TFI, TFI+MERIT, and mcTFI in one of the datasets provided by the QSM Challenge 2.0. TFI contains streaking artifacts that originated from the calcification, whereas both TFI+MERIT and mcTFI were able to suppress the streaking artifacts. B) mcTFI demonstrated a more accurate reconstruction (last two columns) of the calcification than TFI+MERIT (bold indicate the best value).

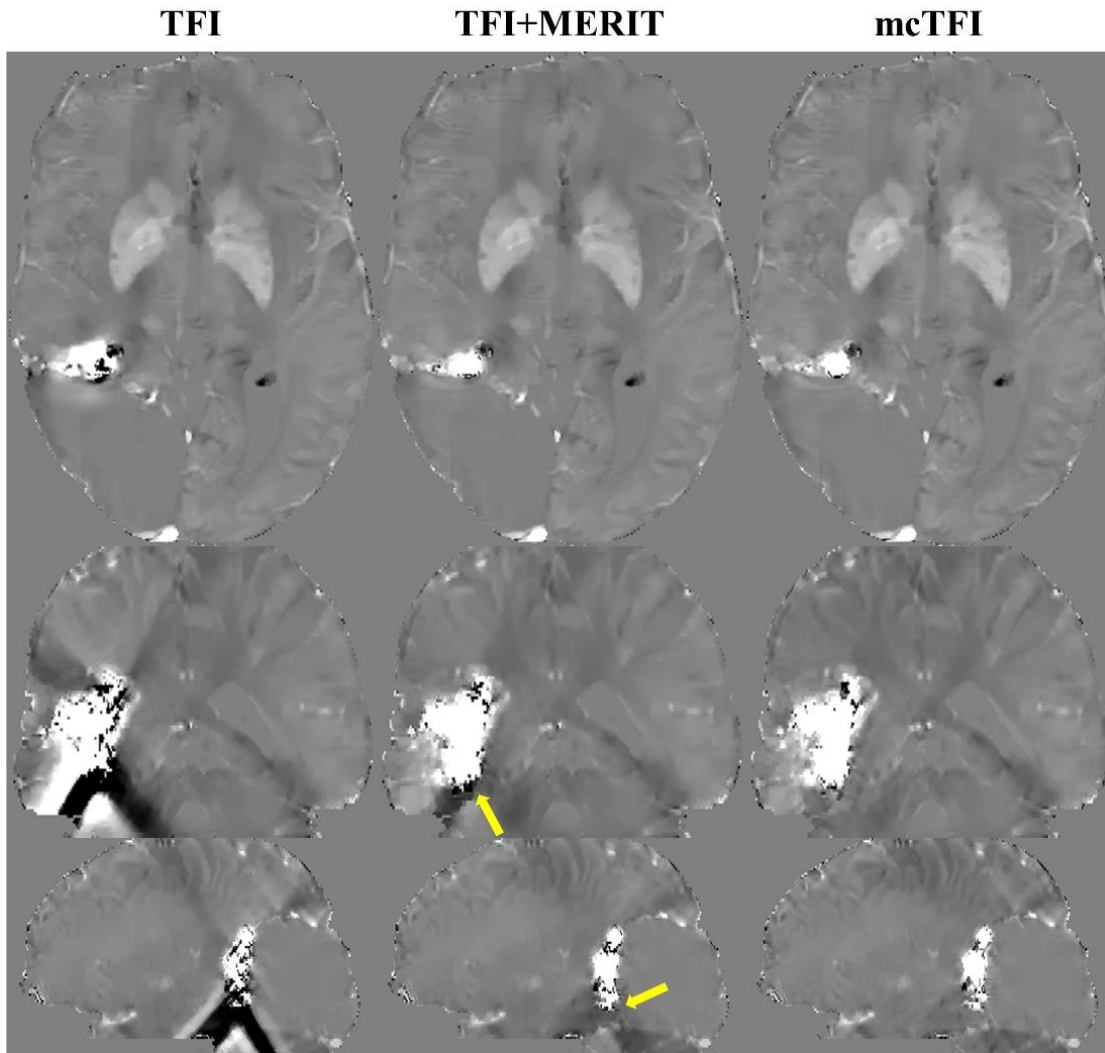


Figure 5.3. QSM reconstructions in a brain with the large ICH. Severe streaking artifacts were observed in the TFI result. TFI+MERIT reduced the severity of the streaking artifacts but did not completely suppress them (yellow arrows), likely because MERIT did not properly penalize all of the problematic voxels. The streaking artifacts were the smallest in the mcTFI reconstructed susceptibility map.

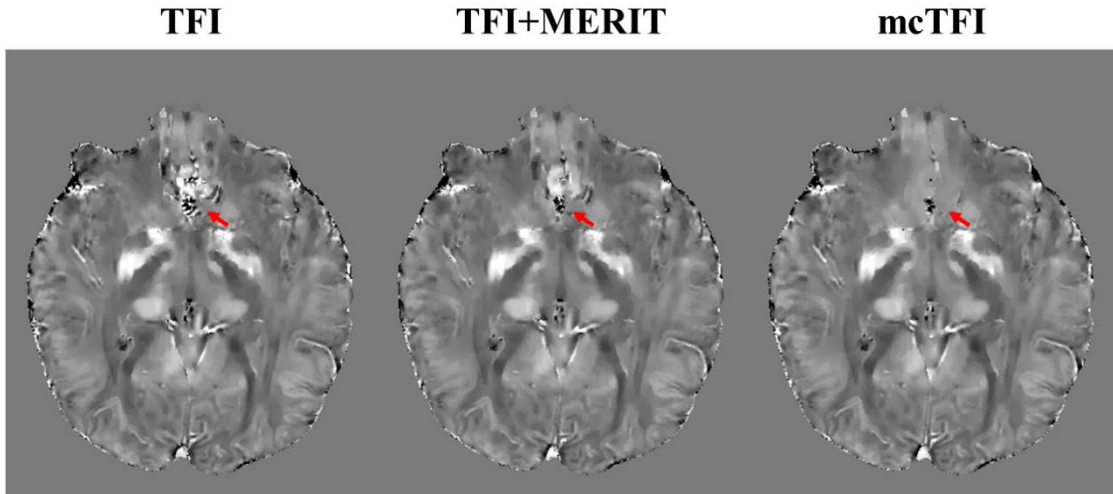


Figure 5.4. A representative healthy brain scanned at a 7T scanner. Significant artifacts in the prefrontal cortex area were observed in the TFI and TFI+MERIT results (red arrows) and proposed mcTFI effectively suppressed such artifact.

## CHAPTER 6

### CONCLUSION AND FUTURE DIRECTIONS

#### 6.1 Cardiac QSM

This dissertation detailed the framework, for both data acquisition techniques and post-processing methods, to generate high-quality cardiac QSM maps. This work demonstrated, for the first time, the feasibility of *in vivo* cardiac QSM, and provided the initial validation of QSM based SvO<sub>2</sub> through comparison with invasive catheterization measurements.

A major limitation of the current cardiac QSM is that the scan time of the cardiac QSM pulse sequence presented is long (~4-7 minutes) compared to other routine clinical cardiac MRI sequences. One approach to shorten scan time is to increase parallel acceleration factor, use compressed sensing (73,107), and/or apply data acquisition strategies such as echo planar readout (72) or echo sharing methods (74). Non-Cartesian acquisitions that allow for self-gating (108) and multi-phase reconstruction (109) are also alternatives to shorten cardiac QSM. Deep-learning reconstruction could also be employed to vastly reduce the k-space coverage needed to generate the cardiac GRE images for QSM reconstruction (175).

#### 6.2 Carotid QSM

The work in this dissertation demonstrated that QSM maps can be reconstructed using the proposed non-linear formulation of TFI (MEDInpt). The reconstructed QSM maps can distinguish calcification and IPH in advanced atherosclerotic carotid plaques in good agreement with findings on mcMRI.

However, the current data acquisition of carotid QSM is not robust against motion artifacts; 18% of the patient cases presented in chapter 4 resulted in unreasonable QSM maps due to excessive motion artifacts in the source GRE images. Real time navigators gating, such as the one presented in chapter 3, may be implemented to compensate for the motion during the scan. Deep learning frameworks may also retrospectively correct the source GRE images with motion artifacts (176).

### **6.3 Multi-Echo Complex Total Field Inversion (mcTFI) Method**

This dissertation proposed the mcTFI method to directly estimate the susceptibility map from the GRE images, which is a more appropriate way to model the signal noise and bypass any errors from a separate field estimation. Compared to TFI, the proposed mcTFI demonstrated improvements in susceptibility map reconstruction, in regions with low SNR.

A few improvements for mcTFI as suggested as follows. Firstly, the data fidelity term used in mcTFI presented in chapter 5 may not fully describe the images from any multi echo GRE acquisitions, therefore, additional terms may need to be introduced into to the data fidelity term to account for other contributors to signals, such as fat, bipolar readout, shimming gradient, and voxels dephasing. Secondly, the non-linear

multi-echo fitting of mcTFI also comes with an increase in computation time; the Alternating Direction Method of Multipliers (ADMM), which is a much faster algorithm (174), can be implemented to efficiently solve the objective function in mcTFI. Finally, the GRE images used in the current mcTFI are not the source images from the GRE acquisition, but rather, they are coil combined from the source images. A further improvement to mcTFI, therefore, would be to fit the susceptibility map directly to the original multi-coil multi-echo GRE images.

## BIBLIOGRAPHY

1. Marques JP, Bowtell R. Application of a Fourier-based method for rapid calculation of field inhomogeneity due to spatial variation of magnetic susceptibility. *Concepts in Magnetic Resonance Part B: Magnetic Resonance Engineering* 2005;25B(1):65-78.
2. Salomir R, de Senneville BD, Moonen CT. A fast calculation method for magnetic field inhomogeneity due to an arbitrary distribution of bulk susceptibility. *Concepts in Magnetic Resonance Part B: Magnetic Resonance Engineering* 2003;19B(1):26-34.
3. de Rochefort L, Nguyen T, Brown R, Spincemaille P, Choi G, Weinsaft J, Prince MR, Wang Y. In vivo quantification of contrast agent concentration using the induced magnetic field for time-resolved arterial input function measurement with MRI. *Med Phys* 2008;35(12):5328-5339.
4. Magnetic Properties of Tissues. *Magnetic Resonance Imaging*. p 739-777.
5. Deistung A, Schweser F, Reichenbach JR. Overview of quantitative susceptibility mapping. *NMR in Biomedicine* 2016:doi:10.1002/nbm.3569.
6. Wang Y, Liu T. Quantitative susceptibility mapping (QSM): Decoding MRI data for a tissue magnetic biomarker. *Magnetic Resonance in Medicine* 2015;73(1):82-101.
7. Haacke EM, Liu S, Buch S, Zheng W, Wu D, Ye Y. Quantitative susceptibility mapping: current status and future directions. *Magnetic Resonance Imaging* 2015;33(1):1-25.
8. Cusack R, Papadakis N. New Robust 3-D Phase Unwrapping Algorithms: Application to Magnetic Field Mapping and Undistorting Echoplanar Images. *NeuroImage* 2002;16(3, Part A):754-764.
9. Dong J, Liu T, Chen F, Zhou D, Dimov A, Raj A, Cheng Q, Spincemaille P, Wang Y. Simultaneous Phase Unwrapping and Removal of Chemical Shift (SPURS) Using Graph Cuts: Application in Quantitative Susceptibility Mapping. *IEEE Transactions on Medical Imaging* 2015;34(2):531-540.
10. Kee Y, Liu Z, Zhou L, Dimov A, Cho J, de Rochefort L, Seo JK, Wang Y. Quantitative Susceptibility Mapping (QSM) Algorithms: Mathematical Rationale and Computational Implementations. *IEEE Trans Biomed Eng* 2017;64(11):2531-2545.
11. Liu Z, Kee Y, Zhou D, Wang Y, Spincemaille P. Preconditioned total field inversion (TFI) method for quantitative susceptibility mapping. *Magnetic Resonance in Medicine* 2017;78(1):303-315.

12. Liu S, Wang C, Zhang X, Zuo P, Hu J, Haacke EM, Ni H. Quantification of liver iron concentration using the apparent susceptibility of hepatic vessels. *Quantitative Imaging in Medicine and Surgery* 2018;8(2):123-134.
13. Chen Q, Chen Y, Zhang Y, Wang F, Yu H, Zhang C, Jiang Z, Luo W. Iron deposition in Parkinson's disease by quantitative susceptibility mapping. *BMC Neuroscience* 2019;20(1):23.
14. Langkammer C, Schweser F, Krebs N, Deistung A, Goessler W, Scheurer E, Sommer K, Reishofer G, Yen K, Fazekas F, Ropele S, Reichenbach JR. Quantitative susceptibility mapping (QSM) as a means to measure brain iron? A post mortem validation study. *NeuroImage* 2012;62(3):1593-1599.
15. Chen W, Gauthier SA, Gupta A, Comunale J, Liu T, Wang S, Pei M, Pitt D, Wang Y. Quantitative susceptibility mapping of multiple sclerosis lesions at various ages. *Radiology* 2014;271(1):183-192.
16. Zhang Y, Gauthier SA, Gupta A, Comunale J, Chia-Yi Chiang G, Zhou D, Chen W, Giambrone AE, Zhu W, Wang Y. Longitudinal change in magnetic susceptibility of new enhanced multiple sclerosis (MS) lesions measured on serial quantitative susceptibility mapping (QSM). *J Magn Reson Imaging* 2016;44(2):426-432.
17. Murakami Y, Kakeda S, Watanabe K, Ueda I, Ogasawara A, Moriya J, Ide S, Futatsuya K, Sato T, Okada K, Uozumi T, Tsuji S, Liu T, Wang Y, Korogi Y. Usefulness of quantitative susceptibility mapping for the diagnosis of Parkinson disease. *AJNR American journal of neuroradiology* 2015;36(6):1102-1108.
18. Acosta-Cabronero J, Williams GB, Cardenas-Blanco A, Arnold RJ, Lupson V, Nestor PJ. In vivo quantitative susceptibility mapping (QSM) in Alzheimer's disease. *PloS one* 2013;8(11):e81093.
19. Ayton S, Fazlollahi A, Bourgeat P, Raniga P, Ng A, Lim YY, Diouf I, Farquharson S, Frupp J, Ames D, Doecke J, Desmond P, Ordidge R, Masters CL, Rowe CC, Maruff P, Villemagne VL, Salvado O, Bush AI. Cerebral quantitative susceptibility mapping predicts amyloid-beta-related cognitive decline. *Brain : a journal of neurology* 2017;140(8):2112-2119.
20. Kim HG, Park S, Rhee HY, Lee KM, Ryu CW, Rhee SJ, Lee SY, Wang Y, Jahng GH. Quantitative susceptibility mapping to evaluate the early stage of Alzheimer's disease. *NeuroImage Clinical* 2017;16:429-438.
21. Wang Y, Spincemille P, Liu Z, Dimov A, Deh K, Li J, Zhang Y, Yao Y, Gillen KM, Wilman AH, Gupta A, Tsiouris AJ, Kovanlikaya I, Chiang GC-Y, Weinsaft JW, Tanenbaum L, Chen W, Zhu W, Chang S, Lou M, Kopell BH, Kaplitt MG, Devos D, Hirai T, Huang X, Korogi Y, Shtilbans A, Jahng G-H,

- Pelletier D, Gauthier SA, Pitt D, Bush AI, Brittenham GM, Prince MR. Clinical quantitative susceptibility mapping (QSM): Biometal imaging and its emerging roles in patient care. *Journal of Magnetic Resonance Imaging* 2017;46(4):951-971.
22. Eskreis-Winkler S, Zhang Y, Zhang J, Liu Z, Dimov A, Gupta A, Wang Y. The clinical utility of QSM: disease diagnosis, medical management, and surgical planning. *NMR in Biomedicine* 2016;doi:10.1002/nbm.3668.
  23. Wen Y, Nguyen TD, Liu Z, Spincemaille P, Zhou D, Dimov A, Kee Y, Deh K, Kim J, Weinsaft JW, Wang Y. Cardiac quantitative susceptibility mapping (QSM) for heart chamber oxygenation. *Magn Reson Med* 2018;79(3):1545-1552.
  24. Wen Y, Weinsaft JW, Nguyen TD, Liu Z, Horn EM, Singh H, Kochav J, Eskreis-Winkler S, Deh K, Kim J, Prince MR, Wang Y, Spincemaille P. Free breathing three-dimensional cardiac quantitative susceptibility mapping for differential cardiac chamber blood oxygenation – initial validation in patients with cardiovascular disease inclusive of direct comparison to invasive catheterization. *Journal of Cardiovascular Magnetic Resonance* 2019;21(1):70.
  25. Robin E, Costecalde M, Lebuffe G, Vallet B. Clinical relevance of data from the pulmonary artery catheter. *Critical Care* 2006;10(3):1-10.
  26. Brovman EY, Gabriel RA, Dutton RP, Urman RD. Pulmonary Artery Catheter Use During Cardiac Surgery in the United States, 2010 to 2014. *Journal of Cardiothoracic and Vascular Anesthesia* 2016;30(3):579-584.
  27. Judge O, Ji F, Fleming N, Liu H. Current Use of the Pulmonary Artery Catheter in Cardiac Surgery: A Survey Study. *Journal of Cardiothoracic and Vascular Anesthesia* 2015;29(1):69-75.
  28. Jesurum J. Svo2 Monitoring. *Critical Care Nurse* 2004;24(4):73-76.
  29. Nield LE, Qi X-LL, Valsangiacomo ER, Macgowan CK, Wright GA, Hornberger LK, Yoo S-J. In vivo MRI measurement of blood oxygen saturation in children with congenital heart disease. *Pediatric Radiology* 2005;35(2):179-185.
  30. Wedegärtner U, Kooijman H, Yamamura J, Frisch M, Weber C, Buchert R, Huff A, Hecher K, Adam G. In vivo MRI measurement of fetal blood oxygen saturation in cardiac ventricles of fetal sheep: A feasibility study. *Magnetic Resonance in Medicine* 2010;64(1):32-41.
  31. Wright GA, Hu BS, Macovski A. Estimating oxygen saturation of blood in vivo with MR imaging at 1.5 T. *Journal of Magnetic Resonance Imaging* 1991;1(3):275-283.

32. Langham MC, Magland JF, Epstein CL, Floyd TF, Wehrli FW. Accuracy and precision of MR blood oximetry based on the long paramagnetic cylinder approximation of large vessels. *Magnetic Resonance in Medicine* 2009;62(2):333-340.
33. Thulborn KR, Waterton JC, Matthews PM, Radda GK. Oxygenation dependence of the transverse relaxation time of water protons in whole blood at high field. *Biochimica et Biophysica Acta (BBA) - General Subjects* 1982;714(2):265-270.
34. Qin Q, Grgac K, van Zijl PCM. Determination of whole-brain oxygen extraction fractions by fast measurement of blood T2 in the jugular vein. *Magnetic resonance in medicine : official journal of the Society of Magnetic Resonance in Medicine / Society of Magnetic Resonance in Medicine* 2011;65(2):471-479.
35. Nield LE, Qi X, Yoo S-J, Valsangiacomo ER, Hornberger LK, Wright GA. MRI-based blood oxygen saturation measurements in infants and children with congenital heart disease. *Pediatric Radiology* 2002;32(7):518-522.
36. Krishnamurthy LC, Liu P, Xu F, Uh J, Dimitrov I, Lu H. Dependence of blood T(2) on oxygenation at 7T: in vitro calibration and in vivo application. *Magnetic resonance in medicine : official journal of the Society of Magnetic Resonance in Medicine / Society of Magnetic Resonance in Medicine* 2014;71(6):2035-2042.
37. Zhao JM, Clingman CS, Närväinen MJ, Kauppinen RA, van Zijl PCM. Oxygenation and hematocrit dependence of transverse relaxation rates of blood at 3T. *Magnetic Resonance in Medicine* 2007;58(3):592-597.
38. Silvennoinen MJ, Clingman CS, Golay X, Kauppinen RA, van Zijl PCM. Comparison of the dependence of blood R2 and R 2\* on oxygen saturation at 1.5 and 4.7 Tesla. *Magnetic Resonance in Medicine* 2003;49(1):47-60.
39. Spees WM, Yablonskiy DA, Oswood MC, Ackerman JJH. Water proton MR properties of human blood at 1.5 Tesla: Magnetic susceptibility, T1, T2, T \*2, and non-Lorentzian signal behavior. *Magnetic Resonance in Medicine* 2001;45(4):533-542.
40. Li D, Wang Y, Waight DJ. Blood oxygen saturation assessment in vivo using T2 \* estimation. *Magnetic Resonance in Medicine* 1998;39(5):685-690.
41. Jain V, Abdulmalik O, Propert KJ, Wehrli FW. Investigating the magnetic susceptibility properties of fresh human blood for noninvasive oxygen saturation quantification. *Magnetic Resonance in Medicine* 2012;68(3):863-867.

42. Zhang J, Zhou D, Nguyen TD, Spincemaille P, Gupta A, Wang Y. Cerebral metabolic rate of oxygen (CMRO<sub>2</sub>) mapping with hyperventilation challenge using quantitative susceptibility mapping (QSM). *Magnetic Resonance in Medicine* 2016;doi:10.1002/mrm.26253.
43. Schweser F, Deistung A, Reichenbach JR. Foundations of MRI phase imaging and processing for Quantitative Susceptibility Mapping (QSM). *Zeitschrift für Medizinische Physik* 2016;26(1):6-34.
44. Liu J, Liu T, de Rochefort L, Ledoux J, Khalidov I, Chen W, Tsiouris AJ, Wisnieff C, Spincemaille P, Prince MR, Wang Y. Morphology enabled dipole inversion for quantitative susceptibility mapping using structural consistency between the magnitude image and the susceptibility map. *NeuroImage* 2012;59(3):2560-2568.
45. de Rochefort L, Liu T, Kressler B, Liu J, Spincemaille P, Lebon V, Wu J, Wang Y. Quantitative susceptibility map reconstruction from MR phase data using bayesian regularization: Validation and application to brain imaging. *Magnetic Resonance in Medicine* 2010;63(1):194-206.
46. Liu C, Li W, Tong KA, Yeom KW, Kuzminski S. Susceptibility-weighted imaging and quantitative susceptibility mapping in the brain. *Journal of Magnetic Resonance Imaging* 2015;42(1):23-41.
47. Xu B, Liu T, Spincemaille P, Prince M, Wang Y. Flow compensated quantitative susceptibility mapping for venous oxygenation imaging. *Magnetic Resonance in Medicine* 2014;72(2):438-445.
48. Fan AP, Bilgic B, Gagnon L, Witzel T, Bhat H, Rosen BR, Adalsteinsson E. Quantitative oxygenation venography from MRI phase. *Magnetic Resonance in Medicine* 2014;72(1):149-159.
49. Dibb R, Qi Y, Liu C. Magnetic susceptibility anisotropy of myocardium imaged by cardiovascular magnetic resonance reflects the anisotropy of myocardial filament  $\alpha$ -helix polypeptide bonds. *Journal of Cardiovascular Magnetic Resonance* 2015;17(1):60.
50. Wang Y, Riederer SJ, Ehman RL. Respiratory motion of the heart: kinematics and the implications for the spatial resolution in coronary imaging. *Magn Reson Med* 1995;33(5):713-719.
51. Wang Y, Rossman PJ, Grimm RC, Riederer SJ, Ehman RL. Navigator-echo-based real-time respiratory gating and triggering for reduction of respiration effects in three-dimensional coronary MR angiography. *Radiology* 1996;198(1):55-60.

52. Liu Z, Kee Y, Zhou D, Wang Y, Spincemaille P. Preconditioned total field inversion (TFI) method for quantitative susceptibility mapping. *Magn Reson Med* 2016.
53. Hoffman R, Silberstein LE, Heslop H, Weitz J. *Hematology: Basic Principles and Practice*: Saunders/Elsevier; 2013. 2520-2521 p.
54. Dickerson RE, Geis I. *Hemoglobin: Structure, Function, Evolution, and Pathology*: Benjamin/Cummings Publishing Company; 1983.
55. Sadava DE, Hillis DM, Heller HC. *Life: The Science of Biology*: W. H. Freeman; 2011. 954 p.
56. Dimov AV, Liu T, Spincemaille P, Ecanow JS, Tan H, Edelman RR, Wang Y. Joint estimation of chemical shift and quantitative susceptibility mapping (chemical QSM). *Magn Reson Med* 2015;73(6):2100-2110.
57. Reeder SB, Pineda AR, Wen Z, Shimakawa A, Yu H, Brittain JH, Gold GE, Beaulieu CH, Pelc NJ. Iterative decomposition of water and fat with echo asymmetry and least-squares estimation (IDEAL): Application with fast spin-echo imaging. *Magnetic Resonance in Medicine* 2005;54(3):636-644.
58. Reeder SB, Wen Z, Yu H, Pineda AR, Gold GE, Markl M, Pelc NJ. Multicoil Dixon chemical species separation with an iterative least-squares estimation method. *Magnetic Resonance in Medicine* 2004;51(1):35-45.
59. Liu Z, Kee Y, Zhou D, Spincemaille P, Wang Y. Preconditioned QSM to Determine a Large Range of Susceptibility Over the Entire Field of View from Total Field. *Proc Int SocMagn Reson Med* 2016;24:0032.
60. Liu T, Khalidov I, de Rochefort L, Spincemaille P, Liu J, Tsiouris AJ, Wang Y. A novel background field removal method for MRI using projection onto dipole fields (PDF). *NMR in biomedicine* 2011;24(9):1129-1136.
61. Pei M, Nguyen TD, Thimmappa ND, Salustri C, Dong F, Cooper MA, Li J, Prince MR, Wang Y. An Algorithm for Fast Mono-exponential Fitting Based on Auto-Regression on Linear Operations (ARLO) of Data. *Magnetic resonance in medicine : official journal of the Society of Magnetic Resonance in Medicine / Society of Magnetic Resonance in Medicine* 2015;73(2):843-850.
62. Zhou D, Zhang J, Spincemaille P, Wang Y. Susceptibility Underestimation in a High Susceptibility Phantom: Dependence on Imaging Resolution, Magnitude Contrast and Sample Orientation. *Proc Int SocMagn Reson Med* 2016;24:1550.

63. Sasse SA, Berry RB, Nguyen TK, Light RW, Kees Mahutte C. Arterial Blood Gas Changes During Breath-holding From Functional Residual Capacity. *Chest* 1996;110(4):958-964.
64. Betgem RP, de Waard GA, Nijveldt R, Beek AM, Escaned J, van Royen N. Intramyocardial haemorrhage after acute myocardial infarction. *Nat Rev Cardiol* 2015;12(3):156-167.
65. Hamirani YS, Wong A, Kramer CM, Salerno M. Effect of Microvascular Obstruction and Intramyocardial Hemorrhage by CMR on LV Remodeling and Outcomes After Myocardial Infarction: A Systematic Review and Meta-Analysis. *JACC: Cardiovascular Imaging* 2014;7(9):940-952.
66. Goldfarb JW, Hasan U, Zhao W, Han J. Magnetic resonance susceptibility weighted phase imaging for the assessment of reperfusion intramyocardial hemorrhage. *Magn Reson Med* 2014;71(3):1210-1220.
67. Chen W, Zhu W, Kovanlikaya I, Kovanlikaya A, Liu T, Wang S, Salustri C, Wang Y. Intracranial calcifications and hemorrhages: characterization with quantitative susceptibility mapping. *Radiology* 2014;270(2):496-505.
68. Fassbender K, Balucani C, Walter S, Levine SR, Haass A, Grotta J. Streamlining of prehospital stroke management: the golden hour. *Lancet Neurol* 2013;12(6):585-596.
69. Chen W, Gauthier SA, Gupta A, Comunale J, Liu T, Wang S, Pei M, Pitt D, Wang Y. Quantitative Susceptibility Mapping of Multiple Sclerosis Lesions at Various Ages. *Radiology* 2014;271(1):183-192.
70. Funk E, Thunberg P, Anderzen-Carlsson A. Patients' experiences in magnetic resonance imaging (MRI) and their experiences of breath holding techniques. *Journal of Advanced Nursing* 2014;70(8):1880-1890.
71. Zhou D, Liu T, Spincemaille P, Wang Y. Background field removal by solving the Laplacian boundary value problem. *NMR in Biomedicine* 2014;27(3):312-319.
72. Sun H, Wilman AH. Quantitative susceptibility mapping using single-shot echo-planar imaging. *Magnetic Resonance in Medicine* 2015;73(5):1932-1938.
73. Deshmane A, Gulani V, Griswold MA, Seiberlich N. Parallel MR imaging. *Journal of Magnetic Resonance Imaging* 2012;36(1):55-72.
74. Quick HH, Ladd ME, Hoevel M, Bosk S, Debatin JF, Laub G, Schroeder T. Real-time MRI of joint movement with trueFISP. *Journal of Magnetic Resonance Imaging* 2002;15(6):710-715.

75. Uecker M, Lai P, Murphy MJ, Virtue P, Elad M, Pauly JM, Vasanawala SS, Lustig M. ESPIRiT—an eigenvalue approach to autocalibrating parallel MRI: Where SENSE meets GRAPPA. *Magnetic Resonance in Medicine* 2014;71(3):990-1001.
76. Kaaouana T, de Rochefort L, Samaille T, Thiery N, Dufouil C, Delmaire C, Dormont D, Chupin M. 2D harmonic filtering of MR phase images in multicenter clinical setting: Toward a magnetic signature of cerebral microbleeds. *NeuroImage* 2015;104:287-300.
77. Wei H, Zhang Y, Gibbs E, Chen N-K, Wang N, Liu C. Joint 2D and 3D phase processing for quantitative susceptibility mapping: application to 2D echo-planar imaging. *NMR in Biomedicine* 2016;doi:10.1002/nbm.3501.
78. Gallet R, Lellouche N, Mitchell-Heggs L, Bouhemad B, Bensaid A, Dubois-Randé J-L, Gueret P, Lim P. Prognosis value of central venous oxygen saturation in acute decompensated heart failure. *Archives of Cardiovascular Diseases* 2012;105(1):5-12.
79. Swiston JR, Johnson SR, Granton JT. Factors that prognosticate mortality in idiopathic pulmonary arterial hypertension: A systematic review of the literature. *Respiratory Medicine* 2010;104(11):1588-1607.
80. Sandoval J, Bauerle O, Palomar A, Gomez A, Martinez-Guerra ML, Beltran M, Guerrero ML. Survival in primary pulmonary hypertension. Validation of a prognostic equation. *Circulation* 1994;89(4):1733-1744.
81. Mullens W, Abrahams Z, Skouri HN, Taylor DO, Starling RC, Francis GS, Young JB, Tang WH. Prognostic evaluation of ambulatory patients with advanced heart failure. *Am J Cardiol* 2008;101(9):1297-1302.
82. Patel CB, DeVore AD, Felker GM, Wojdyla DM, Hernandez AF, Milano CA, O'Connor CM, Rogers JG. Characteristics and outcomes of patients with heart failure and discordant findings by right-sided heart catheterization and cardiopulmonary exercise testing. *Am J Cardiol* 2014;114(7):1059-1064.
83. Silvennoinen MJ, Kettunen MI, Kauppinen RA. Effects of hematocrit and oxygen saturation level on blood spin-lattice relaxation. *Magnetic Resonance in Medicine* 2003;49(3):568-571.
84. Lu H, Ge Y. Quantitative evaluation of oxygenation in venous vessels using T2-Relaxation-Under-Spin-Tagging MRI. *Magnetic Resonance in Medicine* 2008;60(2):357-363.
85. Varghese J, Potter LC, LaFountain R, Pan X, Raman SV, Ahmad R, Simonetti OP. CMR-based blood oximetry via multi-parametric estimation using

- multiple T2 measurements. *Journal of Cardiovascular Magnetic Resonance* 2017;19(1):88.
86. Ogawa S, Menon RS, Tank DW, Kim SG, Merkle H, Ellermann JM, Ugurbil K. Functional brain mapping by blood oxygenation level-dependent contrast magnetic resonance imaging. A comparison of signal characteristics with a biophysical model. *Biophysical journal* 1993;64(3):803-812.
  87. Bolar DS, Rosen BR, Sorensen AG, Adalsteinsson E. QUantitative Imaging of eXtraction of oxygen and Tissue consumption (QUIXOTIC) using venular-targeted velocity-selective spin labeling. *Magnetic Resonance in Medicine* 2011;66(6):1550-1562.
  88. Zhou D, Cho J, Zhang J, Spincemaille P, Wang Y. Susceptibility underestimation in a high-susceptibility phantom: Dependence on imaging resolution, magnitude contrast, and other parameters. *Magnetic Resonance in Medicine* 2017;78(3):1080-1086.
  89. Pauling L, Coryell CD. The Magnetic Properties and Structure of Hemoglobin, Oxyhemoglobin and Carbonmonoxyhemoglobin. *Proceedings of the National Academy of Sciences of the United States of America* 1936;22(4):210-216.
  90. Dimov AV, Liu Z, Spincemaille P, Prince MR, Du J, Wang Y. Bone quantitative susceptibility mapping using a chemical species-specific R2\* signal model with ultrashort and conventional echo data. *Magn Reson Med* 2018;79(1):121-128.
  91. Nguyen TD, Spincemaille P, Weinsaft JW, Ho BY, Cham MD, Prince MR, Wang Y. A fast navigator-gated 3D sequence for delayed enhancement MRI of the myocardium: Comparison with breathhold 2D imaging. *Journal of Magnetic Resonance Imaging* 2008;27(4):802-808.
  92. Nguyen TD, Spincemaille P, Cham MD, Weinsaft JW, Prince MR, Wang Y. Free-breathing 3-dimensional steady-state free precession coronary magnetic resonance angiography: comparison of four navigator gating techniques. *Magnetic Resonance Imaging* 2009;27(6):807-814.
  93. Liu Z, Spincemaille P, Yao Y, Zhang Y, Wang Y. MEDI+0: Morphology enabled dipole inversion with automatic uniform cerebrospinal fluid zero reference for quantitative susceptibility mapping. *Magn Reson Med* 2018;79(5):2795-2803.
  94. Liu T, Wisnieff C, Lou M, Chen W, Spincemaille P, Wang Y. Nonlinear formulation of the magnetic field to source relationship for robust quantitative susceptibility mapping. *Magnetic Resonance in Medicine* 2013;69(2):467-476.

95. Brunori M. Hemoglobin: Structure, function, evolution, and pathology. *Trends in Biochemical Sciences* 1984;9(5):176.
96. Billett H. Hemoglobin and Hematocrit. In: rd, Walker HK, Hall WD, Hurst JW, editors. *Clinical Methods: The History, Physical, and Laboratory Examinations*. Boston: Butterworth Publishers, a division of Reed Publishing.; 1990.
97. Ludbrook J. Linear regression analysis for comparing two measurers or methods of measurement: But which regression? *Clinical and Experimental Pharmacology and Physiology* 2010;37(7):692-699.
98. Golay X, Silvennoinen MJ, Zhou J, Clingman CS, Kauppinen RA, Pekar JJ, van Zij PCM. Measurement of tissue oxygen extraction ratios from venous blood T2: Increased precision and validation of principle. *Magnetic Resonance in Medicine* 2001;46(2):282-291.
99. Fernández-Seara MA, Techawiboonwong A, Detre JA, Wehrli FW. MR susceptibility for measuring global brain oxygen extraction. *Magnetic Resonance in Medicine* 2006;55(5):967-973.
100. Fan AP, Benner T, Bolar DS, Rosen BR, Adalsteinsson E. Phase-based regional oxygen metabolism (PROM) using MRI. *Magnetic Resonance in Medicine* 2012;67(3):669-678.
101. Haacke EM, Lai S, Reichenbach JR, Kuppusamy K, Hoogenraad FGC, Takeichi H, Lin W. In vivo measurement of blood oxygen saturation using magnetic resonance imaging: A direct validation of the blood oxygen level-dependent concept in functional brain imaging. *Human Brain Mapping* 1997;5(5):341-346.
102. Weisskoff RM, Kiihne S. MRI susceptibility: Image-based measurement of absolute susceptibility of MR contrast agents and human blood. *Magnetic Resonance in Medicine* 1992;24(2):375-383.
103. Haacke EM, Tang J, Neelavalli J, Cheng YCN. Susceptibility mapping as a means to visualize veins and quantify oxygen saturation. *Journal of Magnetic Resonance Imaging* 2010;32(3):663-676.
104. Cho J, Kee Y, Spincemaille P, Nguyen TD, Zhang J, Gupta A, Zhang S, Wang Y. Cerebral metabolic rate of oxygen (CMRO<sub>2</sub>) mapping by combining quantitative susceptibility mapping (QSM) and quantitative blood oxygenation level-dependent imaging (qBOLD). *Magnetic Resonance in Medicine* 2018;80(4):1595-1604.
105. Zhang J, Cho J, Zhou D, Nguyen TD, Spincemaille P, Gupta A, Wang Y. Quantitative susceptibility mapping-based cerebral metabolic rate of oxygen

- mapping with minimum local variance. *Magnetic Resonance in Medicine* 2018;79(1):172-179.
106. Barratt-Boyes BG, Wood EH. The oxygen saturation of blood in the venae cavae, right-heart chambers, and pulmonary vessels of healthy subjects. *The Journal of Laboratory and Clinical Medicine* 1957;50(1):93-106.
  107. Lustig M, Donoho D, Pauly JM. Sparse MRI: The application of compressed sensing for rapid MR imaging. *Magnetic Resonance in Medicine* 2007;58(6):1182-1195.
  108. Larson AC, White RD, Laub G, McVeigh ER, Li D, Simonetti OP. Self-gated cardiac cine MRI. *Magnetic resonance in medicine* 2004;51(1):93-102.
  109. Xu B, Spincemaille P, Chen G, Agrawal M, Nguyen TD, Prince MR, Wang Y. Fast 3D contrast enhanced MRI of the liver using temporal resolution acceleration with constrained evolution reconstruction. *Magnetic Resonance in Medicine* 2013;69(2):370-381.
  110. Dewey M, Teige F, Schnapauff D, et al. Noninvasive detection of coronary artery stenoses with multislice computed tomography or magnetic resonance imaging. *Annals of Internal Medicine* 2006;145(6):407-415.
  111. Nguyen TD, Spincemaille P, Prince MR, Wang Y. Cardiac fat navigator-gated steady-state free precession 3D magnetic resonance angiography of coronary arteries. *Magnetic Resonance in Medicine* 2006;56(1):210-215.
  112. Nguyen TD, Nuval A, Mulukutla S, Wang Y. Direct monitoring of coronary artery motion with cardiac fat navigator echoes. *Magnetic Resonance in Medicine* 2003;50(2):235-241.
  113. Nguyen TD, Spincemaille P, Cham MD, Weinsaft JW, Prince MR, Wang Y. Free-Breathing 3D Steady-State Free Precession Coronary Magnetic Resonance Angiography: Comparison of Diaphragm and Cardiac Fat Navigators. *Journal of magnetic resonance imaging : JMRI* 2008;28(2):509-514.
  114. Wagner A, Mahrholdt H, Thomson L, Hager S, Meinhardt G, Rehwald W, Parker M, Shah D, Sechtem U, Kim RJ, Judd RM. Effects of Time, Dose, and Inversion Time for Acute Myocardial Infarct Size Measurements Based on Magnetic Resonance Imaging-Delayed Contrast Enhancement. *Journal of the American College of Cardiology* 2006;47(10):2027-2033.
  115. Aime S, Caravan P. Biodistribution of gadolinium-based contrast agents, including gadolinium deposition. *Journal of Magnetic Resonance Imaging* 2009;30(6):1259-1267.

116. Schneider AT, Kissela B, Woo D, Kleindorfer D, Alwell K, Miller R, Szaflarski J, Gebel J, Khoury J, Shukla R, Moomaw C, Pancioli A, Jauch E, Broderick J. Ischemic stroke subtypes - A population-based study of incidence rates among blacks and whites. *Stroke* 2004;35(7):1552-1556.
117. Flaherty ML, Kissela B, Khoury JC, Alwell K, Moomaw CJ, Woo D, Khatri P, Ferioli S, Adeoye O, Broderick JP, Kleindorfer D. Carotid artery stenosis as a cause of stroke. *Neuroepidemiology* 2013;40(1):36-41.
118. Cai JM, Hatsukami TS, Ferguson MS, Small R, Polissar NL, Yuan C. Classification of human carotid atherosclerotic lesions with in vivo multicontrast magnetic resonance imaging. *Circulation* 2002;106(11):1368-1373.
119. Saam T, Hetterich H, Hoffmann V, Yuan C, Treitl M, Dichgans M, Poppert H, Reiser M, Bamberg F. Meta-Analysis and Systematic Review of the Predictive Value of Carotid Plaque Hemorrhage by Magnetic Resonance Imaging on Cerebrovascular Events. *Circulation* 2012;126(21).
120. Gupta A, Baradaran H, Schweitzer AD, Kamel H, Pandya A, Delgado D, Dunning A, Mushlin AI, Sanelli PC. Carotid plaque MRI and stroke risk: a systematic review and meta-analysis. *Stroke* 2013;44(11):3071-3077.
121. Gupta A, Mushlin AI, Kamel H, Navi BB, Pandya A. Cost-Effectiveness of Carotid Plaque MR Imaging as a Stroke Risk Stratification Tool in Asymptomatic Carotid Artery Stenosis. *Radiology* 2015;277(3):763-772.
122. Singh N, Moody AR, Gladstone DJ, Leung G, Ravikumar R, Zhan J, Maggisano R. Moderate carotid artery stenosis: MR imaging-depicted intraplaque hemorrhage predicts risk of cerebrovascular ischemic events in asymptomatic men. *Radiology* 2009;252(2):502-508.
123. Altaf N, MacSweeney ST, Gladman J, Auer DP. Carotid intraplaque hemorrhage predicts recurrent symptoms in patients with high-grade carotid stenosis. *Stroke* 2007;38(5):1633-1635.
124. Barger AC, Beeuwkes R, 3rd, Lainey LL, Silverman KJ. Hypothesis: vasa vasorum and neovascularization of human coronary arteries. A possible role in the pathophysiology of atherosclerosis. *N Engl J Med* 1984;310(3):175-177.
125. Daemen MJ, Ferguson MS, Gijzen FJ, Hippe DS, Kooi ME, Demarco K, van der Wal AC, Yuan C, Hatsukami TS. Carotid plaque fissure: An underestimated source of intraplaque hemorrhage. *Atherosclerosis* 2016;254:102-108.

126. Lusby RJ, Ferrell LD, Ehrenfeld WK, Stoney RJ, Wylie EJ. Carotid Plaque Hemorrhage - Its Role in Production of Cerebral-Ischemia. *Arch Surg-Chicago* 1982;117(11):1479-1488.
127. Yuan C, Mitsumori LM, Ferguson MS, Polissar NL, Echelard D, Ortiz G, Small R, Davies JW, Kerwin WS, Hatsukami TS. In vivo accuracy of multispectral magnetic resonance imaging for identifying lipid-rich necrotic cores and intraplaque hemorrhage in advanced human carotid plaques. *Circulation* 2001;104(17):2051-2056.
128. Saam T, Ferguson MS, Yarnykh VL, Takaya N, Xu D, Polissar NL, Hatsukami TS, Yuan C. Quantitative evaluation of carotid plaque composition by in vivo MRI. *Arterioscler Thromb Vasc Biol* 2005;25(1):234-239.
129. Fan Z, Yu W, Xie Y, Dong L, Yang L, Wang Z, Conte AH, Bi X, An J, Zhang T, Laub G, Shah PK, Zhang Z, Li D. Multi-contrast atherosclerosis characterization (MATCH) of carotid plaque with a single 5-min scan: technical development and clinical feasibility. *Journal of cardiovascular magnetic resonance : official journal of the Society for Cardiovascular Magnetic Resonance* 2014;16:53.
130. Wang J, Bornert P, Zhao H, Hippe DS, Zhao X, Balu N, Ferguson MS, Hatsukami TS, Xu J, Yuan C, Kerwin WS. Simultaneous noncontrast angiography and intraplaque hemorrhage (SNAP) imaging for carotid atherosclerotic disease evaluation. *Magnetic resonance in medicine* 2013;69(2):337-345.
131. Chu B, Kampschulte A, Ferguson MS, Kerwin WS, Yarnykh VL, O'Brien KD, Polissar NL, Hatsukami TS, Yuan C. Hemorrhage in the atherosclerotic carotid plaque: a high-resolution MRI study. *Stroke* 2004;35(5):1079-1084.
132. Ota H, Yarnykh VL, Ferguson MS, Underhill HR, Demarco JK, Zhu DC, Oikawa M, Dong L, Zhao X, Collar A, Hatsukami TS, Yuan C. Carotid intraplaque hemorrhage imaging at 3.0-T MR imaging: comparison of the diagnostic performance of three T1-weighted sequences. *Radiology* 2010;254(2):551-563.
133. Baradaran H, Al-Dasuqi K, Knight-Greenfield A, Giambone A, Delgado D, Ebani EJ, Kamel H, Gupta A. Association between Carotid Plaque Features on CTA and Cerebrovascular Ischemia: A Systematic Review and Meta-Analysis. *AJNR Am J Neuroradiol* 2017;38(12):2321-2326.
134. de Rochefort L, Liu T, Kressler B, Liu J, Spincemaille P, Lebon V, Wu J, Wang Y. Quantitative susceptibility map reconstruction from MR phase data using bayesian regularization: validation and application to brain imaging. *Magnetic resonance in medicine* 2010;63(1):194-206.

135. Wang Y, Liu T. Quantitative susceptibility mapping (QSM): Decoding MRI data for a tissue magnetic biomarker. *Magnetic resonance in medicine* 2015;73(1):82-101.
136. Haacke EM, Liu SF, Buch S, Zheng WL, Wu DM, Ye YQ. Quantitative susceptibility mapping: current status and future directions. *Magn Reson Imaging* 2015;33(1):1-25.
137. Deistung A, Schweser F, Reichenbach JR. Overview of quantitative susceptibility mapping. *Nmr in Biomedicine* 2017;30(4).
138. Wang Y, Spincemaille P, Liu Z, Dimov A, Deh K, Li J, Zhang Y, Yao Y, Gillen KM, Wilman AH, Gupta A, Tsiouris AJ, Kovanlikaya I, Chiang GC, Weinsaft JW, Tanenbaum L, Chen W, Zhu W, Chang S, Lou M, Kopell BH, Kaplitt MG, Devos D, Hirai T, Huang X, Korogi Y, Shtilbans A, Jahng GH, Pelletier D, Gauthier SA, Pitt D, Bush AI, Brittenham GM, Prince MR. Clinical quantitative susceptibility mapping (QSM): Biometal imaging and its emerging roles in patient care. *Journal of magnetic resonance imaging : JMRI* 2017;46(4):951-971.
139. Chang S, Zhang J, Liu T, Tsiouris AJ, Shou J, Nguyen T, Leifer D, Wang Y, Kovanlikaya I. Quantitative Susceptibility Mapping of Intracerebral Hemorrhages at Various Stages. *Journal of magnetic resonance imaging : JMRI* 2016;44(2):420-425.
140. Liu T, Spincemaille P, de Rochefort L, Wong R, Prince M, Wang Y. Unambiguous identification of superparamagnetic iron oxide particles through quantitative susceptibility mapping of the nonlinear response to magnetic fields. *Magn Reson Imaging* 2010;28(9):1383-1389.
141. Schweser F, Deistung A, Lehr BW, Reichenbach JR. Differentiation between diamagnetic and paramagnetic cerebral lesions based on magnetic susceptibility mapping. *Med Phys* 2010;37(10):5165-5178.
142. Wang C, Liu S, Chen Y, Buch S, Fan Z, Haacke EM, Yang Q. Intraplaque hemorrhage and calcification detection with quantitative susceptibility mapping. *ISMRM*. 2018.
143. Ruetten P, Priest AN, Yuan J, Usman A, Gillard JH, Graves MJ. Phase corrected bipolar acquisition for simultaneous water-fat separation and quantitative susceptibility mapping of the carotid artery wall. *ISMRM*. 2018.
144. Ikebe Y, Ishimaru H, Imai H, Abe K, Izumo T, Morofuji Y, Ideguchi R, Morikawa M, Uetani M. Quantitative Susceptibility Mapping for Carotid Atherosclerotic Plaques: A Pilot Study. *Magn Reson Med Sci* 2019.

145. Li W, Wu B, Liu C. Quantitative susceptibility mapping of human brain reflects spatial variation in tissue composition. *Neuroimage* 2011;55(4):1645-1656.
146. Schweser F, Robinson SD, de Rochefort L, Li W, Bredies K. An illustrated comparison of processing methods for phase MRI and QSM: removal of background field contributions from sources outside the region of interest. *NMR Biomed* 2017;30(4).
147. Liu T, Wisnieff C, Lou M, Chen W, Spincemaille P, Wang Y. Nonlinear formulation of the magnetic field to source relationship for robust quantitative susceptibility mapping. *Magnetic resonance in medicine* 2013;69(2):467-476.
148. Liu Z, Kee Y, Zhou D, Wang Y, Spincemaille P. Preconditioned total field inversion (TFI) method for quantitative susceptibility mapping. *Magn Reson Med* 2017;78(1):303-315.
149. Wen Y, Zhou D, Liu T, Spincemaille P, Wang Y. An iterative spherical mean value method for background field removal in MRI. *Magnetic resonance in medicine* 2014;72(4):1065-1071.
150. Li W, Avram AV, Wu B, Xiao X, Liu C. Integrated Laplacian-based phase unwrapping and background phase removal for quantitative susceptibility mapping. *NMR Biomed* 2014;27(2):219-227.
151. Ozbay PS, Deistung A, Feng X, Nanz D, Reichenbach JR, Schweser F. A comprehensive numerical analysis of background phase correction with V-SHARP. *NMR Biomed* 2017;30(4).
152. Saba L, Yuan C, Hatsukami TS, Balu N, Qiao Y, DeMarco JK, Saam T, Moody AR, Li D, Matouk CC, Johnson MH, Jager HR, Mossa-Basha M, Kooi ME, Fan Z, Saloner D, Wintermark M, Mikulis DJ, Wasserman BA, Vessel Wall Imaging Study Group of the American Society of N. Carotid Artery Wall Imaging: Perspective and Guidelines from the ASNR Vessel Wall Imaging Study Group and Expert Consensus Recommendations of the American Society of Neuroradiology. *AJNR Am J Neuroradiol* 2018;39(2):E9-E31.
153. Pineda AR, Reeder SB, Wen Z, Pelc NJ. Cramer-Rao bounds for three-point decomposition of water and fat. *Magnetic resonance in medicine* 2005;54(3):625-635.
154. Fortier V, Levesque IR. Phase processing for quantitative susceptibility mapping of regions with large susceptibility and lack of signal. *Magnetic resonance in medicine* 2018;79(6):3103-3113.
155. Bradley WG, Jr. MR appearance of hemorrhage in the brain. *Radiology* 1993;189(1):15-26.

156. Underhill HR, Yarnykh VL, Hatsukami TS, Wang J, Balu N, Hayes CE, Oikawa M, Yu W, Xu D, Chu B, Wyman BT, Polissar NL, Yuan C. Carotid plaque morphology and composition: initial comparison between 1.5- and 3.0-T magnetic field strengths. *Radiology* 2008;248(2):550-560.
157. Millon A, Mathevet JL, Boussel L, Faries PL, Fayad ZA, Douek PC, Feugier P. High-resolution magnetic resonance imaging of carotid atherosclerosis identifies vulnerable carotid plaques. *J Vasc Surg* 2013;57(4):1046-1051 e1042.
158. den Hartog AG, Bovens SM, Koning W, Hendrikse J, Luijten PR, Moll FL, Pasterkamp G, de Borst GJ. Current Status of Clinical Magnetic Resonance Imaging for Plaque Characterisation in Patients with Carotid Artery Stenosis. *Eur J Vasc Endovasc* 2013;45(1):7-21.
159. Boussel L, Arora S, Rapp J, Rutt B, Huston J, Parker D, Yuan C, Bassiouny H, Saloner D, Investigators M. Atherosclerotic plaque progression in carotid arteries: monitoring with high-spatial-resolution MR imaging--multicenter trial. *Radiology* 2009;252(3):789-796.
160. Wang Y, Grist TM, Korosec FR, Christy PS, Alley MT, Polzin JA, Mistretta CA. Respiratory blur in 3D coronary MR imaging. *Magn Reson Med* 1995;33(4):541-548.
161. Boussel L, Herigault G, de la Vega A, Nonent M, Douek PC, Serfaty JM. Swallowing, arterial pulsation, and breathing induce motion artifacts in carotid artery MRI. *Journal of magnetic resonance imaging : JMRI* 2006;23(3):413-415.
162. Dyverfeldt P, Deshpande VS, Kober T, Krueger G, Saloner D. Reduction of motion artifacts in carotid MRI using free-induction decay navigators. *Journal of magnetic resonance imaging : JMRI* 2014;40(1):214-220.
163. Wang Y, Rossman PJ, Grimm RC, Wilman AH, Riederer SJ, Ehman RL. 3D MR angiography of pulmonary arteries using real-time navigator gating and magnetization preparation. *Magn Reson Med* 1996;36(4):579-587.
164. De A, Sun H, Emery DJ, Butcher KS, Wilman AH. Rapid quantitative susceptibility mapping of intracerebral hemorrhage. *Journal of magnetic resonance imaging : JMRI* 2019.
165. Wei H, Dibb R, Zhou Y, Sun Y, Xu J, Wang N, Liu C. Streaking artifact reduction for quantitative susceptibility mapping of sources with large dynamic range. *NMR Biomed* 2015;28(10):1294-1303.

166. Wang S, Liu T, Chen W, Spincemaille P, Wisnieff C, Tsiouris AJ, Zhu W, Pan C, Zhao L, Wang Y. Noise Effects in Various Quantitative Susceptibility Mapping Methods. *IEEE Trans Biomed Eng* 2013;60(12):3441-3448.
167. Kressler B, de Rochefort L, Liu T, Spincemaille P, Jiang Q, Wang Y. Nonlinear regularization for per voxel estimation of magnetic susceptibility distributions from MRI field maps. *IEEE Trans Med Imaging* 2010;29(2):273-281.
168. Liu Z, Wen Y, Spincemaille P, Zhang S, Yao Y, Nguyen TD, Wang Y. Automated adaptive preconditioner for quantitative susceptibility mapping. *Magnetic Resonance in Medicine* 2020;83(1):271-285.
169. Hansen PC, Jensen TK, Rodriguez G. An adaptive pruning algorithm for the discrete L-curve criterion. *Journal of Computational and Applied Mathematics* 2007;198(2):483-492.
170. Pei M, Nguyen TD, Thimmappa ND, Salustri C, Dong F, Cooper MA, Li J, Prince MR, Wang Y. Algorithm for fast monoexponential fitting based on Auto-Regression on Linear Operations (ARLO) of data. *Magnetic resonance in medicine* 2015;73(2):843-850.
171. Zubal IG, Harrell CR, Smith EO, Rattner Z, Gindi G, Hoffer PB. Computerized three-dimensional segmented human anatomy. *Med Phys* 1994;21(2):299-302.
172. Marques J, Bilgic B, Meineke J, Milovic C, Chan K-S, Van der Zwaag W, Hedouin R, Langkammer C, Schweser F. Towards QSM Challenge 2.0: Creation and Evaluation of a Realistic Magnetic Susceptibility Phantom2019.
173. Robinson SD, Bredies K, Khabipova D, Dymerska B, Marques JP, Schweser F. An illustrated comparison of processing methods for MR phase imaging and QSM: combining array coil signals and phase unwrapping. *NMR Biomed* 2017;30(4).
174. Milovic C, Bilgic B, Zhao B, Acosta-Cabronero J, Tejos C. Fast nonlinear susceptibility inversion with variational regularization. *Magnetic Resonance in Medicine* 2018;80(2):814-821.
175. Hyun CM, Kim HP, Lee SM, Lee S, Seo JK. Deep learning for undersampled MRI reconstruction. *Physics in Medicine & Biology* 2018;63(13):135007.
176. Küstner T, Armanious K, Yang J, Yang B, Schick F, Gatidis S. Retrospective correction of motion-affected MR images using deep learning frameworks. *Magnetic Resonance in Medicine* 2019;82(4):1527-1540.